Measurement of light neutral mesons and photons in p–Pb collisions at $\sqrt{s_{\rm NN}}=5.02\,{\rm TeV}$ with ALICE at the LHC

Master's Thesis

Fachbereich Physik Goethe Universität Frankfurt am Main Institut für Kernphysik

submitted by
Stefanie Mrozinski

November 2024

Gutachter: Prof. Dr. Henner Büsching

Prof. Dr. Harald Appelshäuser

Contents

1	Inti	roducti	ion	1
2	The	eoretica	al Background	3
	2.1	The B	Building Blocks of Matter and Their Interaction	3
	2.2	The S	trong Interaction	3
	2.3	The Q	QGP	6
	2.4	Invest	igating the QGP	7
		2.4.1	Neutral Mesons	7
		2.4.2	Nuclear Modification Factor (R_{AA})	8
		2.4.3	Probing the QGP Using Photons	11
	2.5	Direct	-Photon Measurement	12
		2.5.1	Related Work	13
3	Exp	erime	nt	15
	3.1	Partic	ele Acceleration at the Large Hadron Collider (LHC)	15
	3.2	The A	LICE Experiment	17
		3.2.1	V0 Detector	18
		3.2.2	Inner Tracking System (ITS)	18
		3.2.3	Time Projection Chamber (TPC)	19
		3.2.4	Photon Spectrometer (PHOS)	19
	3.3	ALICI	E Software Framework	21
4	Dat	a Pres	selection	22
	4.1	Data S	Sets and Event Selection	22
	4.2	Photo	n Reconstruction Methods	24
		4.2.1	Photon Conversions	24
		4.2.2	Calorimetry	28
5	Neı	ıtral-N	Ieson Measurement	34
	5.1	Signal	Extraction	34
	5.2	Correc	ctions	39
		5.2.1	Secondary Contamination	40
		5.2.2	Acceptance and Efficiency	41
	5.3	System	matic Uncertainties	43

Contents

	5.4	Result	s	47
		5.4.1	Minimum Bias	47
		5.4.2	Centrality Dependence	56
6	Dire	ect-Ph	oton Measurement	64
	6.1	Inclusi	ive Photon Yield	64
		6.1.1	Corrections	64
		6.1.2	Corrected Inclusive Photon Yield	70
	6.2	Decay	Photons	71
		6.2.1	Particle Cocktail Input	71
		6.2.2	Particle Cocktail Simulation and Output	73
	6.3	Result	SS	75
7	Sun	nmary		77
8	App	endix		7 9
	8.1	Run L	$_{ m dist}$	79
	8.2	p_{T} Inte	ervals	79
	8.3	Contri	abutions to the Decay Cocktail	79

1 Introduction

In 2022, the particle physics community celebrated the 50th anniversary of Quantum Chromodynamics (QCD), the theory of the strong interaction, first proposed by Harald Fritzsch in 1972–73 [1]. QCD explains how the fundamental building blocks of matter interact via the strong force. While theoretical advancements have significantly deepened our understanding of the strong interaction, emergent QCD phenomena remain challenging to calculate directly from the fundamental principles of QCD. One key emergent QCD phenomenon that remains an object of interest today is the Quark-Gluon Plasma (QGP), a hot and dense medium, thought to have existed shortly after the Big Bang.

Studying the QGP in experiments requires extremely high temperatures or a large baryon-chemical potential. The former are achieved in heavy-ion collisions at the Large Hadron Collider (LHC) at CERN. The ALICE experiment, one of the four major experiments at the LHC, is specifically designed to investigate the QGP and its properties. However, the short lifetime of the QGP makes direct observation difficult, requiring the use of signatures that are influenced by the hot and dense medium.

In recent years, extensive experimental efforts have focused on measuring such signatures of the QGP. Measurements of neutral mesons like π^0 and η , for instance, enable studies of parton energy loss within the medium. Another key probe are direct photons, which potentially give access to an effective temperature of the system. These observables not only characterize the QGP but also, when measured across different collision systems, provide essential insights into the medium's formation conditions.

This work focuses on the π^0 , η and direct-photon measurement in p–Pb collisions. In this collision system no medium formation is expected. However, the measurements in p–Pb serve as a crucial reference for the Pb–Pb collision system, where a QGP formation is expected. Additionally, so-called cold nuclear matter (CNM) effects that arise in p–Pb but not in pp collisions can be studied.

To measure these observables, ALICE employs a variety of detectors. This analysis aims to combine two particle reconstruction techniques: the Photon Spectrometer (PHOS) and the Photon Conversion Method (PCM). This work is the first attempt to use this so-called PCM-PHOS method in p-Pb collisions. Combining the two detection methods enables precise low-momentum neutral meson measurements and reduces the need for certain corrections. In LHC Run 1, limited statistics restricted the use of this reconstruction method. However, the substantial increase in statistics in LHC

Run 2 opens new possibilities for applying this technique.

This analysis presents the first measurements of the π^0 and η mesons using the PCM-PHOS technique at a center-of-mass energy of $\sqrt{s_{\rm NN}}=5.02$ TeV in p–Pb collisions. These measurements allow for a feasibility study of the direct-photon measurement with the PCM-PHOS approach.

The second chapter of this thesis provides a theoretical overview of the strong interaction, the QGP, and the experimental means to probe it. In the third chapter the experimental setup, focusing on the detectors used in the measurement, is introduced. The fourth chapter presents the datasets used for this analysis, covering data and event selection criteria, photon reconstruction, and photon selection criteria for both the PCM method and the PHOS detector. In the next chapter the analysis of neutral mesons, with corrections and systematic uncertainties are discussed and the results of the measurements are presented. In the sixth chapter, the direct-photon measurement is discussed. Finally, the results are summarized and contextualized in the concluding chapter.

2 Theoretical Background

This chapter introduces the Standard Model of particle physics and its constituents, which are central to the measurements presented in this thesis. It focuses on the strong interaction and discusses its role in the Quark-Gluon Plasma (QGP). Potential probes and signatures of the QGP, especially through direct-photon measurements, are also introduced. Lastly, an overview of previous direct-photon measurements is provided to contextualize this research and highlight the significance of its findings.

2.1 The Building Blocks of Matter and Their Interaction

In particle physics, the Standard Model is a framework that classifies indivisible constituents of matter. The most fundamental distinction among particles is based on their spin, dividing them into bosons and fermions. Elementary bosons, including gauge and scalar bosons, have integer spins, while elementary fermions have half-integer spins. Fermions are further categorized into six quarks and six leptons, which are grouped into three generations. These subdivisions for fermions are summarized in Table 2.1 [2].

The quarks and leptons are also differentiated through the charges they carry. These charges are necessary conditions for particles to participate in certain kinds of interactions. In the Standard Model, four distinct bosons, listed in Table 2.2, mediate particle interactions by exchanging various charges. The electromagnetic interaction is mediated by photons, the weak interaction is mediated by the W and Z bosons, and the strong interaction is mediated by gluons. As gluons carry color charge, they can interact with themselves, a peculiarity of the strong interaction. The next section discusses the main focus of the analysis presented in this thesis – the strong interaction.

2.2 The Strong Interaction

The strong interaction is described by Quantum Chromodynamics (QCD), a field theory proposed by Fritzsch et al. in 1972 [1] to characterize the interactions between quarks and gluons. In an approximate form, the potential between two color-charged particles can be expressed by the following equation:

$$V_{\rm QCD}(r) = -\frac{4}{3}\frac{\alpha_{\rm s}}{r} + kr. \tag{2.1}$$

Generation	I	II	III	Electric charge
Quarks	up (u)	charm (c)	top (t)	$+\frac{2}{3}$
Quarks	down(d)	strange (s)	bottom (b)	$-\frac{1}{3}$
Lontons	electron (e)	$myon (\mu)$	$tau(\tau)$	-1
Leptons	e-neutrino (ν_e)	μ -neutrino (ν_{μ})	τ -neutrino (ν_{τ})	0

Table 2.1: Summary of quarks and gluons and sorted according to their electric charge and generation [3].

Interaction	Electromagnetic	Weak	Strong
boson	photon (γ)	W^{\pm}, Z	gluon (g)

Table 2.2: Summary of the interactions between particles and the corresponding bosons [2].

Here r represents the radial distance of the elementary particles, $\alpha_{\rm s}$ the coupling constant of the strong interaction and k the so-called string tension. The first term defines the repulsive part of the interaction, and the second term the attractive component. For small distances $r < 1\,{\rm fm}$ the repulsive part of the interaction dominates. At longer distances the linearly increasing second term starts to dominate the potential. As the energy density rises, rather than isolating the quarks, the potential energy facilitates the creation of new quark-antiquark pairs or triplets. This phenomenon, where only bound colorless quark pairs or triplets are observed in nature – forming particles such as baryons and mesons – is known as confinement.

The strength of an interaction is defined by its coupling constant. For example, the coupling constant in QED is approximately $\alpha_{\rm QED} \approx \frac{1}{137}$. Although in Equation 2.1 $\alpha_{\rm s}$ is treated as a constant, $\alpha_{\rm s}$ depends on the transferred momentum Q. A similar dependence exists for α_{QED} in QED, but it is so weak that it is often neglected. The dependence of $\alpha_{\rm s}$ on Q can be described through perturbative calculations by the following equation:

$$\alpha_{\rm s}(Q^2) = \frac{\alpha_{\rm s}(Q_0^2)}{1 + B_{\alpha_{\rm s}}(Q_0^2) \ln(Q^2/Q_0^2)},$$
(2.2)

where B_{α_s} is a constant and $\alpha_s(Q_0^2)$ is the coupling constant at a reference scale Q_0 . QCD perturbation theory is only valid for $\alpha_s \ll 1$, so Equation 2.2 is only applicable for $Q^2 \gg Q_0^2$. For large momentum transfers, corresponding to small distances between quarks, the force from the strong interaction weakens as can be seen in Figure 2.1, where α_s is shown as a function of the momentum transfer Q. For small distances, not only does the attractive component approach zero, but so does the repulsive one,

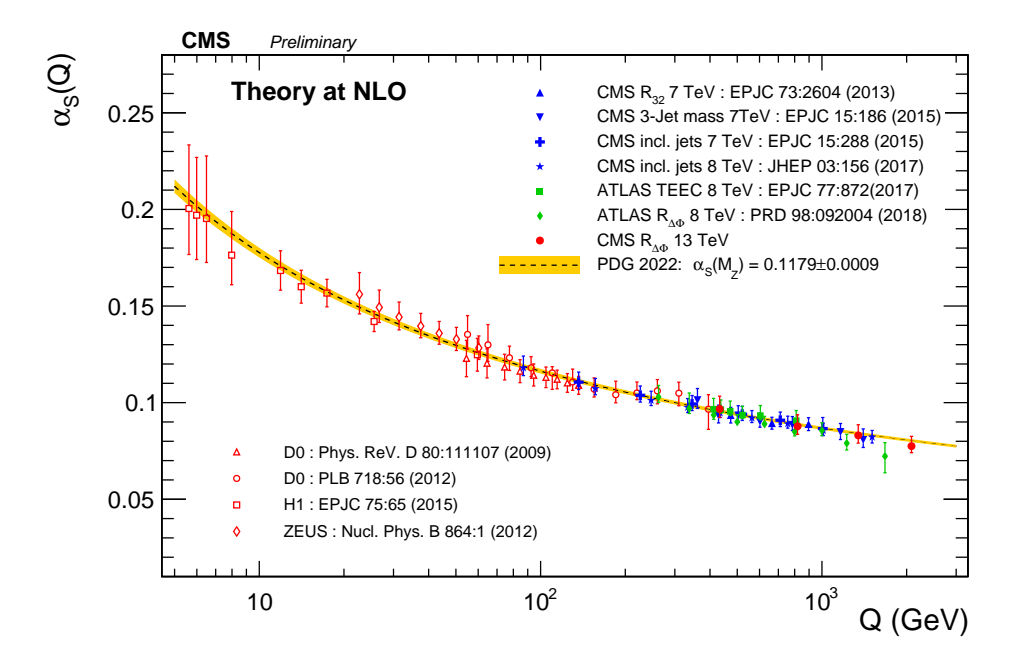


Figure 2.1: Running of the strong coupling constant α_s (Q) (dashed line) together with its associated total uncertainty (yellow band) [4].

making the quarks nearly free. This behavior is known as asymptotic freedom.

To calculate the cross-section σ of a given QCD process, all contributing Feynman diagrams for that process need to be considered. This involves calculating the matrix element M, which essentially results from summing the contributions of these diagrams and accounting for interference effects. For example, the cross-section σ of a single Feynman diagram with two fundamental QCD vertices is given by:

$$\sigma \propto |M|^2 \propto \left(\sqrt{\alpha_{\rm s}^2}\right)^2$$
. (2.3)

Each vertex contributes to M with the square root of the coupling constant α_s . Processes with more than two vertices are called higher-order processes. An infinite number of Feynman diagrams exist for any QCD process, meaning theoretically that all of them contribute to the calculation of σ . As a result, the calculation of σ depends crucially on the magnitude of α_s . For hard processes, where α_s is small, higher-order processes can be neglected, allowing for perturbative QCD (pQCD) calculations similar to those used in QED. For soft processes α_s reaches unity which makes higher-order processes significant for determining σ . Therefore, experimental inputs are crucial for developing, testing, and improving theoretical models to better explain fundamental QCD phenomena, such as the QGP.

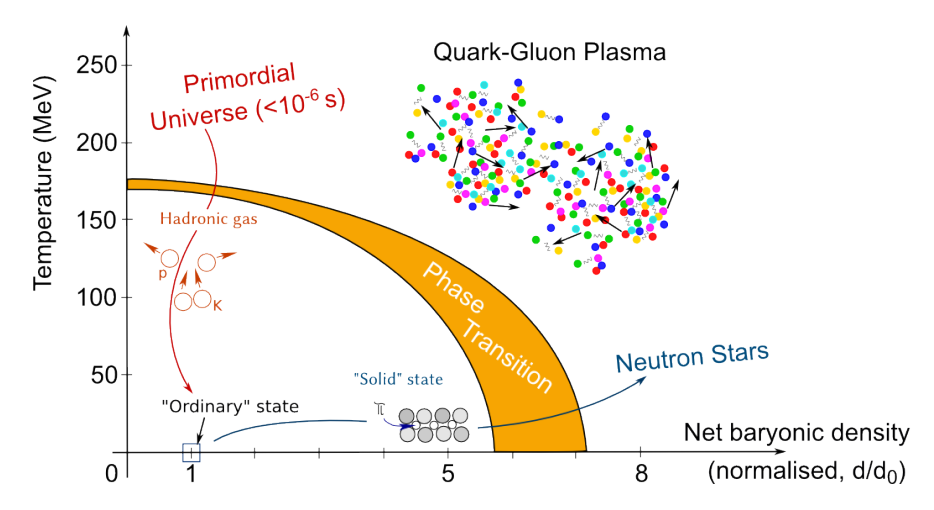


Figure 2.2: Phase diagram (temperature, net baryon density) of QCD matter, ranging from regular nuclear matter to the QGP [4].

2.3 The QGP

As described in the previous section, at high energy densities, hadronic matter dissolves into quarks and gluons that roam in a quasi-free state. This new state of nuclear matter of deconfined quarks is generally known as the QGP. The QGP is one of the states of matter that is depicted in the phase diagram in Figure 2.2, where the state variables are the temperature and the net baryon density (ρ_b). As depicted, the conditions for forming a QGP are high temperatures and high baryon density [1].

A key research topic is to further characterize the transition to the QGP, specifically determining whether it is a cross-over or first-order phase transition, and identifying the temperature at which it occurs. Early theoretical predictions placed the critical temperature, $T_{\rm Crit}$, for this transition between 100 MeV and 250 MeV. However, more recent calculations have refined this estimate to $T_{\rm Crit} \approx 150-160$ MeV, at low baryon chemical potential. The temperature and the baryon density restrict the occurrence of the QGP to two primary possibilities. Cosmologists suggest that the QGP existed during the early universe, immediately after the Big Bang, before the universe cooled from a hot QCD state to ordinary matter. Additionally, QGP may be present despite relatively low temperatures in neutron stars, where high baryon density causes the wave functions of neutrons to overlap. Given the extreme conditions under which a QGP can form, replicating them in experimental settings presents significant challenges [1]. It is believed that smaller collision systems, such as proton-proton or lepton-lepton, do not meet the conditions necessary for QGP formation, as they lack the particle density required to achieve an equilibrium state. In contrast, larger collision systems, like

heavy-ion collisions, are expected to form an equilibrium state if they reach a certain minimum energy, where the QGP can form. Since the 1970s, various experimental efforts have aimed to investigate the QGP in facilities, such as the Berkeley Bevelac and the JINR Synchrophasotron. More powerful accelerators developed throughout the 1980's and 1990's paved the way for further studies of the hot and dense medium. With energies 27 times higher than those in the Relativistic Heavy Ion Collider (RHIC), the LHC enables deeper investigations into various states of the QGP. By facilitating both heavy-ion collisions and smaller systems like pp, p–Pb, and nuclei, the LHC allows for the study of the dependence of the QGP formation on the system size.

2.4 Investigating the QGP

While the LHC provides the conditions necessary for the potential formation of a QGP, its investigation faces a significant challenge. The analysis of the QGP in equilibrium is constrained by its extremely short lifetime, approximately 10×10^{-23} s [3, 1]. As a result, research relies on indirect methods, or signatures, to infer properties of the medium and its formation conditions. Over the past decades, numerous signatures have been associated with QGP production. This brief overview focuses on the measurement of particle production, in particular that of neutral mesons, the nuclear modification factor and photon signatures, while referring the reader to existing literature for discussions of other signatures, such as global event properties [5, 1].

2.4.1 Neutral Mesons

The measurement of various particles produced in high-energy particle collisions forms the fundamental basis of experimental high-energy physics. Neutral mesons $(\pi^0, \eta, \omega, \rho, \text{ etc.})$ span a wide mass range, making them highly sensitive probes for many effects. This analysis aims to measure the π^0 , and η meson as well as the direct photons. The π^0 meson has a mass of $m_{\pi^0}=134.97\,\text{MeV/c}^2$, making it the lightest neutral meson. It consists of u and anti-u or d and anti-d quarks, expressed as $\pi^0=\frac{1}{\sqrt{2}}(u\bar{u}-d\bar{d})$. Its mean lifetime corresponds to $\tau=(8.4\pm0.3)\times10^{-17}\text{s}$. The dominant decay channel into two photons has a branching ratio of about $98.82\,\%$, while the Dalitz decay into a photon, electron, and positron occurs with a branching ratio of about $1.174\,\%$. The η meson, with a mass of $m_{\eta}=547.86\,\text{MeV/c}^2$, is the second-lightest neutral meson. It is composed of u and anti-u, d and anti-d, as well as s and anti-s quarks: $\eta=\frac{1}{\sqrt{3}}(u\bar{u}+d\bar{d}-2s\bar{s})$. Its mean lifetime of $\tau=(5.0\pm0.3)\times10^{-19}s$ is shorter than

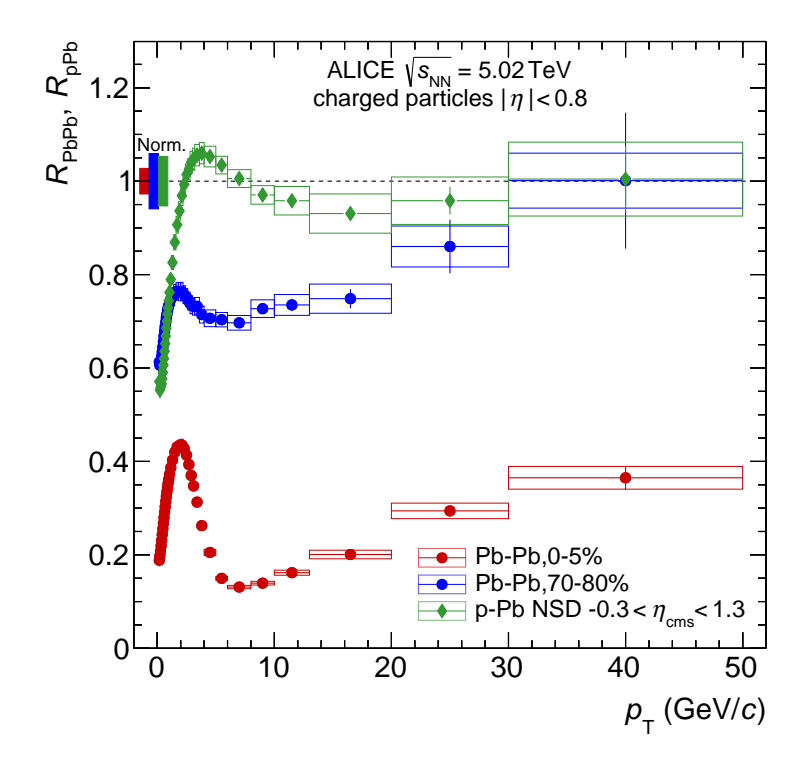


Figure 2.3: Nuclear modification factor $R_{\rm AA}$ for charged hadrons in central Pb–Pb and NSD p–Pb collisions [6].

that of the π^0 . Besides the primary decay channel into two photons with a branching ratio of 39.41 %, the η meson has additional significant decay channels, such as decay into three π^0 mesons with a 32.68 % probability, two charged pions and a neutral pion with a 28.1% probability, and two charged pions and a photon with a probability of 4.22 %.

Since π^0 and η are frequently produced in particle collisions, their high abundance enables high-precision measurements, providing detailed insights into various particle production mechanisms. Therefore, measuring these particles can open the possibility to study the strong interaction.

2.4.2 Nuclear Modification Factor (R_{AA})

One of the key results of the presented analysis is the measurement of the nuclear modiffication factor R_{AA} , which serves as a crucial observable for the QGP [1]. Whenever partons cross the QGP, they lose energy through radiation or collisions. The nuclear modification factor R_{AA} quantifies the differences in particle production in heavy-ion collisions compared to the superposition of individual nucleon-nucleon collisions. It is defined as the ratio of the measured yield in larger collision systems, like Pb–Pb, to a scaled binary collision yield at the same center-of-mass energy, as given in the following equation:

$$R_{\rm AA} = \frac{\mathrm{d}N^{\rm AA}/\mathrm{d}p_{\rm T}}{\langle N_{\rm coll}\rangle \mathrm{d}N^{\rm pp}/\mathrm{d}p_{\rm T}}.$$
 (2.4)

Here, $N^{\rm pp}$ and $N^{\rm AA}$ are the transverse momentum-dependent measured particle yields, and $\langle N_{\rm coll} \rangle$ is the scaling factor used for the pp reference spectrum. To assess the number of particles involved in a collision or selected events, one must rely on theoretical models, as femtoscopic length scales prevent the direct measurement of necessary parameters, such as the number of participating nucleons $N_{\rm part}$, the number of binary nucleon-nucleon collisions $N_{\rm coll}$, or the impact parameter b [1]. The Glauber Model, which describes the multiple scattering of nucleons in nuclear targets, can be used to estimate these parameters. A mapping procedure that correlates observed data with values calculated by the Glauber Model can be used to obtain the centrality of a collision. Once the correct $\langle N_{\rm coll} \rangle$ is determined, $R_{\rm AA}$ can be calculated [1].

Figure 2.3 shows previous ALICE measurements of $R_{\rm AA}$ for charged particles produced in p–Pb and both central and peripheral Pb–Pb collisions. In Pb–Pb collisions, a strong deviation from unity is observed across the entire transverse momentum range, with the suppression intensifying in more central collisions. Conversely, in p–Pb collisions, the nuclear modification factor remains close to unity at $p_{\rm T} > 4\,{\rm GeV}/c$, but falls below unity at lower $p_{\rm T}$. As shown by Equation 2.4, if $R_{\rm AA}=1$, the collision behaves as a straightforward superposition of independent binary particle collisions with no medium effects. However, an $R_{\rm AA}<1$ implies modifications due to a dense medium, such as the QGP, or other phenomena like cold nuclear matter (CNM) effects. The significant suppression in Pb–Pb but no observable suppression at higher $p_{\rm T}$ for p–Pb collisions suggests that the partonic energy loss in the medium is likely responsible for difference in suppression, since in both p–Pb and Pb–Pb collisions CNM effects are expected [6]. To further understand the influence of the CNM effects, the next section explores them in more detail.

Cold Nuclear Matter (CNM) Effects Modifications that occur in A-A collisions but not in pp collisions, and are unrelated to QGP formation, are commonly referred to as CNM effects. These effects stem from the presence of multiple bound nucleons within nuclei, which alter the parton momentum distribution. The momentum dis-

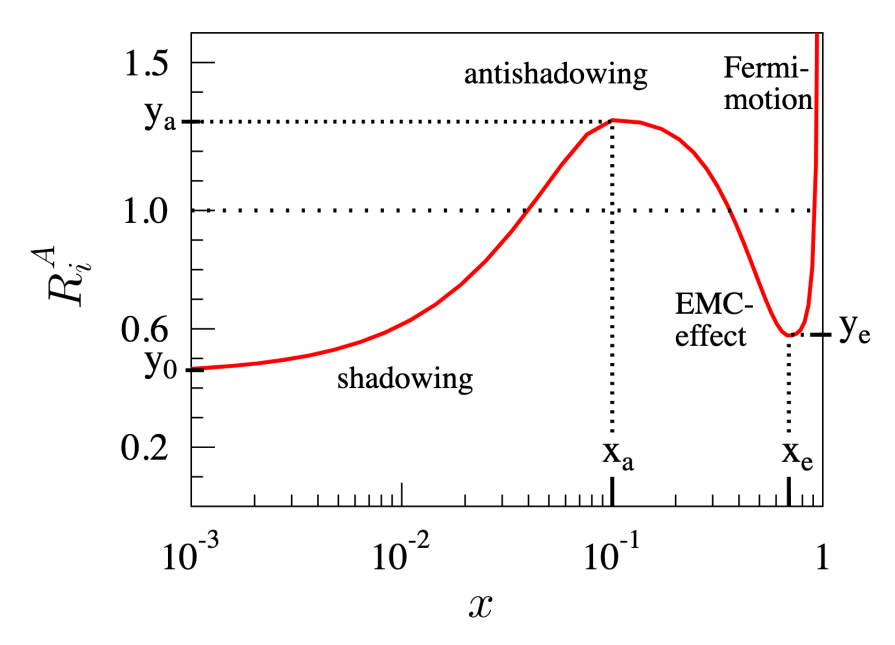


Figure 2.4: Modification of the parton distribution function with different x-dependent CNM effects [1].

tribution of partons is typically described by a parton distribution function (PDF), representing the probability that a parton carries a specific fraction x of the nucleon's total momentum, as shown in the following equation [1]:

$$f_{\mathbf{i}}^{\mathbf{A}}(x) = R_{\mathbf{i}}^{\mathbf{A}}(x) \cdot f_{\mathbf{i}}^{\text{free}}(x), \tag{2.5}$$

here, $R^{A}(x)$ describes the modification of the PDF, which can be observed in A-A collisions. Four primary x-dependent modifications of the PDF have been identified and are depicted in Figure 2.4:

- 1. Shadowing: The PDF is expected to be significantly suppressed for $x \lesssim 0.1$. This suppression is commonly attributed to the effect that nucleons bound in the center of the nucleus are shielded by outer nucleons [7].
- 2. Anti-Shadowing: An increase of the PDF is expected to occur for $0.1 \lesssim x \lesssim 0.3$.
- 3. EMC-Effect: For $0.3 \lesssim x \lesssim 0.8$ a suppression of the PDF is expected and has been observed by the EMC collaboration [8].
- 4. Fermi-Motion: Motions of nucleon are believed to lead to an increase of R_i^{A} for x > 1 [7].

These effects can impact the nuclear modification factor without implying the presence of a QGP. To study the QGP itself, photons offer insights into the medium's

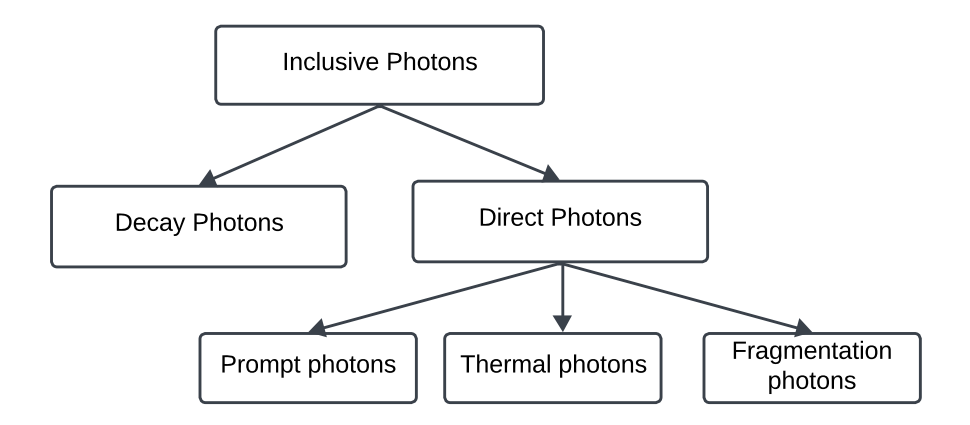


Figure 2.5: Schematic overview of different of photon sources.

characteristics.

2.4.3 Probing the QGP Using Photons

As discussed, the strong interaction dominates within the QGP. However, photons, which carry only an electromagnetic charge and no color charge, pass through the medium largely unaffected. Since the electromagnetic force is much weaker than the strong force, the photon's mean free path (500 fm) in the QGP is significantly longer than that of other particles (6 fm). This property makes direct photons an excellent tool for studying the plasma's evolution [1].

Photon sources are typically categorized by their production mechanisms. The total number of photons is referred to as inclusive photons, $N_{\gamma_{\rm incl}}$. These are further divided into decay photons, $N_{\gamma_{\rm dec}}$, and direct photons, $N_{\gamma_{\rm dir}}$, based on their origin. Decay photons result from the decay of particles after the collision, while direct photons are further classified into prompt, thermal, and other photons, depending on their production mechanism. Prompt photons are typically defined as those originating from hard parton collisions and parton fragmentation. At photon energies $E_{\gamma, \text{prompt}} > 4 \,\text{GeV}$, processes such as Compton scattering and quark-antiquark annihilation produce prompt photons, whereas at lower energies, soft photon radiation is the primary source.

Thermal photons are emitted by the charged constituents of the QGP during its evolution, with their production being limited by the temperature and the size of the emitting source [9]. These thermal photons dominate the direct photon spectrum

at low transverse momenta. As the QGP cools, the direct photon yield decreases. The third class of photons includes all other photon production mechanisms apart from decay photons, such as jet-medium interactions. A summary of all the photon sources is given in Figure 2.5. A complex analysis procedure is needed to measure direct photons as the measurement of a single photon does not reveal the production mechanism it originated from, e.g., whether it is a decay photon or a direct photon. One way to measure the direct photons is to calculate the so-called double ratio introduced in the next section.

2.5 Direct-Photon Measurement

A straightforward way to estimate the direct-photon yield is to subtract the decayphoton yield from the measured inclusive photon yield:

$$\gamma_{\rm dir} = \gamma_{\rm incl} - \gamma_{\rm dec}. \tag{2.6}$$

Here, the decay photon contribution is γ_{dec} and the inclusive photons are denoted as γ_{incl} . The expected photon decay spectrum is derived from an electromagnetic cocktail simulation based on the yield parametrization of mesons with photon decay branches. Table 2.3 lists the decay sources where the light neutral mesons are the dominant source. This calculation uses all available measured spectra of identified particles, while yields of unmeasured particles (e.g. η') are estimated using transverse mass scaling. A more detailed description of the estimation of the decay-photon sources considered in the presented analysis is given in Section 6.2.

While the subtraction method benefits from its conceptual simplicity, it is affected by significant systematic uncertainties. One approach to decrease the uncertainties is to calculate the excess ratio (R_{γ}) , which is calculated using the inclusive photon measurement together with the measured π^0 spectrum and the parameterized π^0 spectrum. The following equation shows how R_{γ} can be calculated via the measured spectrum π^0_{meas} and the parameterized spectrum π^0_{param} :

$$R_{\gamma} = \frac{(\gamma_{\rm incl}/\pi^0)_{\rm meas}}{(\gamma_{\rm dec}/\pi^0_{\rm param})_{\rm cocktail}}.$$
 (2.7)

Since π_{meas}^0 serves as the baseline for the parametrization of π_{param}^0 , systematic uncertainties cancel out, significantly reducing this source of error. This method also ensures the cancellation of all normalization factors, making the double ratio method

Decay channel	Branching ratio	$\gamma_{\rm source}/\gamma_{ m decay}$
$\pi^0 \to \gamma \gamma$	98.8%	$\approx 80\%$
$\eta \to \gamma \gamma$	39.4%	$\approx 15\%$
$\omega \to \pi^0 \gamma$	8.28%	$\approx 2\%$
$\eta' \to \rho^0 \gamma$	28.9%	$\approx 1\%$
$\phi \to \eta \gamma$	1.3 %	< 1 %%
$\rho^0 \to \pi^+ \pi^- \gamma$	$9.9 \times 10^{-3} \%$	< 1 %
$\Sigma^0 \to \Lambda^0 \gamma$	100 %	1 %

Table 2.3: Summary of hadronic decays that result in photon production.

one of the most experimentally promising approaches for measuring direct photons. Additional methods for direct-photon measurements are discussed in [1]. Results from previous direct-photon measurements using this technique are presented in the next section.

2.5.1 Related Work

Since this analysis does not present the first measurement of direct photons in ALICE or other experiments, this section briefly reviews prior measurements and their results. ALICE previously investigated direct photon production in Pb–Pb collisions at a center-of-mass energy of $\sqrt{s_{\rm NN}}=2.76\,{\rm TeV}$, in pp collisions at $\sqrt{s}=2.76$ and 8 TeV, and in p–Pb collisions at $\sqrt{s_{\rm NN}}=5.02\,{\rm TeV}$ for LHC Run 1 data [10]. The findings from some of these measurements are discussed in the following.

Figure 2.6 shows the ALICE measurement [10] of the excess ratio for three different centrality classes in Pb–Pb collisions at a center-of-mass energy of $\sqrt{s_{\rm NN}}=2.76\,{\rm TeV}$. The left side of the figure displays R_{γ} while the right side compares the direct photon spectrum in the $0-20\,\%$ centrality class for Pb–Pb collisions with that from Au–Au collisions at $\sqrt{s_{\rm NN}}=200\,{\rm GeV}$ measured with the PHENIX experiment. A clear R_{γ} signal above unity is observed for all centrality classes in the high $p_{\rm T}$ regions. The direct-photon yield on the right side is described by an exponential function in the low $p_{\rm T}$ region. This fit is used to extract the effective temperature of the QGP, yielding $T_{\rm eff}=304\pm11^{\rm stat}\pm40^{\rm sys}$ MeV. This temperature is significantly higher than that obtained from PHENIX measurements, approximately $T_{\rm eff}=239\pm25^{\rm stat}\pm7^{\rm sys}$ MeV in Au–Au collisions, and exceeds theoretical calculations discussed in Section 2.3.

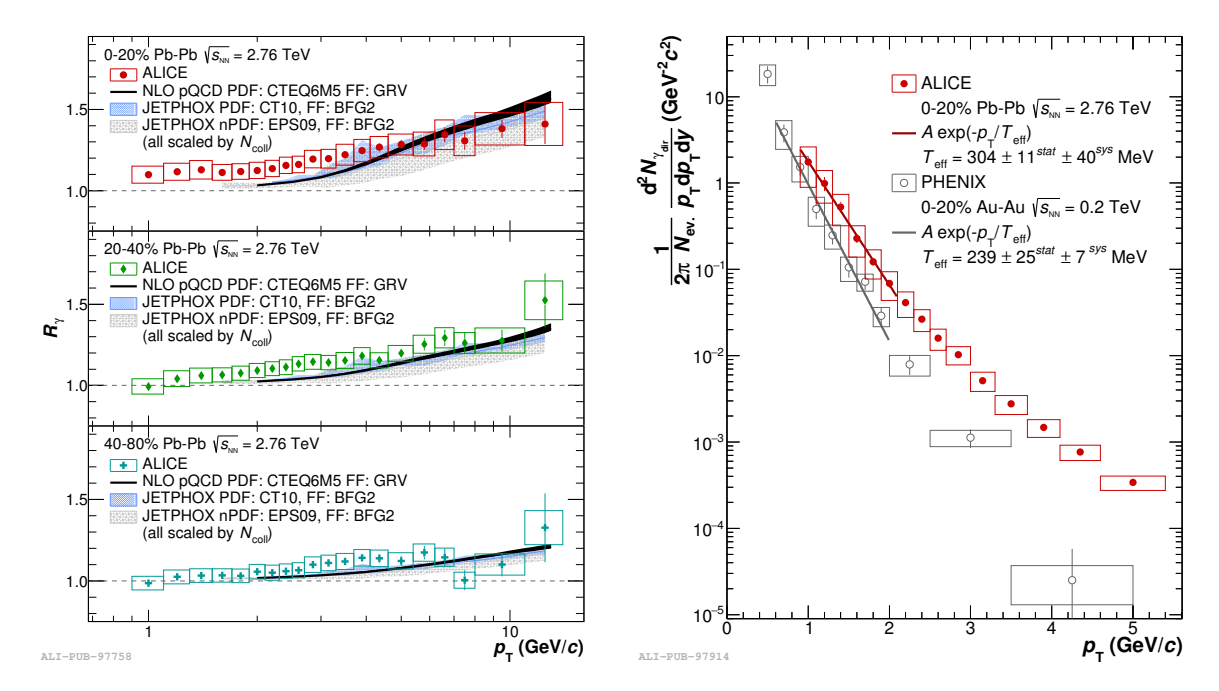


Figure 2.6: Left: R_{γ} for three different centrality classes in Pb–Pb collisions at $\sqrt{s_{\mathrm{NN}}} = 2.76\,\mathrm{TeV}$. The measurements are compared with theoretical predictions [10]. Right: Comparison of direct photon differential invariant yield in the most central collisions 0-20% Pb–Pb at $\sqrt{s_{\mathrm{NN}}} = 2.76\,\mathrm{TeV}$ and Au–Au collisions at $\sqrt{s_{\mathrm{NN}}} = 200\,\mathrm{GeV}$ [10].

3 Experiment

These theoretical debates, introduced in the last chapter, are studied by means of dedicated experiments in the field of particle physics. This analysis contributes to these discussions by utilizing data from ALICE, one of the four large experiments at the CERN LHC near Geneva, where particles such as protons or lead nuclei are accelerated and brought to collision [1]. This chapter provides a brief overview of the particle acceleration process and a description of the ALICE experiment, focusing on the subdetectors used in this measurement.

3.1 Particle Acceleration at the LHC

High-energy particle physics measurements rely on collisions of accelerated particles that allow the study of various particle species and matter in extreme conditions. The LHC accelerates protons and heavy ions to velocities close to the speed of light and to the highest energies currently possible. However, before reaching the LHC, protons and ions undergo pre-acceleration in a series of accelerators that incrementally increase their energy. In LHC Run 2 for protons, a maximum collision energy of $\sqrt{s} = 13 \,\text{TeV}$ is achieved, while for heavy ions, the highest center-of-mass energy per nucleon pair in Run 2 reached $\sqrt{s_{\text{NN}}} = 5.44 \,\text{TeV}$.

The acceleration process varies depending on the particle type, as illustrated in Figure 3.1. Protons are first accelerated in the Linac 2 before being filled into the Proton Synchrotron Booster (PSB). The heavy ions are accelerated in the linear accelerator, Linac and, in a second step, filled into the Low Energy Ion Ring (LEIR) accelerator [11, 12, 13]. The procedure to obtain the protons and ions differs depending on the atom that is used as the source for extracting the particles. At the Linac 2 the electrons get stripped off hydrogen atoms before being injected into the PSB. The heavy ions instead are obtained from an Electron Cyclotron Resonance Ion Source (ECRIS) [14]. Here, a Pb-gas by slowly heating a solid lead strip in micro-ovens. To obtain heavy ions, the electrons are, stripped from the lead ions by an external electric field. The strength of the field is adjusted depending on the type of ion (e.g., Pb, O, Xe, or In) [15].

To achieve high luminosities, the lead ions are stored in the LEIR accelerator, where their energy is increased from an initial kinetic energy of $E_{\rm kin} = 4.3 \,\rm MeV$ per nucleon and in the Linac 3 up to $E_{\rm kin} = 72.2 \,\rm MeV$ per nucleon [13].

Particles reaching the Proton Synchrotron (PS), follow the same acceleration process,

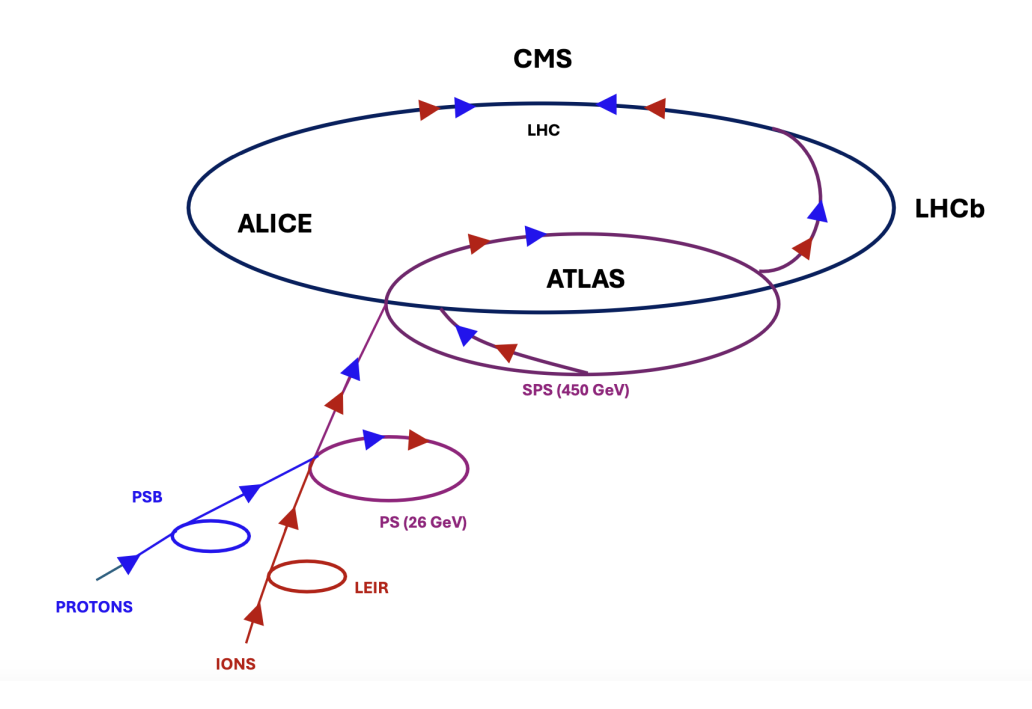


Figure 3.1: Schematic illustration of the various acceleration processes for both protons and lead nuclei.

regardless of particle type. Protons are accelerated to a kinetic energy of $E_{\rm kin}=5\,{\rm GeV}$ and Pb-ions $E_{\rm kin}=5.9\,{\rm GeV}$ per nucleon. Afterward the particles are filled into the Super Proton Synchroton (SPS), where individual particle bunches are accelerated from $E_{\rm kin}=450\,{\rm GeV}$ to $E_{\rm kin}=176.4\,{\rm GeV}$ per nucleon [16]. These particle bunches consist of up to 100 billion particles and are injected into the LHC in opposing directions. The potential spacing between bunches injected in the LHC is 7.5 m (25 ns). The collision occurs at four different interaction points in which the two beam lines intersect. The particles resulting from the collisions are recorded by the experiments built around the interaction points.

The CMS and ATLAS experiments, designed as complementary multipurpose experiments, were primarily built to study proton-proton (pp) collisions, with a particular focus on detecting the Higgs boson and exploring its properties [17, 18]. Beyond the Higgs boson, they also play a key role in probing physics beyond the Standard Model, such as the search for extra dimensions or supersymmetric particles (SUSY). In contrast, the LHCb experiment is dedicated to study CP violation in B meson decays [19]. The ALICE experiment is introduced in detail in the following section, as this analysis is based on data measured by ALICE.

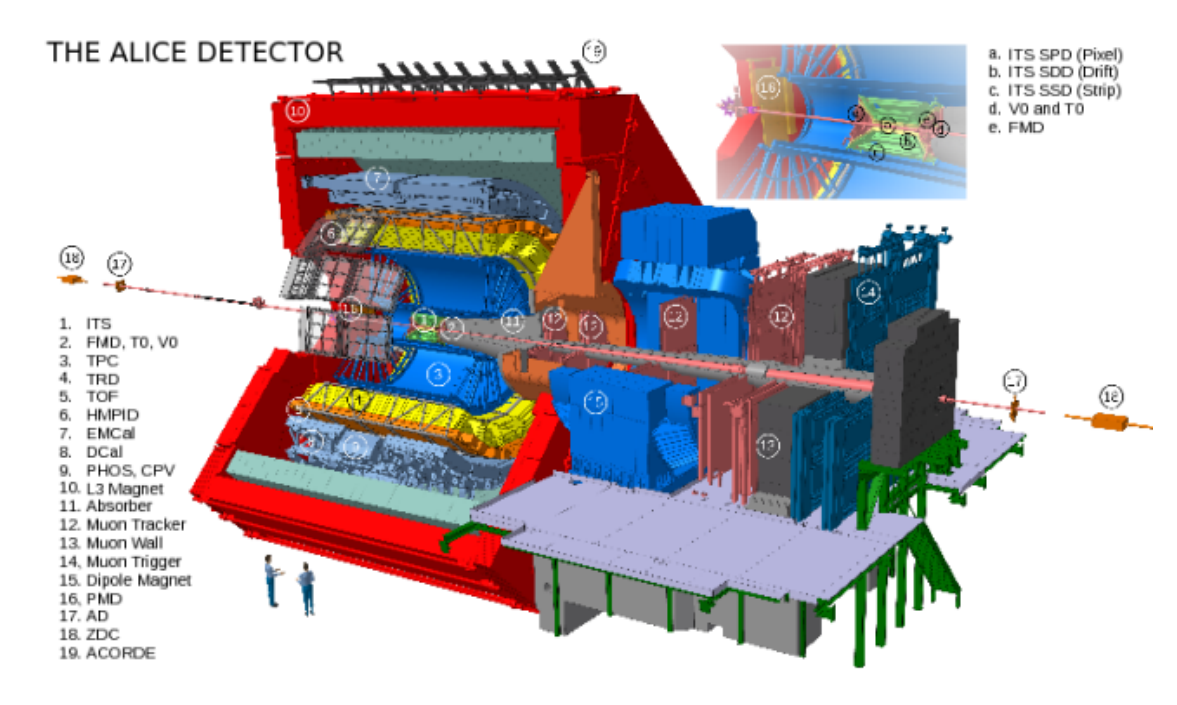


Figure 3.2: Schematic overview of the ALICE experiment and its 19 subdetectors [20].

3.2 The ALICE Experiment

The ALICE experiment spans 16 m x 16 m x 26 m and is located 56 m below the Earth's surface. It is a general-purpose experiment for studying heavy-ion collisions [15]. AL-ICE is optimized to investigate matter at high densities and temperatures, specifically to probe properties of the QGP. This research focus places specific demands on the design of the experiment's detectors, which must provide high resolution in low transverse momentum regimes, excellent particle identification (PID), and be capable of handling high particle multiplicities. Figure 3.2 shows a schematic overview of the experiment, including its 19 subdetectors active during LHC Run 2 and Table 3.1 summarizes the coverage and purpose of selected detector systems [15]. The detectors in the experiment are divided into three main categories that are indicative of their measurement capabilities. The Inner Tracking System (ITS), Time Projection Chamber (TPC), Transition Radiation Detector (TRD), and the Time-Of-Flight (TOF) are counted as central barrel detectors and are used for charged-particle measurements. These detectors are surrounded by a solenoid magnet, which generates a magnetic field of up to 0.5 T. The field is oriented parallelly to the beam axis and curves the trajectory of charged particles depending on their charge and momentum. The second subclass of detectors are the muon detectors, which are positioned outside the magnet. The last group of the detectors are the so-called group of forward detectors, which

Detector	Pseudo- rapidity	Azimuthal coverage	Radial distance (cm)	Purpose
ITS				
SPD	$ \eta < 2$	full	3.9, 7.6	tracking, vertex
SDD	$ \eta < 0.9$	full	15, 23.9	tracking, PID
SSD	$ \eta < 0.97$	full	38, 43	tracking, PID
TPC	± 0.9	full	84, 240	tracking, PID
TRD	± 0.84	full	290, 368	tracking, PID
TOF	± 0.9	full	378	PID
PHOS	± 0.12	$220^{\circ} < \phi < 320^{\circ}$	460	photons
EMCal	± 0.7	$80^{\circ} < \phi < 187^{\circ}$	436	photons
V0	$2.8 < \eta < 5.1$	full	340	trigger, centrality

Table 3.1: Selection of the detector systems included in the ALICE experiment. Additionally, their coverage and their main purpose are outlined [15].

are located partially inside and outside the red solenoid.

For this analysis data is drawn from the ITS, TPC, the V0, and the PHOS, which will therefore be discussed in depth in the following sections.

3.2.1 V0 Detector

The V0 detector as part of the forward detectors plays a key role in determining centrality in p–Pb collisions. Located in front of the ITS, it consists of two arrays of scintillating counters: V0A and V0C. These detectors cover a wide pseudorapidity range, with V0A spanning $2.8 < \eta < 5.1$, and V0C covering $-3.7 < \eta < -1.7$. In this analysis, the V0 detector classifies minimum bias samples by requiring coincidental signals from both V0A and V0C, and serves as a centrality trigger [21].

3.2.2 Inner Tracking System (ITS)

The primary objective of the ITS is to determine the position of the primary collision vertex and distinguish it from secondary vertices. This is achieved primarily by the two innermost layers of the ITS, the Silicon Pixel Detector (SPD), which are placed as close as possible to the beam pipe ($R=3.9\,\mathrm{cm}$), providing a vertex resolution of 100 µm. Secondary vertices, such as those formed when photons convert into electron-positron pairs upon crossing the beam pipe, can therefore be identified and allow for the photon reconstruction. Since those conversions happen close to the primary vertex, they leave a signal in the outer layers of the ITS, which can be used to reconstruct those vertices.

Their analog readout allows for energy loss measurements of low-momentum particles. Thus, the ITS plays a crucial role in track reconstruction for low-momentum particles. However, full track reconstruction also relies on data from the TPC.

3.2.3 Time Projection Chamber (TPC)

The TPC serves as the primary detector for tracking and identifying charged particles. Positioned between the ITS and the TRD, the cylindrical TPC covers the full azimuthal angle and a pseudorapidity range of $|\eta| < 0.9$ [22].

The volume of the TPC is filled with a specific gas mixture, enabling the reconstruction of charged-particle tracks as they ionize the atom's of the gas along their path. A uniform electric field, generated by a high-voltage electrode at $\eta=0$ and z=0, causes the freed electrons from ionization processes to drift toward the TPC endplates at a constant velocity. Upon reaching the endplates, the arrival time and x-y coordinates of the electrons are recorded, allowing the determination of the initial ionization position. The particle's transverse momentum is calculated from the track curvature, with primary tracks covering a momentum range of $100\,\mathrm{MeV}/c < p_\mathrm{T} < 100\,\mathrm{GeV}/c$ [22]. To identify charged particles, the TPC also measures their energy loss in the gas. The energy loss per unit path length $(\mathrm{d}E/\mathrm{d}x)$ for inelastic scattering follows a Bethe-Bloch-like formula, allowing for particle identification [22].

A detailed description of photon reconstruction with the particle identification capabilities of the TPC can be found in Section 4.2.1. However, the primary technique for the measurement of photons involves electromagnetic calorimeters, one of which will be introduced later in this chapter.

3.2.4 Photon Spectrometer (PHOS)

The PHOS is positioned at the bottom of the ALICE experiment, at a distance of 460 cm from the collision point. During LHC Run 2, the detector consisted of three full-sized modules and one half-module, covering a pseudorapidity range of $-0.12 < \eta < 0.12$ and an azimuthal angle of $250^{\circ} < \phi < 320^{\circ}$ [23].

The PHOS offers high granularity, with each full module composed of 64×56 lead tungstate (PbWO₄) crystals, and the half-module containing 32×56 crystals, totaling 12.544 crystals. This design allows for high precision measurements of low energy photons, especially since the material budget in front of the detector has been kept to a minimum. Figure 3.3 shows the module layout in detail [23]. The measurement

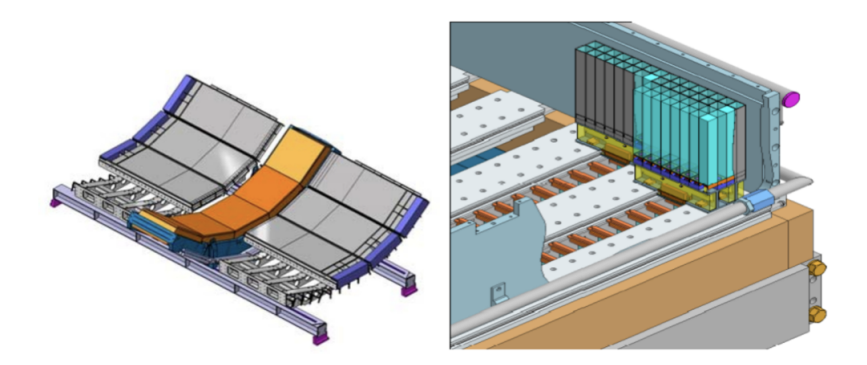


Figure 3.3: *Left:* Schematic overview of the PHOS detector with its original five detector modules. *Right:* Zoom into the installation and design of the PHOS cells.

capabilities of the PHOS detector rely on detecting electromagnetic showers produced by electrons, positrons, and photons. These showers are generated when photons convert within the detector material and by Bremsstrahlung. The likelihood of photon conversion depends on two factors: the distance traveled through the material (X)and the average radiation length (X_0) , as given in the following equation:

$$P(X) = 1 - e^{-\frac{7}{9} \cdot \frac{X}{X_0}}. (3.1)$$

This relationship shows that the probability of photon conversion increases with the amount of crossed detector material. When photons convert, they produce electrons and positrons that interact with the material, emitting Bremsstrahlung, which in turn generates more electrons and perpetuates the process. This cycle continues until the showering particles reach a lower energy bound, where instead of emitting more Bremsstrahlung, the electrons excite the valence electrons in the material, producing scintillating light. This light is measured by a so-called avalanche photodiode (APD), which produces an electric signal that is proportional to the energy of the incident particle.

The propagation of the electromagnetic shower inside the calorimeter occurs along the longitudinal axis. Two key factors determine the energy resolution: the length and surface area of the calorimeter cells. The length affects energy resolution, while the surface area influences spatial resolution. The shower must spread across multiple cells for its position to be accurately determined. The spread of the shower is described by the Molière radius:

$$R_{\rm M} = 0.0265 \cdot X_0 \cdot (Z + 1.2), \tag{3.2}$$

where Z is the atomic number of the atoms in the crystals. To ensure high spatial and energy resolution, the surface area of the cells is designed to be close to the Molière radius, allowing the shower to spread across multiple cells. To reduce noise and further enhance resolution of the PHOS detector the APD, preamplifiers, and crystals are cooled to -25° C.

3.3 ALICE Software Framework

Measurements in ALICE rely on a central software framework for the reconstruction, data processing, and analysis. The framework is based on ROOT [24], which is developed at CERN for the special purpose to analyze vast amounts of data from different high-energy experiments. The ALICE specific framework is split into two distinct software parts, AliRoot and AliPhysics. While AliRoot offers an interface between different Monte Carlo generators, detector simulations and track reconstruction, AliPhysics includes the physics analysis code. In addition to these components, a specifically designed post-processing software framework developed by the ALICE conversion photon group is used and extended for this particular analysis.

4 Data Preselection

This chapter presents the analyzed data sets and the criteria used to select collision events and photons with high purity. The selection criteria for the two photon reconstruction methods, PCM and PHOS, are based on previous studies [25, 9] and refined for this analysis.

4.1 Data Sets and Event Selection

The goal of this analysis is to measure direct photons using the PCM-PHOS reconstruction method in p–Pb collisions at a center-of-mass energy of $\sqrt{s_{\rm NN}}=5.02\,{\rm TeV}$. These data were recorded during the second run of the LHC in 2016. In ALICE, datasets are typically organized into periods where key experimental conditions, such as the collision system and energy, remain constant. During LHC Run 2, four p–Pb data periods were recorded, two of which — LHC16q and LHC16t — at $\sqrt{s_{\rm NN}}=5.02\,{\rm TeV}$. The presented results combine these two periods and the combined data set is referred to as LHC16qt. Table 4.1 shows a summary of the analyzed data sets. This table also includes the MC data sets which are used for the correction of the data which will be explained in the following.

Each period is further divided into runs, representing continuous data-taking intervals. For this analysis, only runs are selected where both the ITS and TPC were fully operational to enable the photon reconstruction with the PCM method. Additionally, only runs where the PHOS detector was actively recording data are included in the analysis. A detailed list of selected runs can be found in Appendix 8.1.

To only select physically meaningful events, the following criteria have to be fulfilled:

- Only events that passed the Physics Selection (PS) in AliPhysics are included in the analysis to suppress beam induced background.
- Only events with one vertex in the SPD are included in the analysis. Multiple reconstructed vertices typically indicate a pileup event, which may arise from multiple collisions during the same bunch crossing. Additionally, this signature in the SPD can be caused by particle interactions with the beam pipe or the gas inside it.
- An additional event selection criterion is based on the correlation between SPD tracklets and SPD clusters. Normally, a roughly proportional relationship

	Dataset	$N_{\rm evt} \ ({\rm x} \ 10^8)$
Data	LHC16qt	4.9
MC	LHC18f3	5.5

Table 4.1: Number of events (N_{evt}) for analysis in data and MC.

between tracklets and clusters is expected. However, if an event shows a high number of clusters but relatively few tracklets, it is excluded from the analysis as a background event. This relationship is described by the following expression:

$$N_{\text{tracklets}} > \frac{N_{\text{clusters}} - 65}{4}.$$
 (4.1)

Only events fulfilling this requirement are included in the presented analysis.

• Last, only events where the primary vertex of the considered event is reconstructed less than 10 cm apart from the nominal interaction point are considered for reconstruction. This criterion ensures that a significant portion of the produced particles pass through the active areas of the central barrel detectors. The number of remaining events after selection is shown in Table 4.1.

While these selection criteria enhance data quality for physics analysis, detector effects still alter the observables. Therefore, data analysis requires corrections for these effects, typically addressing three types of detector responses: kinematic acceptance and efficiency losses, or reductions in the purity of particle selection. These corrections are typically implemented using Monte Carlo (MC) simulations, which generate data by modeling particle production with event generators. The particles are then propagated through a virtual representation of the ALICE detector, which allows assessing effects of the detector response.

One type of MC simulation models the particle production process. The event generators most widely used in ALICE are PYTHIA8, PHOJET, DPMJet-III, and EPOS LHC, each modelling the underlying physical principles of particle production differently. The MC with the highest number of generated events for p-Pb collisions in ALICE at this center-of-mass energy, was selected for the analysis as it minimizes statistical uncertainties in the extracted corrections. This simulation employs DPMJet as the event generator.

Once the particles are generated by the event generators, the simulation propagates them through the detector material. The GEANT3 package facilitates the modeling of particle interactions with the detector by incorporating the specific layout and material properties of the detectors. The combination of the DPMJet event generator and the GEANT3 simulation forms the basis for the LHC18f3 MC data, which is utilized for correction purposes in this analysis.

In the selected events, photons have to be identified for the measurement of neutral mesons and direct photons. The reconstruction methods and selection criteria used will be discussed in the following section.

4.2 Photon Reconstruction Methods

To reconstruct and identify the particles produced in the collision, ALICE is equipped with a set of detectors as outlined in Section 3. This chapter introduces two photon reconstruction approaches relevant to this analysis: the PCM and PHOS methods. Neutral mesons are measured through their decay into two photons. The combination of both reconstruction approaches, where one photon is measured in PHOS and one via the PCM, allows for a wide $p_{\rm T}$ range of meson momenta and is referred to as PCM-PHOS method.

This section now discusses the photon reconstruction techniques and introduces photon selection criteria that are applied in the reconstruction process. These criteria enhance the purity and are vital to improving the quality of the measurement.

4.2.1 Photon Conversions

Reconstruction This method relies on detecting photons that convert into an electron-positron pair. As discussed in Section 3.2.4, the photon conversion usually occurs due to scattering processes with a nucleus in the detector material. The resulting decay topology features two charged particle tracks originating from a secondary production vertex at a distance R from the primary collision vertex, with no direct connection between the two vertices as visualized in Figure 4.1.

Due to the distinct topology of these conversions, an algorithm is used to reconstruct the decay of neutral particles into two oppositely charged tracks. This algorithm is known as the V^0 finder.

For all oppositely charged tracks with the required decay topology, the distance of closest approach (DCA) between the two tracks is calculated. Only particles with a DCA of less than 1 cm are selected as V^0 candidates for the further analysis. This ensures that the tracks stem from secondary vertices rather than primary vertices.

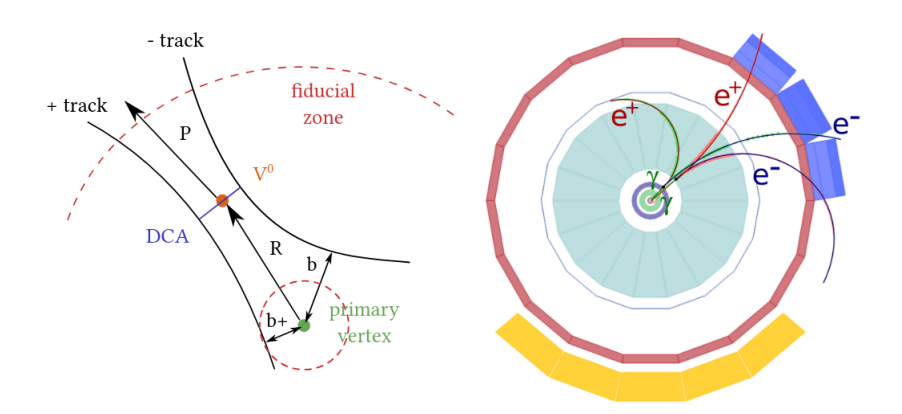


Figure 4.1: Left: Schematic visualization of the secondary vertex reconstruction from two charged tracks [26]. Right: Schematic visualization of the reconstruction of the π^0 candidate from two photons converting into electron and positron [26].

Additionally, the reconstruction is confined within a fiducial zone, extending radially from 5 cm to 180 cm from the primary vertex. The algorithm extrapolates the momentum vectors of the two tracks to the DCA and sums them to determine the momentum of the neutral particle. V⁰ candidates are included in the analysis only if their momentum vector points toward the primary vertex. This condition is satisfied when the cosine of the angle (θ_{PA}) between the V⁰ momentum and the vector connecting the secondary and primary vertex R has a value of less than 0.85.

For the reconstruction of neutral mesons and direct photons, additional selection criteria for the tracks, photons and charged particles are applied, which will be discussed in the following section.

Track Selection and PID The track selection and PID criteria are summarized in Table 4.2. All selection criteria are applied to the secondary tracks of the V^0 candidates. All tracks should not exhibit any kink topology. To ensure tracks reach the TPC, the minimum transverse momentum is set to $p_{T,track} = 0.05 \,\text{GeV}/c$.

To only select tracks where it is ensured that the full track length can be reconstructed in the ITS and TPC, a pseudorapidity selection of the tracks of $|\eta| < 0.8$ is chosen. Here, η is the pseudorapidity, which depends on the angle between the beam axis and the particle's momentum vector in the transverse plane. However, since many particles could meet this criterion without being reconstructed inside the TPC, an additional constraint is imposed: the conversion radius, $R_{\rm conv}$, must be less than 180 cm, and the longitudinal position, $Z_{\rm conv}$, must be less than 240 cm to ensure the secondary tracks

$\overline{ ext{Track and } ext{V}^0 ext{ Criteria}}$	
$\overline{{ m V}^0}$ finder	On-the-fly
Minimum track $p_{\rm T}$	$p_{\mathrm{T,track}} > 0.05 \mathrm{GeV}/c$
$N_{ m Cluster TPC}/N_{ m find TPC}$	> 60 %
R_{conv}	$5 \text{cm} < R_{\text{conv}} < 180 \text{cm}$
$Z_{ m conv}$	$ Z_{\rm conv} < 240{\rm cm}$
η	$ \eta < 0.8$

Table 4.2: Standard track and V^0 selection criteria used in the neutral meson and direct photon analysis.

Cut	Condition
$\frac{\mathbf{n}\sigma_e \text{ TPC d}E/\mathbf{d}x}{\mathbf{n}\sigma_\pi \text{ TPC d}E/\mathbf{d}x}$	$-3 < n\sigma_e < 4$ $0.4 {\rm GeV}/c < p_{\rm T} < 3.5 {\rm GeV}/c$: $n\sigma_{\pi} > 2.5$ $p_{\rm T} > 3.5 {\rm GeV}/c$: $n\sigma_{\pi} > -2.5$

Table 4.3: Selection criteria for the electron and pion identification. The range indicates the range within the particles are kept for the analysis.

are contained within the TPC barrel. To further minimize contamination from Dalitz decays of the neutral mesons, $R_{\rm conv}$ is chosen to be bigger than $R_{\rm conv} < 5\,{\rm cm}$ of both π^0 and η meson measurement.

Electron Identification To ensure that only photons are included in the V⁰ sample, additional selection criteria are applied to identify electrons and reject pions. The selection mainly relies on the dE/dx information provided by the TPC.

The specific criteria used in this analysis are summarized in Table 4.3. These criteria are designed to minimize contamination while maintaining efficiency. They are applied around the expected values for the energy loss of electrons and pions, with the electron selection set to $n\sigma_e = 5$ inside the predicted electron energy loss.

To further optimize particle identification, an additional pion rejection is performed, with criteria varying by momentum region. For low momentum up to $p_{\rm T}=3.5\,{\rm GeV}/c$, tracks with energy losses outside ${\rm n}\sigma_{\pi}=1$ are rejected, while at higher momentum, all tracks are retained. The influence of the selection criteria on the included particles are shown in Figure 4.2.

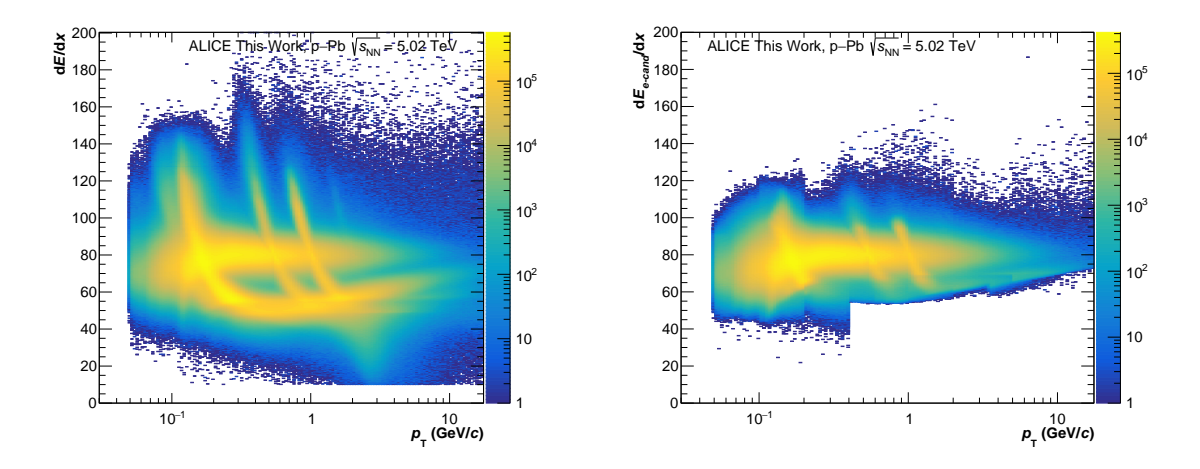
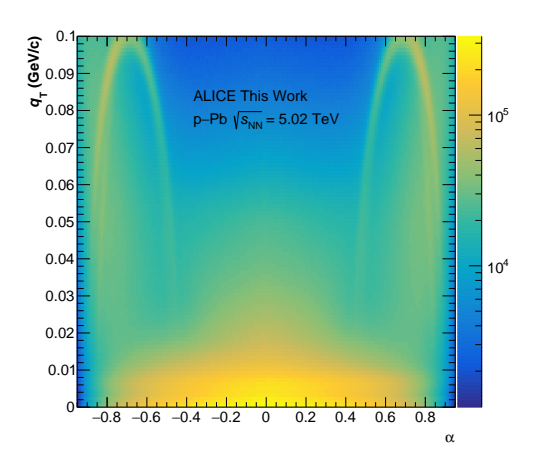


Figure 4.2: Left: The TPC dE/dx plot for the V⁰ daughters before the electron selection criteria are applied. Right: The TPC dE/dx plot for the V⁰ daughters after the electron selection criteria are applied.

Photon selection	
χ^2/ndf	2D triangular cut with $\chi^2/\text{ndf} < 30$ and $\psi_{\text{pair}} < 0.1$
$q_{ m T}$	2D elliptical cut with $q_{\rm T} < 0.05{\rm GeV}/c$ and $\alpha_{\gamma} = 0.95$
$\cos(heta_{ ext{PA}})$	> 0.85

Table 4.4: Photon selection criteria for the PCM method.

Photon Selection To increase the purity of the V⁰ photon candidates, additional selection criteria are applied. The reconstruction algorithm aims to detect the particles based on their topology. Other decays such as $\Lambda^0 \to p^+\pi^-$ or $K_S^0 \to \pi^+\pi^-$ can be mistakenly identified as an electron-positron pair. One can therefore implement selection criteria which aim to restrict the photon selection based on their conversion topology. Table 4.4 summarizes the photon selection criteria applied in the presented analysis. To suppress the background from decays of heavy particles, regions in the socalled Armenteros-Podolanski plane are selected. The Armenteros-Podolanski plane combines two kinematic variables: $q_{\rm T}$, which describes the relative momentum of the daughter particles with respect to the V^0 and α , which indicates the longitudinal asymmetry of the oppositely charged daughter particles. The Armenteros-Podolanski plane is shown in Figure 4.3. As the electron-positron pair originates from a massless photon, a small opening angle for the particles is expected and hence low $q_{\rm T}$ values. The values for α are also low since both the electron and positron have identical masses. With these considerations in mind, one can thus minimize the background in the sample of V^0 candidates as decays into heavier particles which lead to higher



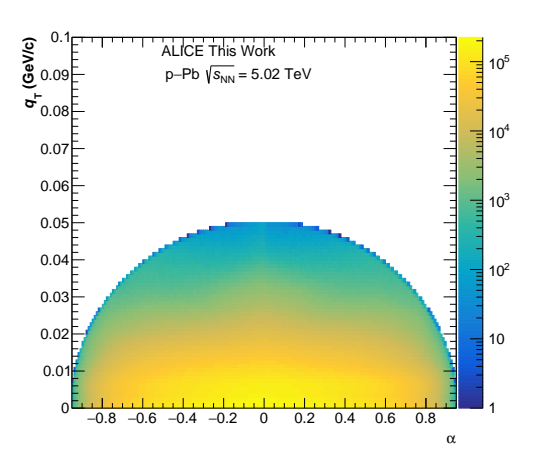


Figure 4.3: *Left:* Armenteros Podolanski plane for the V⁰ candidates before the photon selection criteria are applied. *Right:* Armenteros Podolanski plane after applying the photon selection criteria.

values in both variables. After applying the respective selection criteria, the amount of considered particles reduces to the distribution on the right-hand side of the figure. For this analysis, a two-dimensional selection of the photons is applied where a maximum value of $q_{\rm T,max} = 0.05\,{\rm GeV}/c$ is used.

Further suppression of the background is achieved by implementing a two-dimensional selection in χ^2/ndf and ψ_{pair} . The χ^2/ndf selection criteria is based on the goodness of track hypotheses of the Kalman filter which is used for the reconstruction. The ψ_{pair} selection criterium uses the fact that the orientation of the decay is correlated with the direction of the magnetic field as the electron and positron are bent in opposite direction of the magnetic field and produced at nearly zero relative momentum. The associated geometric variable, ψ_{pair} , is then defined as the angle between the plane spanned by the two charged tracks and the plane perpendicular to the magnetic field, as can be seen in the left panel of Figure 4.4. For signal pairs, the ψ_{pair} distribution is centered around 0 with a significantly narrower width compared to V⁰ candidates arising from combinatorial background. By forcing a limit to the relative electron positron opening angle, one can thus suppress photons from π^0 -Dalitz decays.

4.2.2 Calorimetry

Reconstruction The second photon reconstruction method used in this analysis involves the PHOS detector. In the calorimeter, the energy deposited by a photon is measured. As explained in Section 3.2.4, photons interacting with the calorime-

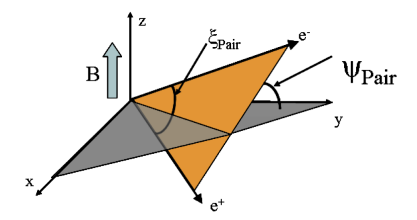


Figure 4.4: Schematic visualization of the ψ_{pair} angle as the angle between the plane of the electron and positron pair and the plane of the magnetic field in gray [26].

ter induce electromagnetic showers through processes such as pair production and Bremsstrahlung. Depending on the incident angle and energy of the particles, the produced showers may spread across multiple calorimeter cells. To accurately reconstruct the energy, the deposited energy from multiple cells must be combined into a cluster through a process known as clusterization. For the clusterization, however, only cells that fall within the accepted time interval and whose energy exceeds a certain threshold are selected. The PHOS clusterization algorithm follows six distinct steps:

- 1. Cells are sorted based on their energy.
- 2. The cell with the highest energy is chosen as the reference point to initiate the clusterization process. The energy of this leading cell (E_{seed}) must exceed a threshold of $E_{\text{seed}} > 50 \,\text{MeV}$.
- 3. If the cell energy (E_{cell}) of adjacent cells exceed the threshold $E_{\text{cell,min}} = 15 \,\text{MeV}$ then these cells are aggregated into the cluster.
- 4. Step 3 is repeated until no adjacent cells meet the energy requirement $E_{\text{cell}} > E_{\text{cell,min}}$.
- 5. Steps 2–4 are repeated as long as the leading cell's energy satisfies $E_{\rm seed} > E_{\rm seed,min}$.
- 6. After all leading cells have been processed, the clusterization is complete.

Once the clusters are formed, the energy, position and shape of the cluster can be calculated. To calculate the energy of the cluster, the following relation is used:

$$E_{\text{cluster}} = \sum_{i}^{N} E_{\text{cell,i}}, \tag{4.2}$$

where N is the total amount of cells forming the cluster and $E_{\text{cell,i}}$ is the energy contributions from the individual cells. The cluster position is determined using the η - ϕ coordinates of the cells within the cluster weighted by a factor w that depends on the cell energies, as described by the following equation:

$$x_{\text{cluster}} = \frac{\sum_{i}^{N} w_i \cdot x_{\text{cell},i}}{\sum_{i}^{N} w_i}.$$
 (4.3)

The shape of the cluster is characterized by the so-called shower shape parameter M_{02} , which is defined as:

$$M_{02} = \sum_{i}^{N} \left(x_1^{(i)} \right)^0 \cdot \left(x_2^{(i)} \right)^2 E_{\text{cell,i}}, \tag{4.4}$$

where i again is running over all cells that form the cluster and $E_{\text{cell,i}}$ is the energy of the respective cell. The main use for the shower shape parameter is to discriminate between electromagnetic, hadronic or overlapping showers. To further minimize measurement distortions, the cluster energy is calibrated using an absolute energy scale which accounts for the non-linear energy response of the calorimeter. The parameters for these calibrations are determined by previous test-beam experiments.

It should be noted that the cell aggregation process continues as long as the condition $E_{\text{cell}} > E_{\text{cell,min}}$ is satisfied. This can sometimes result in overlapping clusters due to continuous aggregation. To identify such cases, the number of cells above the seed threshold are determined. If a cluster contains more than one such cell, it is assumed to consist of multiple overlapping showers. The cluster is then split into multiple clusters, using the cells with maximum energy as the seeds for the new clusters, which are subsequently unfolded. Once the cluster is unfolded, the energy position and shape of a cluster need to be recalculated.

Photon Selection In addition to electrons, positrons, and photons, other particles such as π^{\pm} , K^{\pm} , (anti)protons and (anti)neutrons can deposit portions of their energy

Cluster reconstruction	
Minimum cell energy	$E_{\rm cell,min} = 15 \mathrm{MeV}$
Minimum cell energy	$E_{\rm seed,min} = 50 \mathrm{MeV}$
Cluster selection	
Minimum cluster energy	$E_{\rm cluster} > 300 {\rm MeV}$
Minimum number of cells	$N_{ m cluster}^{ m cells} > 2$
Cluster time	$-50\mathrm{ns} < t_{\mathrm{cluster}} < 50\mathrm{ns}$
Cluster shape	$M_{02} > 0.1$
Cluster-track matching $\Delta \eta \ \Delta \phi$	p_{T} dependent
Cluster-track matching $\Delta \eta \Delta \phi$	$p_0 = 0.05, p_1 = 0.005, p_2 = 3.0$

Table 4.5: Standard selection criteria for the cluster reconstruction with PHOS used throughout this analysis.

in the calorimeter, producing hadronic showers and contributing unwanted background to the photon candidate sample. To enhance the photon reconstruction purity, this analysis employs several selection criteria for photon identification.

To ensure a precise measurement of the energy, timing, and position of the detected particles, several selection criteria are applied on cluster level. To exclude signals from detector noise, each cluster must consist of at least two cells. To further reduce electronic background, the minimum cluster energy is set to 300 MeV. Additionally, to mitigate the effects of pileup from previous events, cluster timing selection criteria are applied by comparing the cluster's relative time with the event timestamp. The cluster time is typically determined using the highest-energy cell of the cluster, known as the cluster seed. For p-Pb collisions, the cluster time selection is commonly set to $-50 < t_{\text{cluster}} < 50 \,\text{ns}$. This window minimizes contamination from particles from previous events while remaining large enough to capture sufficient signal as the bunch spacing is commonly set to 100 ns. Furthermore, a cut based on the shower shape parameter M_{02} is applied, where $M_{02} > 0.1$ is required for PHOS clusters. For smaller M_{02} values, there is a significant contribution from exotic clusters. These clusters are likely caused by slow neutrons striking the electronics of the readout chip, depositing energy in a single cell. Due to cross-talk, this energy can propagate to neighboring cells through leakage in the readout cards. As a result, these clusters typically exhibit one cell containing over 95 % of the total cluster energy, yielding an M_{02} value close to 0 [27].

In addition to requirements for the cluster energy and shape, further selection criteria,

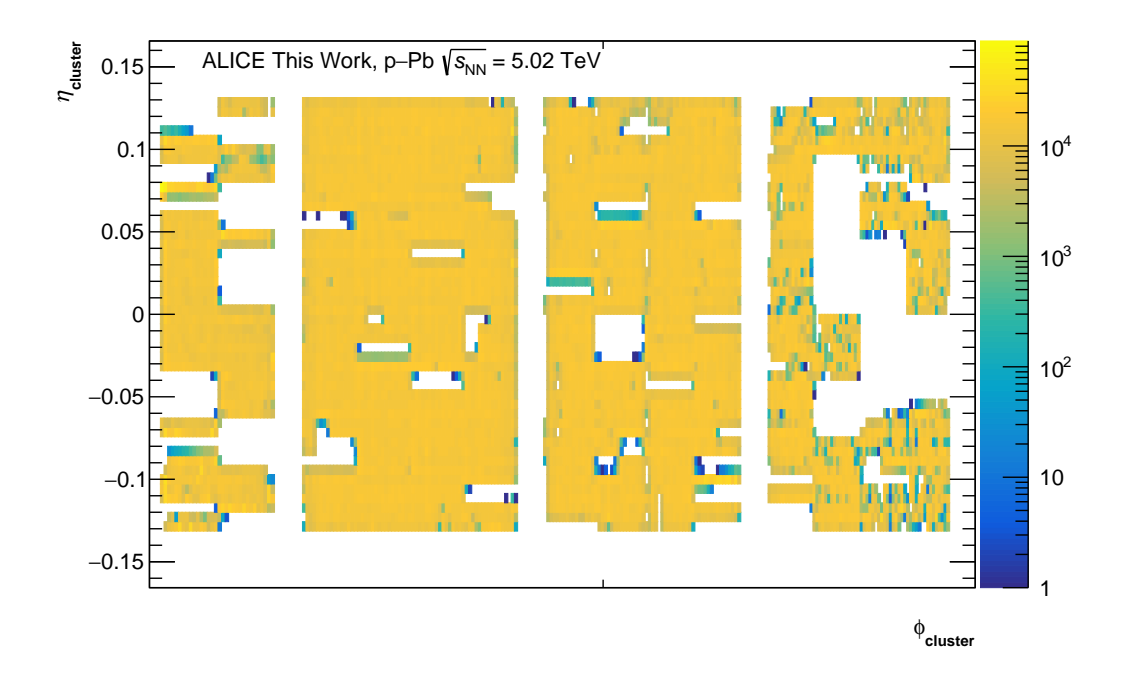


Figure 4.5: $\eta - \phi$ distribution of all selected clusters after the cluster and cell quality assessment was performed.

listed in Table 4.5, are applied to minimize contamination from other particles like electrons and positrons. Since charged particles leave tracks in the TPC, these tracks can be propagated to match clusters in the PHOS detectors. If a track points to a cluster, the track is rejected. To exclude clusters associated with charged particles, only clusters that have a minimal distance from the extrapolated track are included in the analysis. This minimal distance depends on the transverse momentum of the track, which can be described by the following function

$$f_{\eta,\phi}(p_{\rm T}) = p_1 + \frac{1}{\left(p_{\rm T,track} + \left(\frac{1}{p_0 - p_1}\right)^{\frac{1}{p_2}}\right)^{p_2}},$$
 (4.5)

where p_0 , p_1 , and p_2 are free parameters. The whole expression depends on the transverse momentum of the charged tracks $p_{\rm T,track}$ as the track extrapolation to the PHOS is worse at lower transverse momenta. This momentum-dependent function allows the calculation of boundaries for accepted tracks. A summary of the selection criteria used in this analysis is provided in Table 4.5, while Figure 4.5 illustrates the $\eta - \phi$ distribution of clusters that meet these criteria.

The reconstructed V⁰ candidates and photon clusters can now be used for the recon-

struction of the neutral mesons. The specific analysis procedure for their reconstruction and the obtained results will be discussed in the section that follows.

5 Neutral-Meson Measurement

As previously described in Section 2.4.2 and Section 2.5, the measurement of the neutral meson nuclear modification factor as well as the photon excess ratio relies on the precise measurement of the light neutral meson yields. This section, therefore, describes the measurement of the neutral pion and η meson in p-Pb collisions at a center-of-mass energy of $\sqrt{s_{\rm NN}} = 5.02\,{\rm TeV}$.

Although neutral mesons have been measured and published [28] using both the PHOS and PCM technique at this center-of-mass energy, their measurement via the PCM-PHOS technique was not feasible with the limited statistics of the LHC Run 1 data. This thesis presents the first measurement of neutral mesons with the PCM-PHOS reconstruction method. The method to obtain the raw meson yield will be discussed in this section. Subsequently, the main corrections applied to the raw meson yields are presented, followed by a discussion of the sources of systematic uncertainties. Finally, the fully corrected spectra are shown and compared to PCM and PHOS Run 1 measurements. The spectra are additionally compared to predictions from MC event generators as well as NLO pQCD calculations.

5.1 Signal Extraction

The signal extraction described in this section for the neutral mesons is performed for both data and MC. The purpose of performing this analysis with the MC is that it is used for correcting the measured data for detector effects, as will be described in the following.

Invariant Mass Distribution Given the branching ratios (BR) for two-photon decays of the neutral pion and of the η meson – $BR_{\pi^0} = 98.2\%$ and $BR_{\eta} = 39.41\%$ – the channels provide effective means for particle reconstruction. For the meson reconstruction, the V⁰ photon candidates are paired with photons, that are measured with the PHOS and have an opening angle greater than 5 mrad. For every possible combination of photon candidate pairs reconstructed with PCM and with PHOS that passed the selection criteria discussed in Section 4.2, the invariant mass is calculated using the following equation:

$$M_{\gamma\gamma} = \sqrt{2E_{\gamma_{\text{PHOS}}}E_{\gamma_{\text{PCM}}} (1 - \cos\theta_{\text{PHOS,PCM}})}.$$
 (5.1)

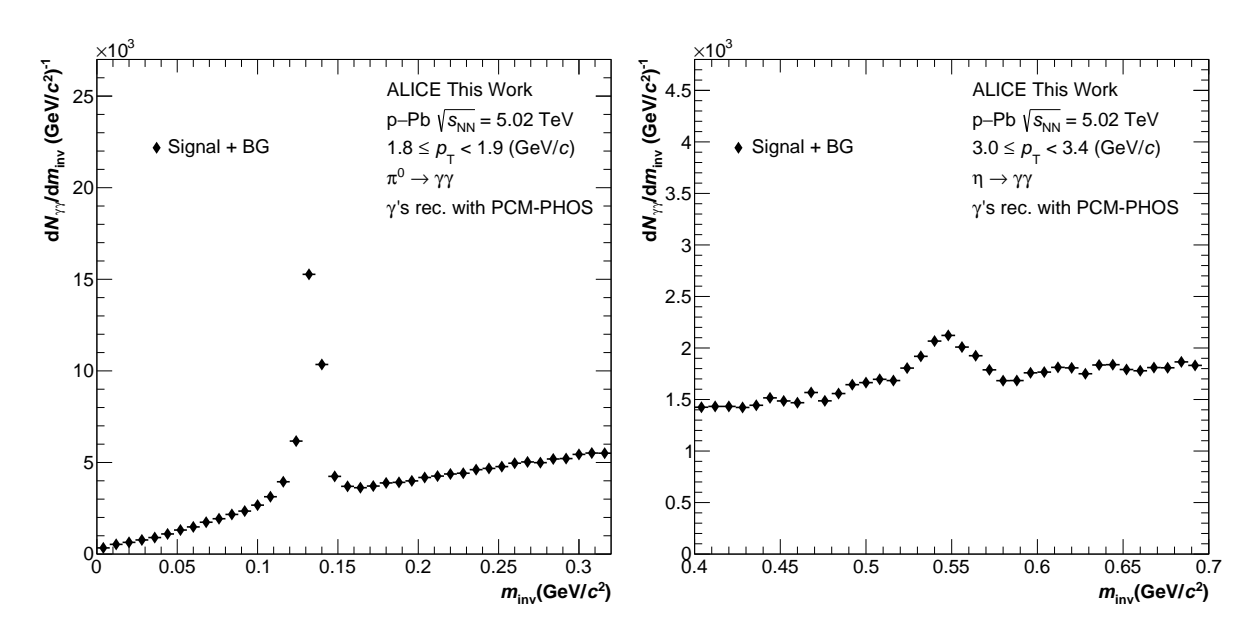


Figure 5.1: Left: Neutral pion invariant mass distribution for the transverse momentum interval $1.8 \le p_{\rm T} < 1.9 \, ({\rm GeV}/c)$. Right: η invariant mass distribution for the transverse momentum interval $3.0 \le p_{\rm T} < 3.4 \, ({\rm GeV}/c)$.

Here, $E_{\gamma_{\rm PHOS,PCM}}$ denotes the photon energy, and $\theta_{\rm PHOS,PCM}$ is the opening angle between the decay photons in the laboratory frame. Combining each photon pair and calculating the invariant mass leads to an excess yield around the nominal mass: $m_{\pi^0} = 134.976 \,\mathrm{MeV/c^2}$ for the π^0 and $m_{\eta} = 547.862 \,\mathrm{MeV/c^2}$ for the η meson [29]. The left panel of Figure 5.1 shows the invariant mass distribution with an excess near the expected neutral pion mass for the transverse momentum interval $1.8 \leq p_{\mathrm{T}} < 1.9 \,\mathrm{(GeV/c)}$, while the right panel displays the η meson distribution for the transverse momentum interval $3.0 \leq p_{\mathrm{T}} < 3.4 \,\mathrm{(GeV/c)}$. Unlike the η meson, the π^0 shows a more distinct peak above the background, which is expected given the lower production rate and branching ratio of the η meson. To extract the signal for the π^0 or η meson measurement, a background description is required.

Background Description The background shown in green in Figure 5.2 consists of both uncorrelated and correlated photon pairs. Uncorrelated photons are those that occur when decay photons originate from particles that do not share a common ancestor. Correlated photons refer to photons originating from the same particle, such as in meson decays ($\eta \to \pi^0 \pi^0 \pi^0$), or those produced within the same particle jet, sharing spatial and momentum correlations.

To model the background, two methods are commonly used: the rotation method

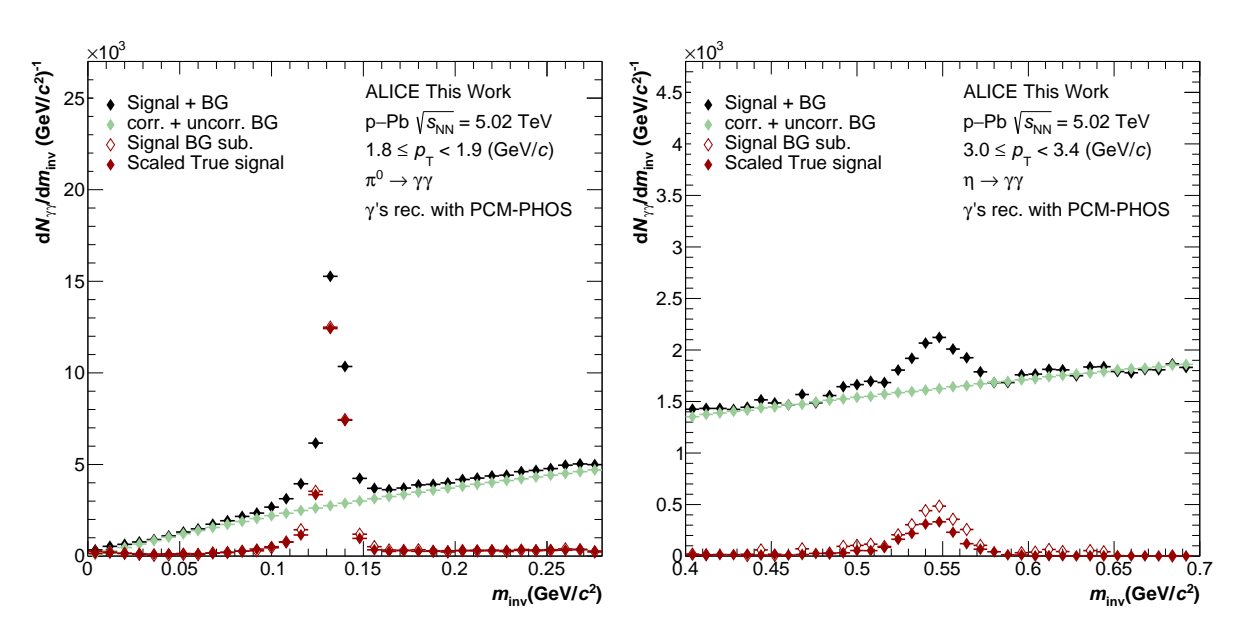


Figure 5.2: Left: Neutral pion invariant mass distribution for the example interval $1.8 \le p_{\rm T} < 1.9 \, ({\rm GeV/c}) \, Right: \, \eta$ invariant mass distribution for the example interval $3.0 \le p_{\rm T} < 3.4 \, ({\rm GeV/c})$.

and the mixed-event method. The rotation method describes the background by simulating alternative decays within the same event. After reconstructing a particle from two photons, each photon is rotated around the mother particle's momentum vector, producing a new pair while preserving first-order correlations. This method maintains the original event's correlations and therefore provides a great tool to model the correlated background. It requires, however, at least three photons per event, resulting in limited statistics. The event mixing method on the other hand combines photon candidates from different events to scale the background, offering higher statistical power. Both approaches replicate the spatial patterns found in same-event data, but also ensure that all clusters fall within the detector's acceptance range. This thesis employs the event mixing method as it is found to describe the background equally good as the rotation background, however, the event mixing offers much smaller statistical uncertainties.

The background obtained via the mixed event methods needs to be scaled to match the background in the same-event distribution. This analysis uses the following secondorder polynomial fit to scale the background:

$$f(m_{\gamma\gamma}) = B(m_{\gamma\gamma}) \cdot (p_3 \cdot m_{\gamma\gamma}^2 + p_4 \cdot m_{\gamma\gamma} + p_5) + p_1(M(m_{\gamma\gamma}) + p_2 \cdot S(m_{\gamma\gamma})). \tag{5.2}$$

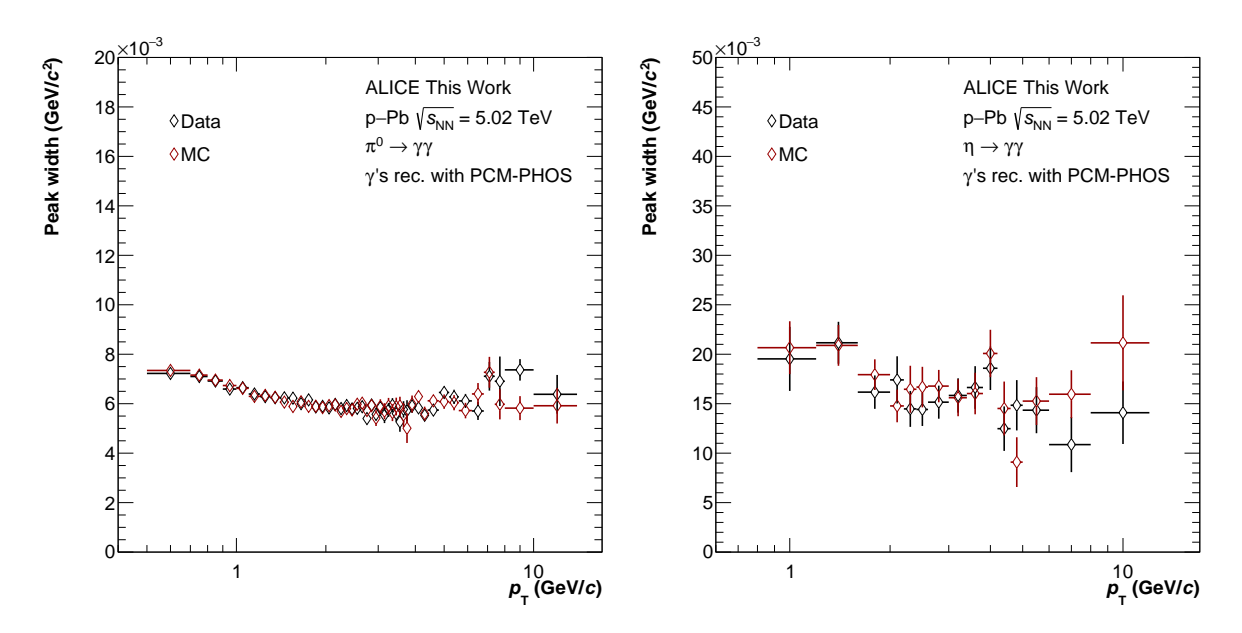


Figure 5.3: Left: FWHM of the neutral pion obtained from the respective invariant mass peak fits as a function of transverse momentum. Right: FWHM of the η obtained from the respective invariant mass peak fits as a function of transverse momentum.

Here, M represents the MC-based template for true π^0 or η mesons, S is the second meson signal template, capturing the other meson type (η or π^0). The parameter B denotes the obtained background distribution. The parameters $p_{1,2,3,4,5}$ are free fit parameters used to fine-tune the background model. After scaling the background, it is subtracted from the same-event distribution in each $p_{\rm T}$ interval.

Figure 5.2 shows two exemplary $p_{\rm T}$ intervals for the π^0 (left) and η (right) meson again with the same-event distribution shown in black markers. The background obtained via the scaling of the event mixing method is drawn in green markers. After subtracting the background, the signal, which is drawn in red markers is obtained. The scaled π^0 signal shape from the MC is drawn in open red markers. In general, a good agreement between the MC true signal and the extracted data can be seen. As the signal is now sufficiently cleared from background contribution, the signal in the peak region can be extracted.

Peak Extraction After subtracting the background from the invariant mass distribution, the remaining signal is parameterized using a Gaussian function and exponential tail on the left to account for energy loss due to Bremsstrahlung and late conversions in the detector material. This and the previous steps have been performed across multiple transverse momentum bins. In Appendix 8.2, the different $p_{\rm T}$ -intervals

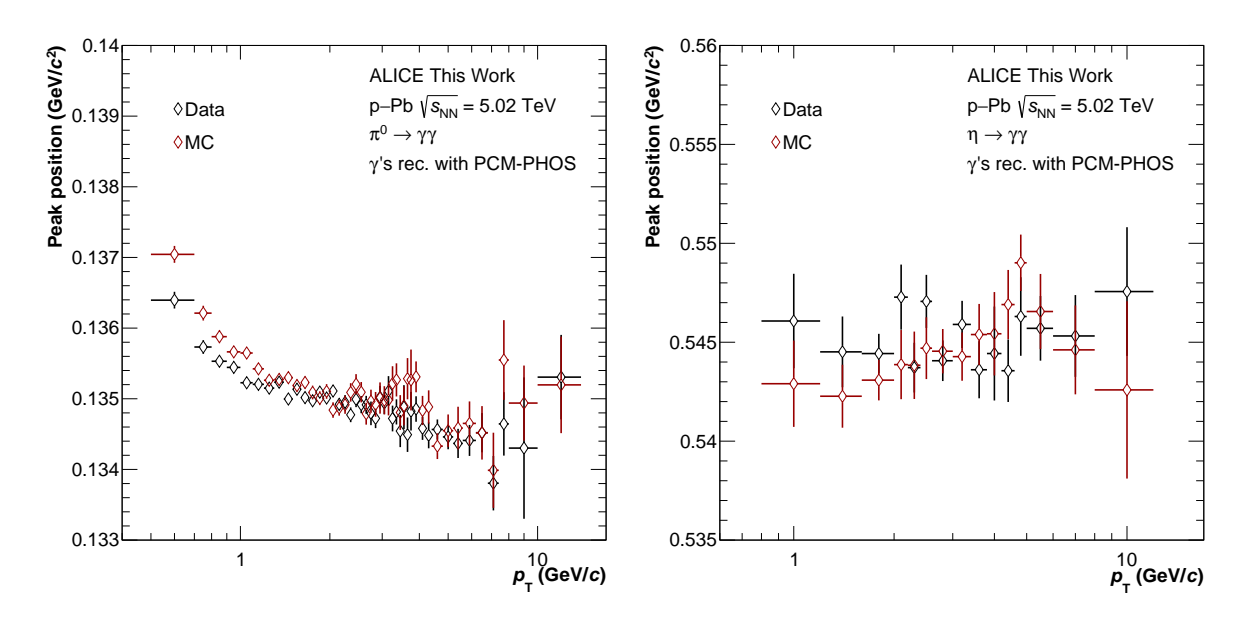


Figure 5.4: Left: Mass position of the neutral pion obtained from the respective invariant mass peak fits as a function of transverse momentum. Right: Mass position of the η obtained from the respective invariant mass peak fits as a function of transverse momentum.

are listed.

The Gaussian with the exponential tail is applied to extract the invariant mass peak position at full width at half maximum (FWHM) for both mesons across their transverse momentum bins. Figure 5.3 presents the full width at half maximum values as a function of $p_{\rm T}$ for data and MC, illustrating the agreement between data and MC. Similarly, Figure 5.4 shows the extracted peak position as a function of $p_{\rm T}$ for data and MC. The good agreement between data and MC for both variables indicates a good calibration of the detector and the energy resolution. This ensures that the MC can be used for the correction of the data.

After performing the fit, the meson yield is extracted by integrating the background subtracted mass distribution for each transverse momentum bin in a fixed window around the estimated peak position. The integration range for the π^0 meson is set to $(M_{\pi^0} - 0.035 \,\text{GeV}/c, M_{\pi^0} + 0.012 \,\text{GeV}/c)$. Given that the choice of the integration region is arbitrary, variations in the integration range are accounted for as part of the systematic uncertainties. Since the η meson has a much broader peak, the integration range is widened accordingly $(M_{\eta} - 0.048 \,\text{GeV}/c, M_{\eta} + 0.022 \,\text{GeV}/c)$.

After performing these steps, one obtains the raw neutral meson yields as a function of $p_{\rm T}$ which are depicted in Figure 5.5. The measurement for the π^0 meson ranges from

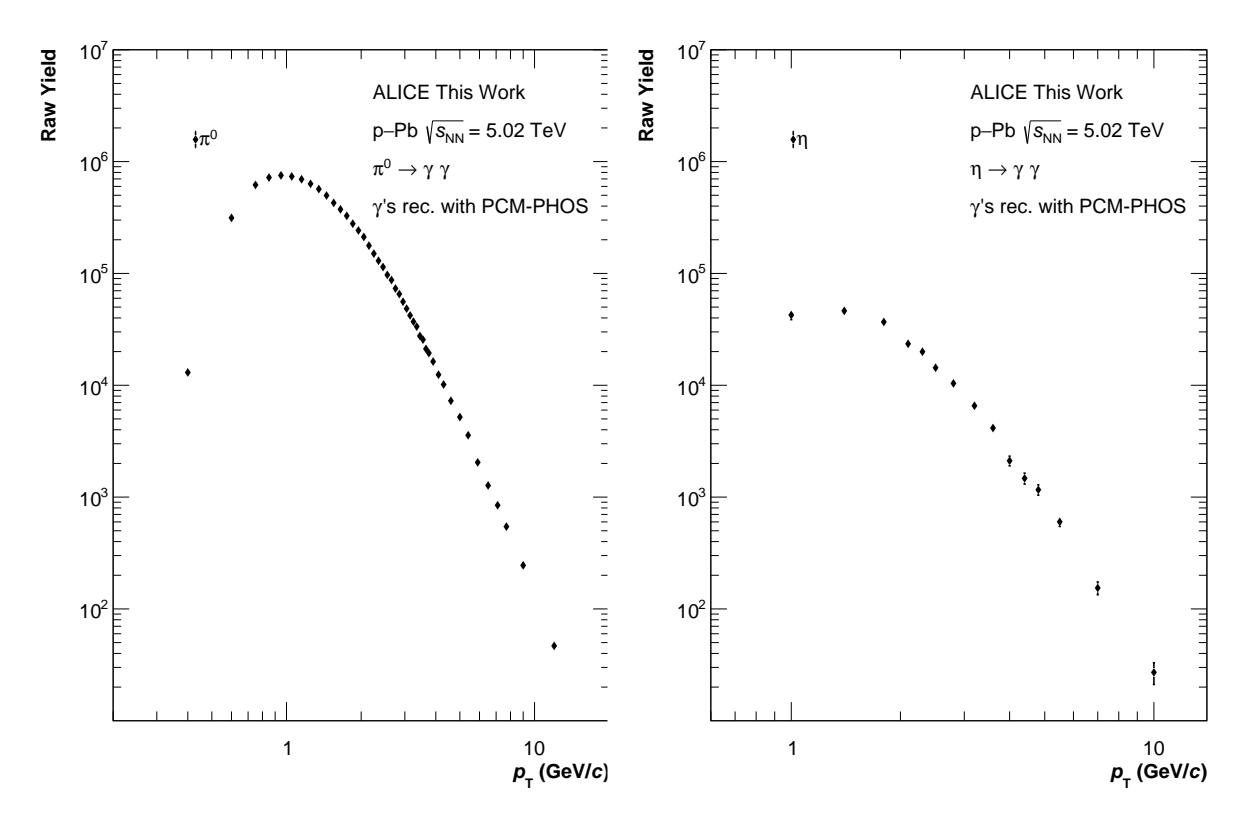


Figure 5.5: Left: Raw yield of the π^0 meson obtained after peak extraction for the different $p_{\rm T}$ intervals. Right: Raw yield of the η meson obtained after peak extraction for the different $p_{\rm T}$ intervals.

 $0.5 < p_{\rm T} < 14\,{\rm GeV/}c$ and for the η meson $0.8 < p_{\rm T} < 12\,{\rm GeV/}c$. The most important constrain at low transverse momentum is the minimum cluster energy requirement for the PHOS cluster. The η meson spectrum, on the other hand, is limited due to its lower signal, as the branching ratio is only 39.41% for the two photon decay. In combination with a smaller acceptance for η photons, the $p_{\rm T}$ range of the measurement is constrained, as will be discussed in the next section. Since the raw yield contains contamination from detector effects or other decaying particles, multiple corrections need to be applied which will be discussed in the section that follows.

5.2 Corrections

The corrections needed for the raw yield are obtained by MC simulations. These MC simulations either allow for the correction of particle contamination from other decays or detector effects. Compared to purely PCM-based measurements, the PCM-PHOS reconstruction method requires fewer corrections, as it avoids complications such as out-of-bunch pileup contamination [25].

Particle	Decay	Branching	Decay
	Channel	Ratio	Length
$K_{ m S}^0$	$\pi^0\pi^0$	30.69 %	2.68 cm
$K_{ m L}^0$	$\pi^0\pi^0\pi^0$	19.84%	15.34 m
	$\pi^+\pi^-\pi^0$	12.5%	19.94 III
Λ	$n\pi^0$	38.50%	7.89 cm

Table 5.1: Strange particles that decay into π^0 and their respective branching ratios and decay lengths.

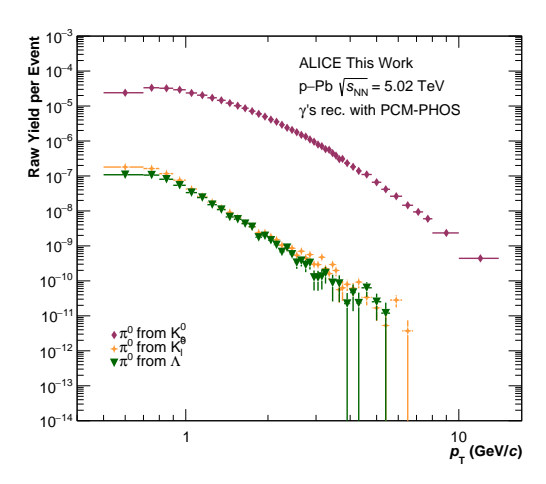


Figure 5.6: π^0 from weak decays of the $K_{\rm L}^0, K_{\rm S}^0$ and Λ particles.

5.2.1 Secondary Contamination

The raw π^0 particle spectrum includes π^0 particles produced via hadronic interactions with the detector material and π^0 produced from weak decays from $K_{\rm L}^0$, the $K_{\rm S}^0$, and Λ . These decay π^0 are commonly denoted as secondaries and have to be differentiated from the primary π^0 , which are directly produced in the collision or by decays via the strong interaction. To correct for contamination in the primary neutral meson yield, the secondary neutral pion contribution is derived from simulations based on measured particles. This approach is preferable to using purely MC simulations which depend on particle generators and whose predicted particle abundances vary with the generator used.

To estimate the contribution from secondary neutral pions, the particle decays are simulated via PYTHIA. To estimate the contribution from secondary neutral pions, the measured spectra from $K_{\rm S}$ and Λ [30] are parameterized. The parameterizations are then used as input for a decay simulation based on PYTHIA. The latter generates the particles flat in transverse momentum for a rapidity of $|\eta| < 1$ and a full azimuthal

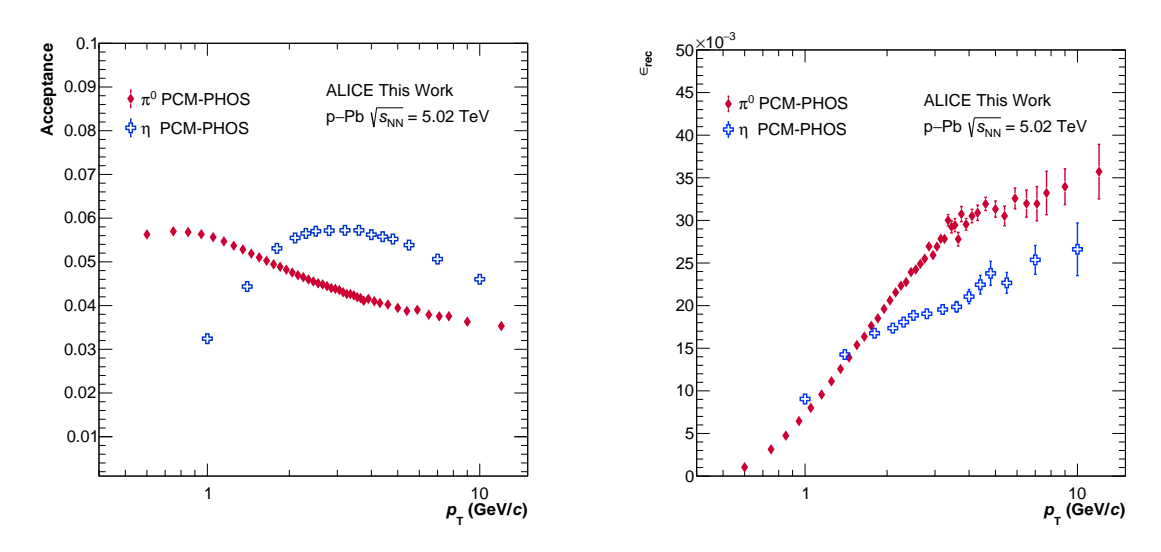


Figure 5.7: Left: Acceptance for both neutral mesons as a function of $p_{\rm T}$. Reconstruction efficiency for both neutral mesons as a function of $p_{\rm T}$.

angle of $0 < \phi < 2\pi$. The simulations include information on the branching ratio of the different particles that are summarized in Table 5.1. Then, the limited detector acceptance and efficiency, which are obtained via the MC simulations, is applied on the secondary spectra to obtain the secondary raw yield. This enables the subtraction of the secondary contamination from the raw π^0 particle spectra.

The number of π^0 from different decay sources is shown in Figure 5.6. As expected, being an order of magnitude larger than the $K_{\rm L}^0$, the $K_{\rm S}^0$ distribution is the largest contributor to the secondary contamination in this analysis. On the other hand, neutral pions stemming from the decay of Λ mesons are the smallest contributor to secondary contamination considered in this analysis, as their contribution is two orders of magnitude lower.

5.2.2 Acceptance and Efficiency

MC simulations, as briefly introduced in Section 4.1, are crucial for evaluating how detector effects alter measurements. Since each detector has a limited rapidity window for detecting particles produced in a collision, as shown in Table 4.5, not all particles produced in the collision can be observed. For example, the PHOS detector covers an acceptance range of $250^{\circ} < \phi < 320^{\circ}$ and a pseudorapidity range of $|\eta| < 0.12$, while the PCM method requires that photons and their conversion products remain within the TPC acceptance window of $0 < \phi < 2\pi$ rad and $|\eta| < 0.8$. As the opening angle of decay photons depends on their transverse momentum, smaller momenta result in

larger opening angles, potentially causing decay particles to fall outside the detector's acceptance range.

To account for these losses, a $p_{\rm T}$ -dependent acceptance correction is applied. This correction is based on MC simulations, which provide $p_{\rm T}$ -dependent particle generation data and the decay photon directions. By comparing simulations to data, the fraction of particles within the detector's acceptance range is determined. A correction factor is then calculated as the ratio of the total number of generated particles to those within the acceptance range. This correction factor, called acceptance (A), is defined as the ratio of the number of particles within the acceptance range $(N_{\rm acc})$ to the total number of particles $(N_{\rm prod})$ produced in the collisions within the inspected rapidity range, as expressed in the following equation:

$$A(p_{\rm T}) = \frac{N_{\rm acc}(p_{\rm T})}{N_{\rm prod}(p_{\rm T})}.$$
(5.3)

The left panel of Figure 5.7 shows the acceptance for both mesons for the π^0 in red, and for the η meson in blue. The π^0 acceptance initially rises slowly up to a $p_{\rm T}$ value of $p_{\rm T}=1\,{\rm GeV}/c$, then steadily declines, appearing to level off around $p_{\rm T}=4\,{\rm GeV}/c$. In contrast, the η meson has a much lower acceptance at low $p_{\rm T}$ values due to the larger opening angle of its decay photons. However, at higher $p_{\rm T}$, both acceptances begin to converge.

In addition to being constrained by detector geometry, particle measurements are affected by losses and energy smearing due to detector effects, such as malfunctioning electronics and limitations in spatial and energy resolution. To address these losses, full MC detector simulations are used. After generating all particles, the same analysis steps—such as photon reconstruction and signal extraction—are applied. The reconstruction efficiency is then defined as the fraction of the reconstructed π^0 - or η -mesons, $(N_{\rm rec})$, to the π^0 - or η -mesons, $(N_{\rm acc})$, whose decay photons point towards the PHOS detector, as given by:

$$\epsilon_{\rm rec}(p_T) = \frac{N_{\rm rec}(p_{\rm T})}{N_{\rm acc}(p_{\rm T})}.$$
 (5.4)

However, for this approach to be effective, the MC simulation must accurately describe the data, as discrepancies in cluster energy could lead to deviations in the π^0 and η meson peaks. As noted previously, Figure 5.4 shows no significant differences between the MC simulation and the data, ensuring a reliable estimation of the reconstruction

efficiency.

The reconstruction efficiency is depicted in the right panel of Figure 5.7. Both mesons show an increase with higher $p_{\rm T}$ values. This is because the probability of reconstructing clusters increases with higher cluster energies. While higher-energy clusters are more likely to be reconstructed, they also contribute to higher background, affecting overall reconstruction efficiency. This causes a plateau-like shape at higher transverse momenta.

5.3 Systematic Uncertainties

For the neutral meson measurement, the analysis uses a range of selection criteria on physical quantities, as detailed in Section 4.2.1. However, the MC simulations employed for corrections do not perfectly replicate all physical quantities where these selective criteria are applied, resulting in minor discrepancies between the data and simulations. Equally, uncertainty in selecting the photon candidates and the following applied signal extraction can lead to small variations in the corrected yield. To address this, the selection criteria applied to the data are systematically varied and the differences are compared. It is assumed that the individual contributions to the systematic uncertainty are uncorrelated. Generally, the size of each contribution is determined by repeating the analysis with one or more variations of the discussed parameters. The systematic uncertainty for each contribution is then obtained by comparing the $p_{\rm T}$ spectra under these variations (varied $p_{\rm T}$ spectra) to the $p_{\rm T}$ spectrum using the standard parameters (standard $p_{\rm T}$ spectrum). The magnitude of the systematic uncertainty is calculated as the root mean square of the maximum positive deviation Δ^+ and the maximum negative deviation Δ^- between the varied $p_{\rm T}$ spectra and the standard $p_{\rm T}$ spectrum. The total systematic uncertainty from all the different variations can be calculated using Gaussian error propagation:

$$\sigma_{\rm sys}(p_{\rm T}) = \sqrt{(\Sigma \sigma_{\rm sys,X}(p_{\rm T}))^2}.$$
 (5.5)

Systematic uncertainties calculated using this method often exhibit significant binto-bin fluctuations typically arising from statistical variations or signal extraction differences. Since the same analysis workflow is applied, the uncertainties are expected to show a correlated, $p_{\rm T}$ -dependent pattern. This analysis leverages this relationship by smoothing the uncertainties through a polynomial fit that captures the $p_{\rm T}$ -dependent trend. The following sections discuss the contributions from various cut selections, where these smoothed values are used.

Minimum Cluster Energy As previously discussed, a cluster must have an energy of $E_{\rm cluster,min} \geq 0.3\,{\rm GeV}$ to be included in the analysis. The lower a cluster's energy, the higher the likelihood that it contains a significant portion of electronic noise or energy deposition from a hadron passing through the PHOS. These clusters contribute to the background. For systematic variations, energy thresholds of $E_{\rm cluster} \geq 0.6\,{\rm GeV}$, $E_{\rm cluster} \geq 0.8\,{\rm GeV}$, and $E_{\rm cluster} \geq 0.9\,{\rm GeV}$ are chosen. For the variations with $E_{\rm cluster} \geq 0.8\,{\rm GeV}$, and $E_{\rm cluster} \geq 0.9\,{\rm GeV}$, the $p_{\rm T}$ spectrum of the π^0 can only be determined for $p_{\rm T} > 1.5\,{\rm GeV}/c$ and $p_{\rm T} > 1.7\,{\rm GeV}/c$, respectively, as the minimum cluster energy is directly related to the lowest reconstructable $p_{\rm T}$. In these ranges, the respective variation is not considered when determining the systematic uncertainty.

Minimum amount of cells In this analysis, the minimum number of cells per cluster is set to two but varied to three cells per cluster. This variation particularly impacts the $p_{\rm T}$ spectra at low transverse momentum since clusters are generally smaller at low $p_{\rm T}$ than at high $p_{\rm T}$. Due to limitations in the MC simulations, which do not accurately represent clusters with low energies, this variation leads to large deviations that likely overestimate the systematic uncertainty [27]. The primary cause of these large deviations is noise suppression applied to the PHOS cell signals, causing simulations to align less accurately with measurements. This variation is thus disregarded for values below $p_{\rm T} \approx 3\,{\rm GeV/c}$, as it would otherwise lead to an overestimation of systematic uncertainty [27]. In this analysis, therefore, the systematic uncertainty for $p_{\rm T} < 3\,{\rm GeV/c}$ is assumed to be constant.

Cluster form In the present analysis, the cluster shape parameter M_{02} is restricted to the range $0.1 \le M_{02} < 0.7$. The range of M_{02} values is extended to $0.1 \le M_{02} < 1.3$ and $0.1 \le M_{02} < 2.5$, and the impact of removing the M_{02} restriction is included in the study of systematic uncertainties.

Cluster Timing The cluster time indicates the specific time in which photons deposit their energy in the calorimeter cells. The data used for this analysis has a bunch crossing of 100 ns. Therefore, the timing of cluster recording is restricted in the analysis to $-50 \le t_{\text{cluster}} < 50 \,\text{ns}$. This choice allows nearly all clusters originating from particles produced in the collision to be included in the analysis. To

determine the systematic uncertainty, two variations are considered. The first variation, $-30 \le t_{\rm cluster} < 35 \,\mathrm{ns}$ and $-20 \le t_{\rm cluster} < 20 \,\mathrm{ns}$ are chosen which exclude more clusters from other bunch crossings.

Inner and outer material budget The material budget uncertainty for the PCM method is estimated at 2.5%, primarily due to the inner detector material, which directly correlates with the conversion probability [31]. For the PHOS detector, the material budget is similarly independent of transverse momentum, with an estimated uncertainty of 2% [32]. Unlike the PCM technique, the PHOS uncertainty arises from the outer detector material, including the outer TPC wall, TOF, and their support structures. Since the uncertainty applies to each conversion photon, the total systematic uncertainty is 4.5%. Extensive prior analyses have aimed to evaluate and reduce the material budget uncertainties for reconstruction methods; hence, no additional variations are performed in this analysis to reassess the systematic error from the material budget [31].

Track matching To optimize the matching between tracks and clusters, an initial matching window of $\Delta\eta=0.005$ and $\Delta\varphi=0.03$ is chosen as the baseline. Two variations are then tested to determine their effect on cluster exclusion. In the first variation, a fixed, larger matching window of $\Delta\eta=0.01$ and $\Delta\varphi=0.07$ is applied, which excludes more clusters from the analysis, potentially reducing noise at the cost of losing some signal clusters. The second variation introduces a $p_{\rm T}$ -dependent matching window to account for the relationship between track resolution and transverse momentum: $\Delta\eta$ is defined as $0.025 + \left(\frac{1}{p_T + 3.52}\right)^3$ and $\Delta\varphi$ as $0.025 + \left(\frac{1}{p_T + 3.62}\right)^2$. This dynamic adjustment allows for a larger matching window at low $p_{\rm T}$, where track resolution is lower, while tightening the matching window for high- $p_{\rm T}$ tracks where precision improves. In theory, the $p_{\rm T}$ -dependent approach should increase matching accuracy across a wider range of $p_{\rm T}$ values by balancing efficiency and noise suppression dynamically. The results from these variations can reveal whether a fixed or adaptive matching window is more effective for optimal cluster selection.

Electron and pion identification This category includes all uncertainties associated with electron identification and contamination rejection in photon conversions, specifically at the level of individual electron tracks (legs). These uncertainties are estimated by varying the electron inclusion criteria and pion rejection thresholds

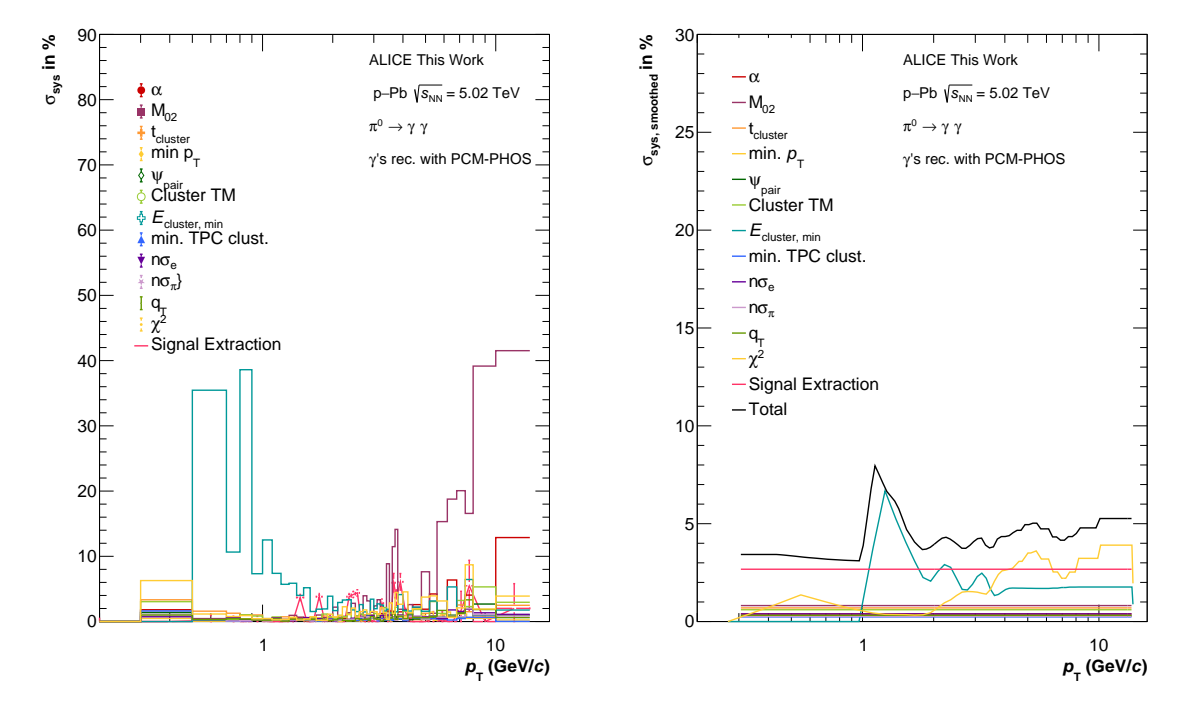


Figure 5.8: Left: Systematic uncertainty as a function of $p_{\rm T}$ for the π^0 , based on the applied variations, where the $p_{\rm T}$ -dependent fluctuations have not yet been smoothed. Right: Systematic uncertainty as a function of $p_{\rm T}$ for the π^0 after smoothing.

based on TPC dE/dx measurements. For the electron identification, the ranges of the $n\sigma$ values are varied between $-4 < n\sigma_e < 5$ and $-2 < n\sigma_e < 4$. This allowed to study loose restriction on the electron rejection based on the specific energy loss. For the pion rejection, the $n\sigma$ is varied between $-2 < n\sigma_{\pi} < 10$ and $0 < n\sigma_{\pi} < 10$.

Photon Identification Another dominant uncertainty for the PCM reconstruction is the various photon selection criteria. Predominantly, the background rejection criteria on the basis of the χ^2 and $\psi_{\rm pair}$ selection criteria as well as the momentum dependent cuts on the basis of the Armenteros-Podolanski plane are varied to assess their effect on the photon identification. The $\psi_{\rm pair}$ selection is varied between 0.15-0.3 and the χ^2 ranged from -0.005-0.065. This increases the combinatorial background since the signal of χ^2 and $\psi_{\rm pair}$ should be close to 0.

Secondaries track reconstruction The track quality selection necessary for the reconstruction for the V⁰ candidates is associated with multiple systematic uncertainties. First, the minimum transverse momentum of tracks is augmented to $p_{\rm T}=0.11\,{\rm GeV}/c$, $p_{\rm T}=0.14\,{\rm GeV}/c$ and $p_{\rm T}=0.16\,{\rm GeV}/c$. Additionally, the minimum ratio of the num-

Variation	$\pi^0 \; (\mathrm{GeV}/c^2)$	$\eta \left(\mathrm{GeV}/c^2 \right)$
Standard	$(M_{\pi^0} - 0.035, M_{\pi^0} + 0.012)$	$(M_{\eta} - 0.048, M_{\eta} + 0.022)$
Narrow	$(M_{\pi^0} - 0.015, M_{\pi^0} + 0.005)$	$(M_{\eta} - 0.036, M_{\eta} + 0.010)$
Wide	$(M_{\pi^0} - 0.055, M_{\pi^0} + 0.025)$	$(M_{\eta} - 0.068, M_{\eta} + 0.025)$

Table 5.2: Variations of the integration windows for the systematic error estimation from the signal extraction.

ber of TPC clusters to the number of findable clusters are varied to 35 % and 70 %.

Signal extraction For the invariant mass analyses, an uncertainty in yield extraction is estimated by considering variations in the integration windows around the fitted mass position and the different ways to describe the background. Additionally, the dependence of signal extraction on the signal-to-background ratio is tested by adjusting the minimum opening angle and introducing a mild asymmetry between the decay photons. Table 5.2 summarizes the different integration ranges used for the estimation of this uncertainty.

The systematic uncertainties for each $p_{\rm T}$ interval as well as the smoothed systematic uncertainties for the π^0 are shown in Figure 5.8. The uncertainties for the η are presented in Figure 5.9. Since the inner and outer material budgets are considered as constant, they are not included in the Figure. The smoothed systematic uncertainties are then used to determine the corrected yields of the different mesons, which will be discussed in the following section.

5.4 Results

5.4.1 Minimum Bias

In this section, the fully corrected $p_{\rm T}$ -differential Lorentz-invariant yields of the π^0 and η mesons are presented. To obtain the fully corrected $p_{\rm T}$ -dependent yield the previously discussed corrections are applied to the measured raw yield of the mesons. The $p_{\rm T}$ -differential invariant meson yield can thus be expressed as:

$$\frac{1}{N_{\text{ev.}}} \frac{dN_{\text{corr}}^{\text{Meson}}}{dp_{\text{T}}dy} = \frac{1}{BR} \frac{1}{\epsilon_{\text{rec}} \cdot A} \frac{1}{N_{\text{ev.}}} \frac{(1 - r_{\text{sec}}) \cdot N^{\text{Meson}}}{2\pi p_{\text{T}} \Delta p_{\text{T}} \Delta y}.$$
 (5.6)

The components of the given expression are:

• $p_{\rm T}$ mean transverse momentum of the given $p_{\rm T}$ interval

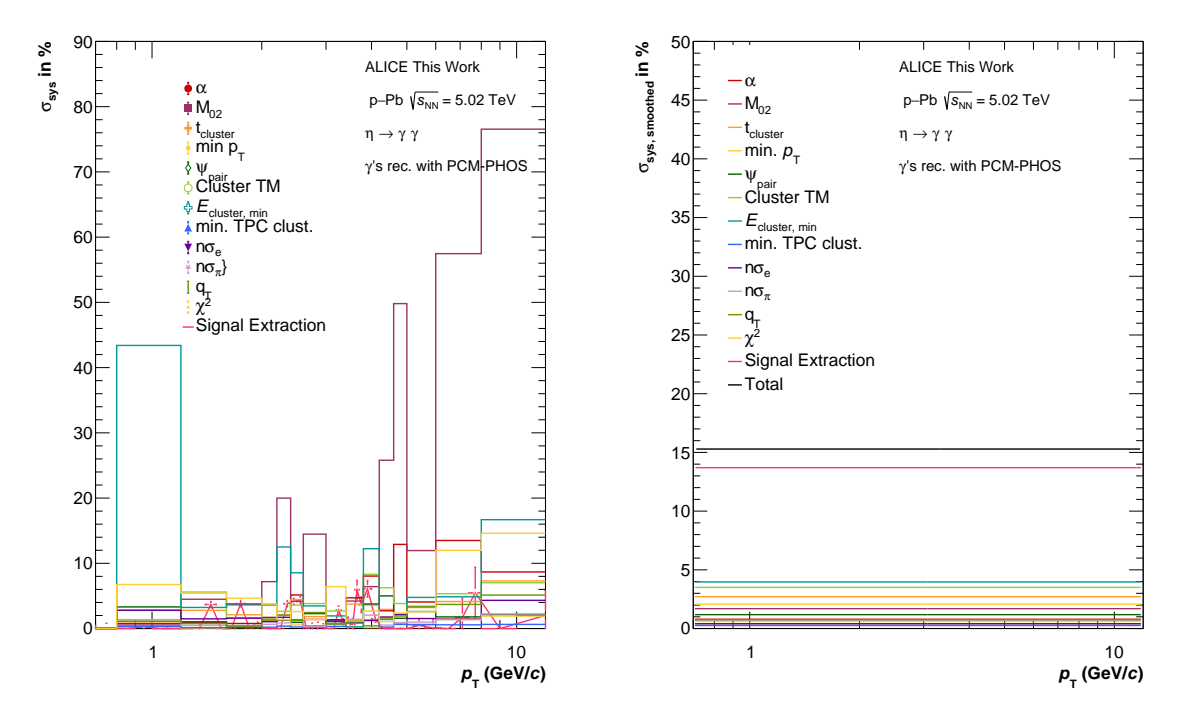


Figure 5.9: Left: Systematic uncertainty as a function of $p_{\rm T}$ for the η , based on the applied variations, where the $p_{\rm T}$ -dependent fluctuations have not yet been smoothed. Right: Systematic uncertainty as a function of $p_{\rm T}$ for the η after smoothing.

- $N_{\text{ev.}}$ number of events (Table 4.1)
- BR branching ratio of $\pi^0 \to \gamma \gamma$ and $\eta \to \gamma \gamma$
- $\epsilon_{\rm rec}$ reconstruction efficiency
- \bullet A detector acceptance
- $r_{\rm sec}$ fraction of secondary neutral mesons.
- $\frac{N^{\text{Meson}}}{\Delta p_{\text{T}} \Delta y}$ number of reconstructed mesons in a p_{T} interval and rapidity range.

The corrected pion yield as a function of $p_{\rm T}$ is shown in Figure 5.10 in black for a $p_{\rm T}$ range of $0.5 \leq p_{\rm T} < 14\,{\rm GeV}/c$. The statistical uncertainties are drawn as vertical lines and the systematic uncertainties are drawn as boxes. Additionally, the predicted particle productions from three different MC generators are shown: EPOS LHC in blue, DPMJet in violet, and HIJING in orange. Comparing the measured yield to these MC predictions enables testing of the various theoretical models embedded in each generator, which will be discussed later in the section.

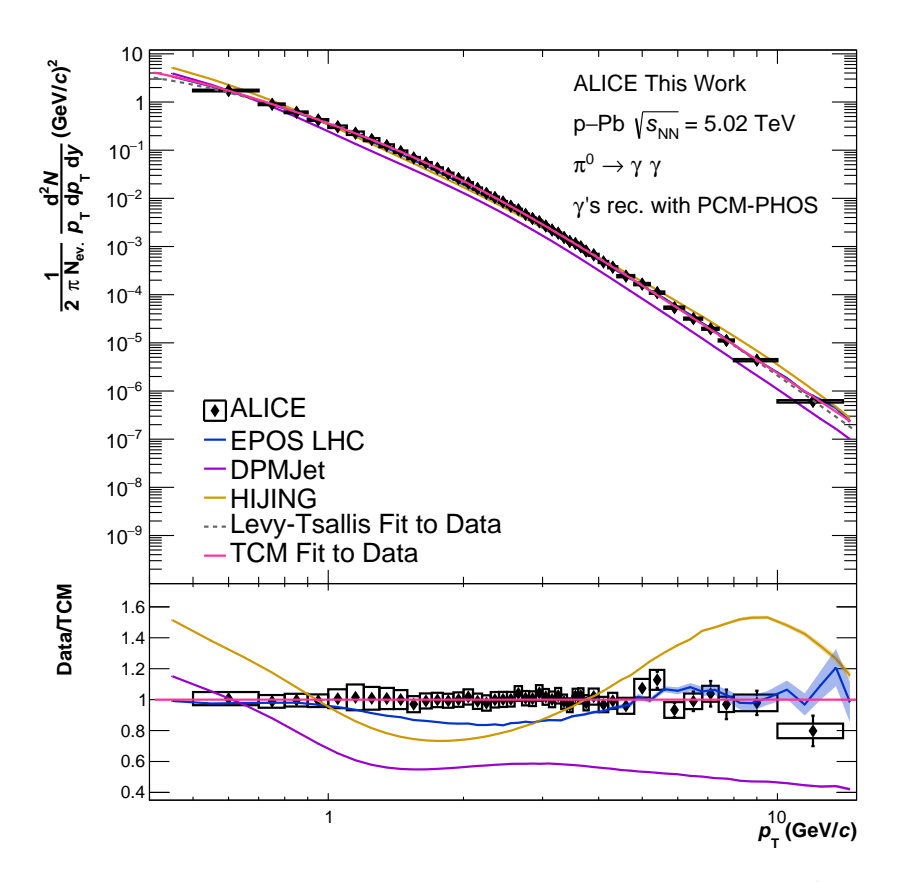


Figure 5.10: Upper Panel: Fully corrected $p_{\rm T}$ -dependent invariant π^0 yield in p–Pb collisions at $\sqrt{s_{\rm NN}}=5.02\,{\rm TeV}$ reconstructed with PCM-PHOS. Additionally, comparisons to MC predictions and a parameterizations with a Levy-Tsallis and TCM function are included. Lower Panel: Ratios of the $p_{\rm T}$ -spectra of the π^0 from the measurement and from predictions of EPOS LHC, HIJING and DPMJet to the TCM parameterization for the respective π^0 $p_{\rm T}$ spectrum.

To facilitate later comparison to previous measurements, the data points are parameterized with different functions. One functional form used in this thesis is the Two Component Model (TCM), which was introduced by Bylinkin and Rostovsev [33]. The parameterization describes the soft part of the spectrum with an exponential and the hard part of the spectrum with a power-law as described in the following expression:

$$f_{\text{TCM}}(p_{\text{T}}) = A_{\text{e}} \exp\left(\frac{-E_{\text{T,kin}}}{T_e}\right) + A\left(1 + \frac{p_{\text{T}}^2}{nT^2}\right)^n, \tag{5.7}$$

where $E_{\rm T,kin}$ is the the transverse kinetic energy $E_{\rm T,kin} = \sqrt{p_{\rm T}^2 + m^2} - M$ with m being the meson mass. A_e , A are normalization factors and T, $T_{\rm e}$ and n are adjustable parameters. The second parameterization used to describe the yield is the Levy-Tsallis

Two Component Model Fit							
Meson	$A_e \; (\mathrm{GeV}^{-2} c^3)$	$T_e \; (\mathrm{GeV}/c)$	$A (GeV^{-2}c^3)$	T (GeV/c)	\overline{n}		
π^0	26.78 ± 8.76	0.12 ± 0.01	2.93 ± 0.01	0.54 ± 0.02	3.58 ± 0.23		
η	0.25 ± 1.2	0.23 ± 0.02	0.04 ± 0.01	0.93 ± 1.2	3.89 ± 1.2		
Levy-Tsallis Fit							
Meson	A	$T_{\rm t}~({ m MeV})$	n				
π^0	7.9 ± 1.2	0.03 ± 0.001	2.92 ± 0.2				
η	8.36 ± 1.3	0.013 ± 0.002	4.96 ± 0.1				

Table 5.3: Parameters of a TCM and Levy-Tsallis parameterization to the corrected π^0 and η spectrum.

parameterization (f_{Tsallis}), which is given by:

$$f_{\text{Tsallis}}(p_{\text{T}}) = \frac{A}{2\pi} \frac{(n-1)(n-2)}{nT_t(nT_t + M(n-2))} \left(1 + \frac{m_{\text{T}} - M}{nT_t}\right)^{-n}.$$
 (5.8)

Again A, n and T_t are adjustable parameters and $m_{\rm T}$ and M being the transverse mass and the respective meson mass. The Levy-Tsallis is generally regarded as a generalization of the Boltzmann-Gibbs distribution and has been reported to be successful in describing particle spectra [25]. All parameters used for the parameterization of the yield are listed in Table 5.3. Both parameterization are shown in Figure 5.10, where the TCM parameterization is drawn in pink and the Levy-Tsallis parameterization in gray. As seen in Figure 5.10 the Levy-Tsallis function does not describe the spectrum over the full $p_{\rm T}$ range, which is why this thesis uses the TCM for all further comparisons.

The lower panel of Figure 5.10 displays the ratios of the data and MC generators to the TCM parameterization. The comparison shows that only EPOS LHC is in agreement with the measured π^0 spectrum with a maximum deviation of 10%. The HIJING model in contrast overestimates particle production by about 60% at both low- $p_{\rm T}$ and in the high- $p_{\rm T}$ region, suggesting that adjustments are needed in the crossover region in the model itself [25]. Similarly, DPMJet predictions show a strong overestimation at low- $p_{\rm T}$ but underestimate particle production above $p_{\rm T} > 0.8\,{\rm GeV}/c$, with deviations reaching about 40% at high- $p_{\rm T}$.

Similar to the π^0 spectrum, Figure 5.11 shows the fully corrected η meson measurement in a $p_{\rm T}$ range $0.8 < p_{\rm T} < 12\,{\rm GeV}/c$ with prediction from different MC generators. Again both parameterizations introduced earlier are used to describe the data points. In contrast to the pion case, the Levy-Tsallis parameterization works equally well to

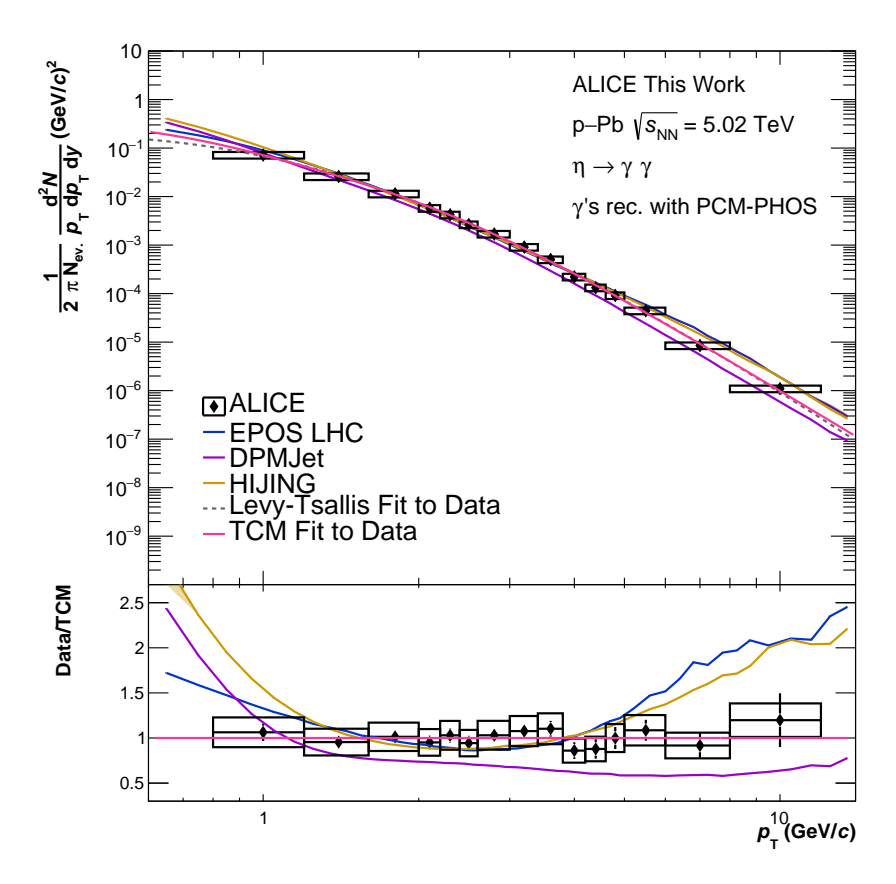


Figure 5.11: Upper Panel: Fully corrected $p_{\rm T}$ -dependent invariant η yield in p-Pb collisions at $\sqrt{s_{\rm NN}}=5.02\,{\rm TeV}$ reconstructed with PCM-PHOS. Additionally, comparison to MC predictions and a parameterization with a Levy-Tsallis and TCM function is included. Lower Panel: Ratios of the $p_{\rm T}$ -spectra of the η from the measurement and from predictions of EPOS LHC, HIJING and DPMJet to the TCM parameterization for the respective η $p_{\rm T}$ spectrum.

describe the shape of the particle yield. For consistency, this analysis uses the TCM parameterization for all further comparisons.

The comparison of the η spectrum parameterization with MC generators reveals more discrepancies than for the π^0 case, as no generator fully captures the spectrum's shape. DPMJet significantly overestimates particle production at low- $p_{\rm T}$ by about 40 %, then consistently underestimates it at higher $p_{\rm T}$ values. In contrast, both EPOS LHC and HIJING overestimate the particle production by over 40 % at low- $p_{\rm T}$. Both estimators show better agreement with the parameterization in the mid- $p_{\rm T}$ region. In the high- $p_{\rm T}$ area both estimators overestimate the particle production by over 50 %.

The reported discrepancies among various particle generators offer valuable insights for their improvement, as the deviations between data and MC generators highlight where certain model assumptions fail to accurately describe the data. To better

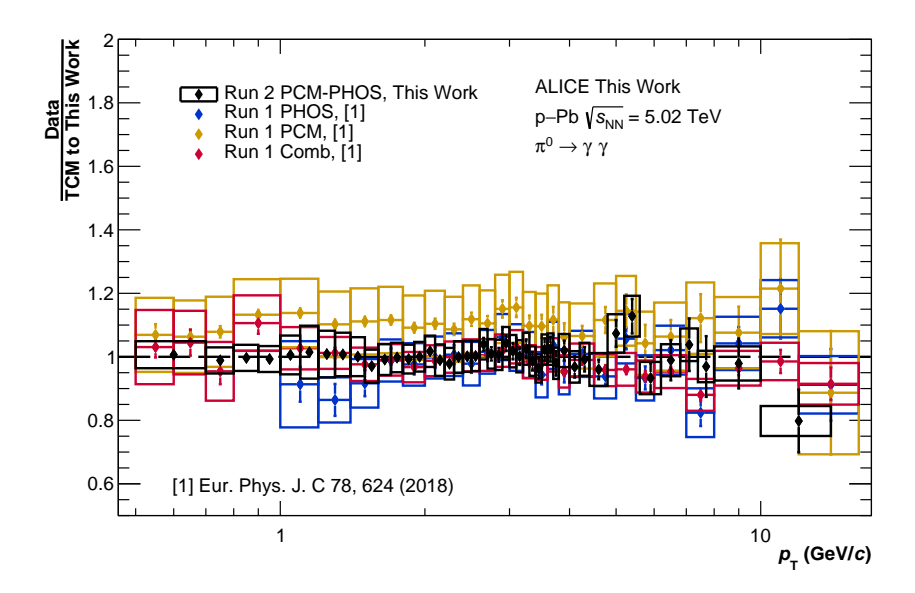


Figure 5.12: Ratio of the $p_{\rm T}$ dependent π^0 spectrum of this work as well as of published LHC Run 1 [28] measurements obtained with different photon reconstruction methods to the TCM parameterization of the data obtained in this analysis.

contextualize the performed measurement, the next section compares it with the previously published results from Run 1.

Comparison to LHC Run 1 Previous neutral meson measurements were conducted using data recorded in 2013, employing various photon reconstruction techniques. This subsection therefore aims to compare these measurements to the Run 1 measurements and provide a detailed description of the differences observed.

The data analyzed from Run 1 constitutes only 10% of the statistics of that from Run 2, which limited the ability to reconstruct mesons using the PCM-PHOS method with Run 1 data. Consequently, the measurement cannot be compared to an equivalent neutral pion measurement from Run 1. Instead, the comparison utilizes results from the Run 1 PCM and Run 1 PHOS methods. Additionally, the results from this thesis are compared to a measurement, where different reconstruction methods are combined. Due to limited statistics, the combined η spectrum did not incorporate measurements with the PHOS detector. Hence, the comparison with Run 1 only includes the measurement performed with PCM and the combined η spectrum.

Due to differing $p_{\rm T}$ interval widths, both the neutral pion measurement from this analysis and the Run 1 measurements are parameterized using a TCM parameterization, as previously described. The Run 1 measurements are then compared to the

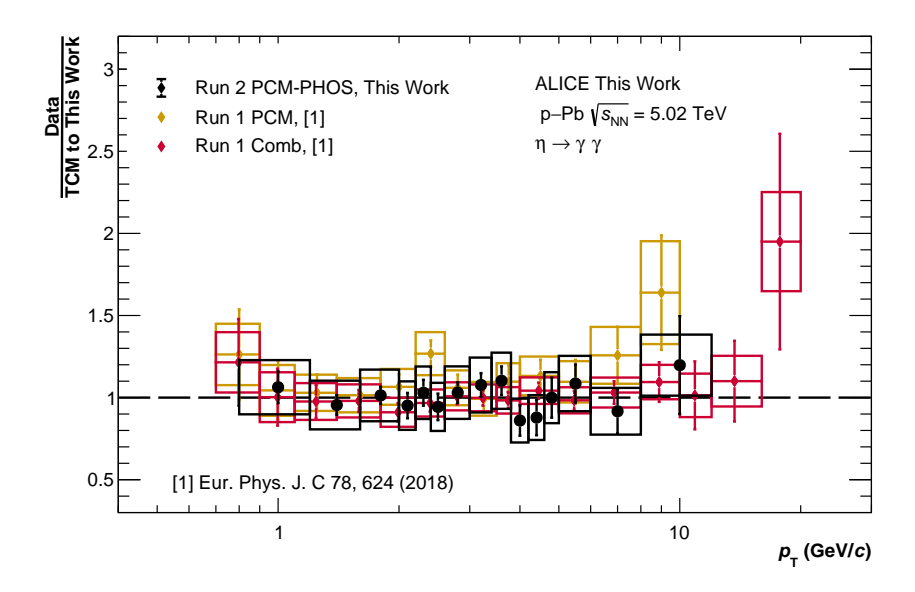


Figure 5.13: Ratio of the $p_{\rm T}$ dependent η spectrum of this work as well as of published LHC Run 1 [28] measurements obtained with different photon reconstruction methods to the TCM parameterization of the data obtained in this analysis.

presented measurement by taking the ratio to the parameterized spectra.

Figure 5.12 shows the ratio of the Run 1 measurement to the parameterized π^0 spectrum from this analysis. The ratio of the data points to the parametrization is shown in black, the Run 1 PCM measurement in yellow, the Run 1 PHOS measurement in blue, and the Run 1 combined measurement in red. Throughout the whole $p_{\rm T}$ -range, this analysis shows good agreement with both the Run 1 combined and PHOS measurement within the given uncertainty. However, the Run 1 PCM measurement differs across the entire transverse momentum range, with pronounced tension in the low- $p_{\rm T}$ region. This discrepancy can be attributed to updated material budget weights in this analysis, which shifts the Run 1 PCM measurement down by about $\approx 8\%$ [31]. Overall, reductions in both statistical and systematic uncertainties are observed for the individual reconstruction methods for the π^0 measurement.

The same approach as for the π^0 is taken for the comparison of the measured η spectrum. The measured η spectrum is compared to the Run 1 PCM and the Run 1 combined measurement. Figure 5.13 shows the ratio of the data points to the parametrization is shown in black, the Run 1 PCM measurement in yellow and the ratio of the combined measurement to the parametrization in red. Within the uncertainties the presented measurement agrees throughout the whole $p_{\rm T}$ range. The measured spectra

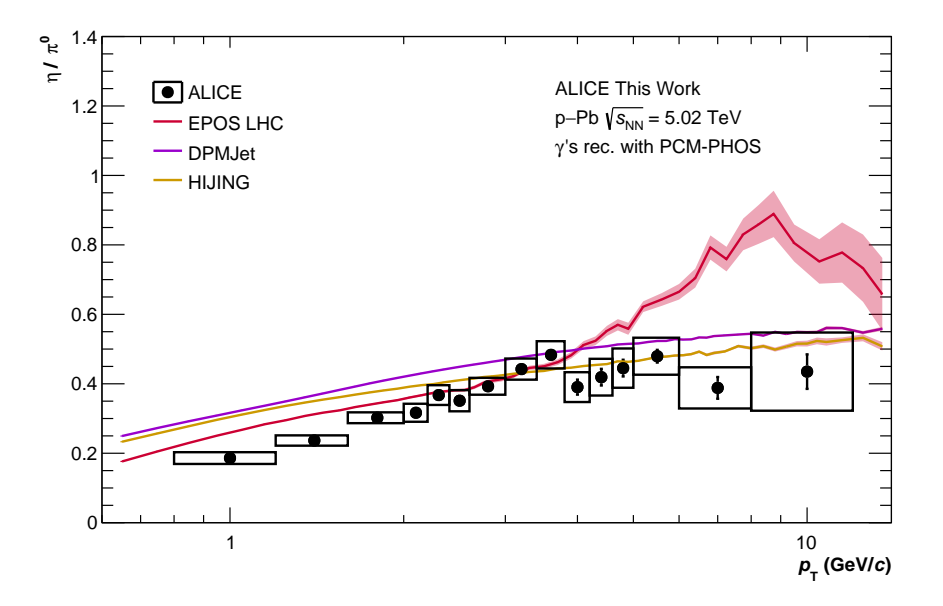


Figure 5.14: Minimum bias η/π^0 ratio with different MC generator predictions.

can now be used to investigate multiple physics observable, providing insight into the production processes of various particles.

 η/π^0 ratio In particle physics, the relative abundance of one particle compared to another is an important metric, as it provides insight into the applicability of analysis methods like the transverse mass scaling. Additionally, ratios provide an important input for fragmentation functions as it often allows multiple uncertainties to cancel; this results in a more precise estimate for the relative particle production. In this analysis, the measured π^0 and η mesons allow for a comparison of their ratio.

To obtain the η/π^0 ratio, the π^0 analysis is conducted following the same procedure as described previously, but using the same $p_{\rm T}$ intervals as for the η meson, enabling a straightforward calculation of the particle ratio. Since both measurements are equally influenced by the MC energy calibration and material budget, these contributions cancel out when calculating the systematic uncertainty for the ratio.

Figure 5.14 shows the measured η/π^0 yield: the black points represent the experimental data, while the colored lines correspond to values predicted by different MC generators. Again the EPOS prediction is drawn in red, the DPMJet prediction in violet and the HIJING values in yellow. The kinks, apparent in the EPOS line are a consequence of the fact that the underlying data is binned and connected with a line. The ratio of η/π^0 rises until $p_{\rm T} \approx 3\,{\rm GeV}/c$, beyond which it plateaus, indicating the expected asymptotic behavior within the measurement's uncertainties, as noted in prior studies [25]. In

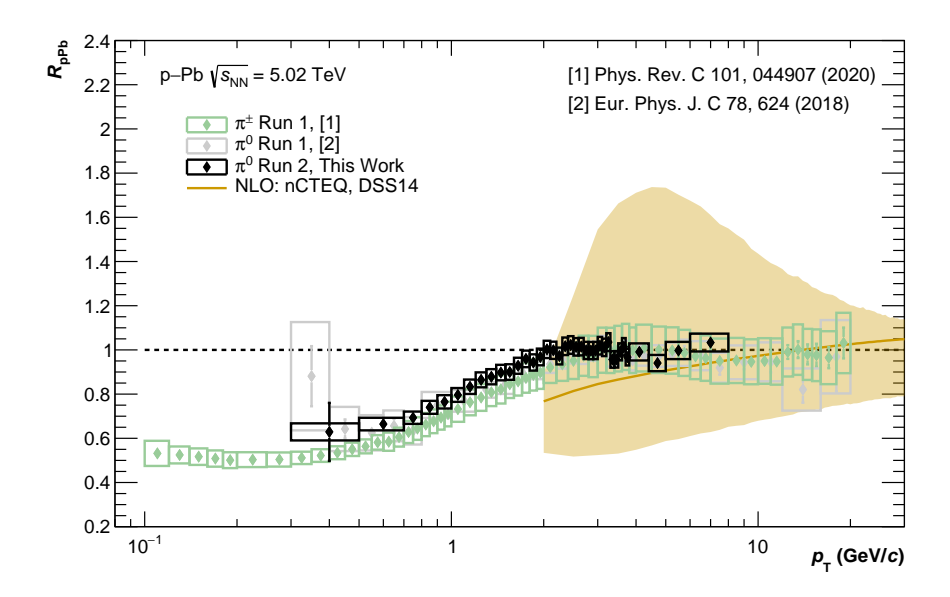


Figure 5.15: Nuclear modification factor for the π^0 meson with π^{\pm} measurement as pp reference. Additionally, the measurement of the $R_{\rm pPb,\pi^{\pm}}$ and the $R_{\rm pPb,\pi^0}$ with Run 1 data is shown.

comparison, none of the MC generators accurately capture the shape of the data, and all predict an initial value higher than observed. In the high- $p_{\rm T}$ plateau, the values from DPMJet and HIJING come closer to the experimental saturation level, while EPOS LHC does not replicate either the increase or the plateau behavior.

This section examined the particle abundances obtained in the presented analysis within the same collision system. To further investigate particle production and potential modifications, the next section compares the $p_{\rm T}$ measurements of π^0 mesons in p-Pb collisions to those in pp collisions.

 $R_{\rm pPb}$ Measurement An approach to observing modifications in particle production in the p–Pb collision system – compared to pp collisions – is through the measurement of the nuclear modification factor, as discussed in Section 2.4.2. In this analysis the nuclear modification factor for the π^0 is measured. Hereby, as will be discussed in the following, the charged pion spectrum at $\sqrt{s_{\rm NN}} = 5.02 \, {\rm TeV}$ serves as the reference for π^0 meson in pp collisions [34].

To determine the nuclear modification factor, the fully corrected spectra are divided by $\langle N_{\rm coll} \rangle$ and the relevant reference spectrum [34]. Since there is no reference measurement of π^0 at the same center-of-mass energy, the charged pion spectrum for the same center-of-mass energy is used. This charged pion spectrum is parameterized

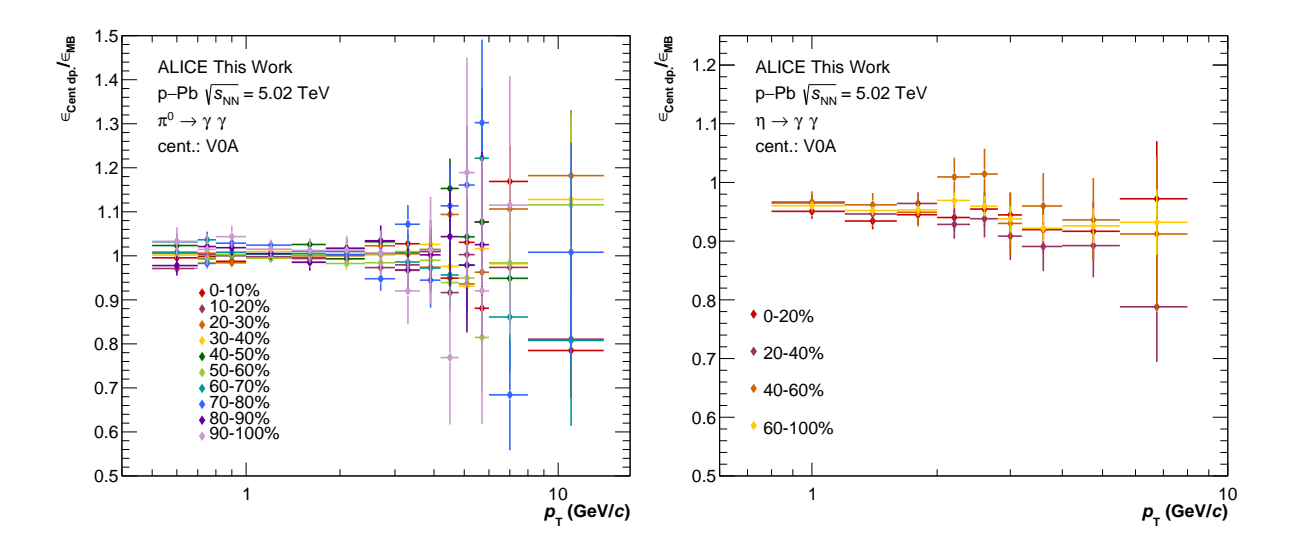


Figure 5.16: Ratio of reconstruction efficiencies in different centrality intervals to the centrality integrated efficiency for the π^0 (*Left*) and the η meson (*Right*)

using the TCM parameterization and then divided by two, to account for the fact that the charged over neutral pion ratio is expected to be two. Figure 5.15 shows the transverse momentum–dependent measurement of the modification factor for the π^0 meson obtained in this analysis. The uncertainties presented, both statistical and systematic, contain the uncertainties for contributions from this analysis and from the reference measurements. Additionally, for comparison, previous measurements of the $R_{\rm pPb,\pi^0}$ with LHC Run 1 data, the $R_{\rm pPb,\pi^\pm}$, and a theoretical $R_{\rm pPb,\pi^0}$ prediction obtained from an NLO pQCD calculation are shown.

The measurement of the $R_{\rm pPb,\pi^0}$ is shown in Figure 5.15. For $p_{\rm T}>2\,{\rm GeV}/c$, the nuclear modification factor aligns with unity and agrees with the given pQCD NLO prediction. For $p_{\rm T}<2\,{\rm GeV}/c$, however, the values fall below unity—a trend attributed to cold nuclear matter effects in the p–Pb collision system, as discussed in Section 2.4.2. Both trends are consistent with previous measurements of nuclear modification factors for neutral mesons and charged pions within their uncertainties.

5.4.2 Centrality Dependence

In addition to providing a minimum-bias measurement, this analysis presents a centrality-dependent measurement of the neutral-meson spectra. This centrality-dependent measurement enables the investigation of QGP formation constraints as peripheral Pb-Pb collisions are considered comparable to central p-Pb collisions regarding their multiplicity [1]. To estimate the centrality of an event in ALICE, three

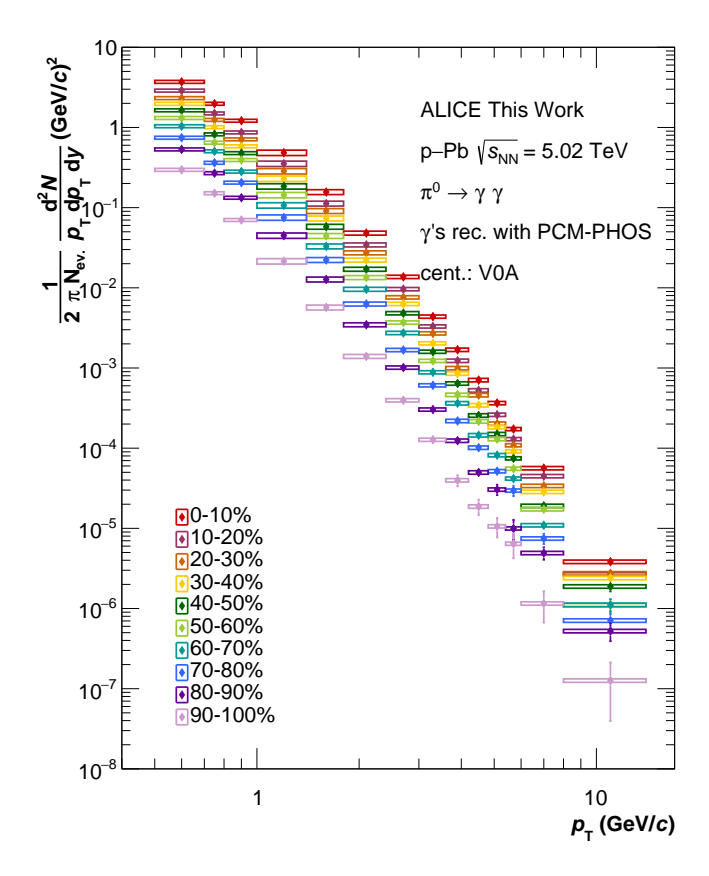


Figure 5.17: Centrality-dependent neutral pion $p_{\rm T}$ -spectra, selected with the V0A estimator.

different methods are used:

- CL1 The CL1 centrality estimator counts tracklets in the central pseudorapidity region using the ITS. Since the number of tracklets is considered to be directly correlated to the centrality. Thus a more central collision produces more tracks.
- V0A The V0A detector, as introduced, is positioned at forward rapidity of the ALICE detector. The signal intensity of the V0A is directly correlated with the event centrality in a similar way to the CL1 centrality estimator.
- ZNA The Zero Degree Calorimeter is located at the forward side of the ALICE detector and detects neutrons which are emitted close to zero degrees relative to the beam direction. These neutrons are usually produced from fragments of the nucleus which have not interacted in the collision. For this reason, one expects less signal in more central collisions and a higher signal for peripheral collisions.

Previous studies have indicated that the choice of centrality estimator can lead to observable deviations in the obtained particle spectra [35]. To assess these differences

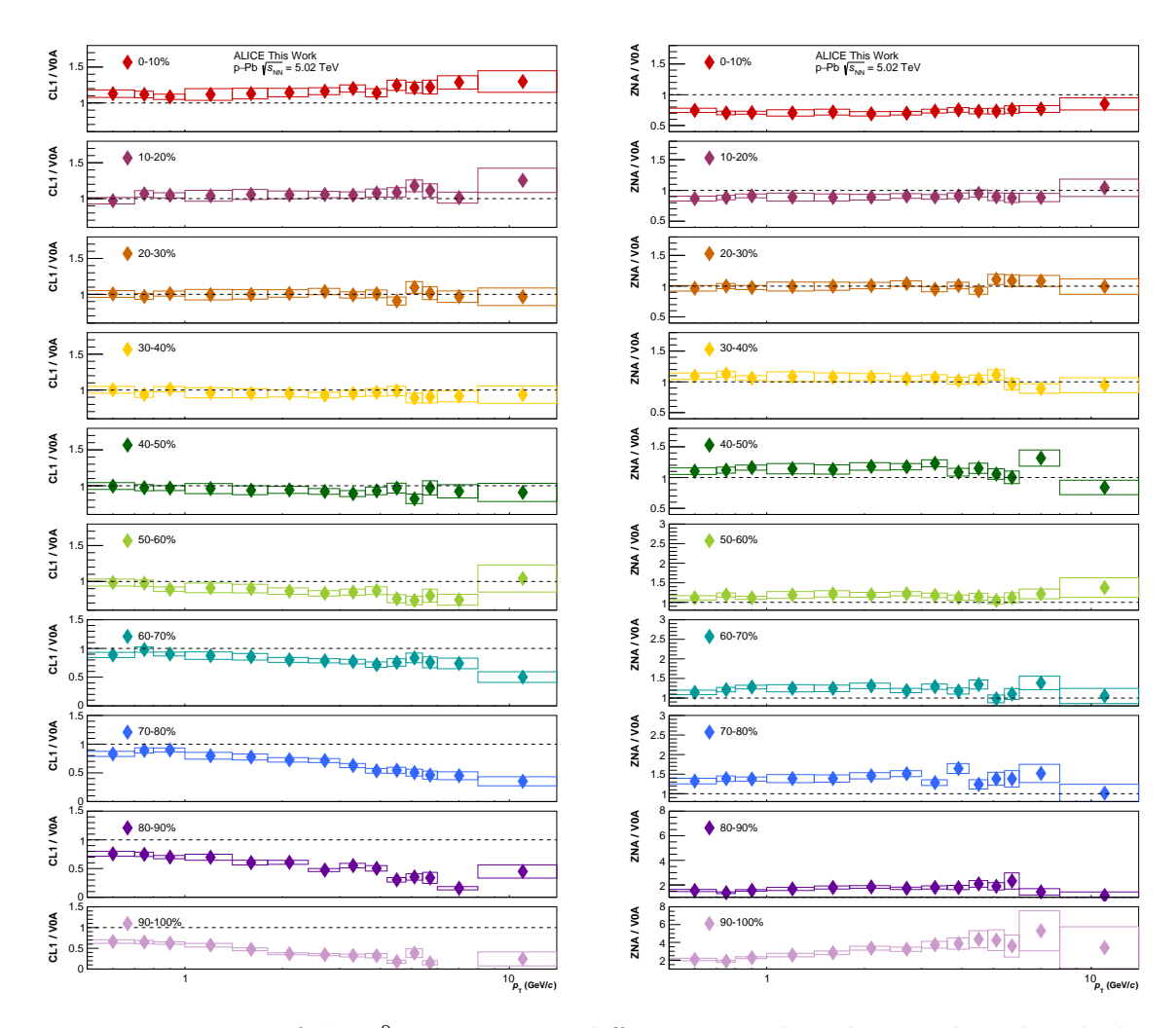


Figure 5.18: Ratio of the π^0 p_{T} -spectra in different centrality classes selected with the CL1 (*Left*) or the ZNA (*Right*) to the corresponding p_{T} -spectra selected with the V0A estimator.

quantitatively, this analysis compares the particle yields derived from multiple centrality estimators. This approach helps to clarify any variations introduced by the choice of estimator.

To measure the neutral-pion spectra, the data set is divided into ten centrality classes: 0-10%, 10-20%, 20-30%, 30-40%, 40-50%, 50-60%, 60-70%, 70-80%, 80-90%, 90-100%. The 0-10% class represents the most central collisions, while the 90-100% class includes the most peripheral ones.

For the η meson, the data is split into four centrality classes (0-20 %, 20-40 %, 40-60 %, 60-100 %) due to limited statistics, which prevented a more detailed separation by centrality. The analysis follows the same procedure as for the previously discussed minimum bias case.

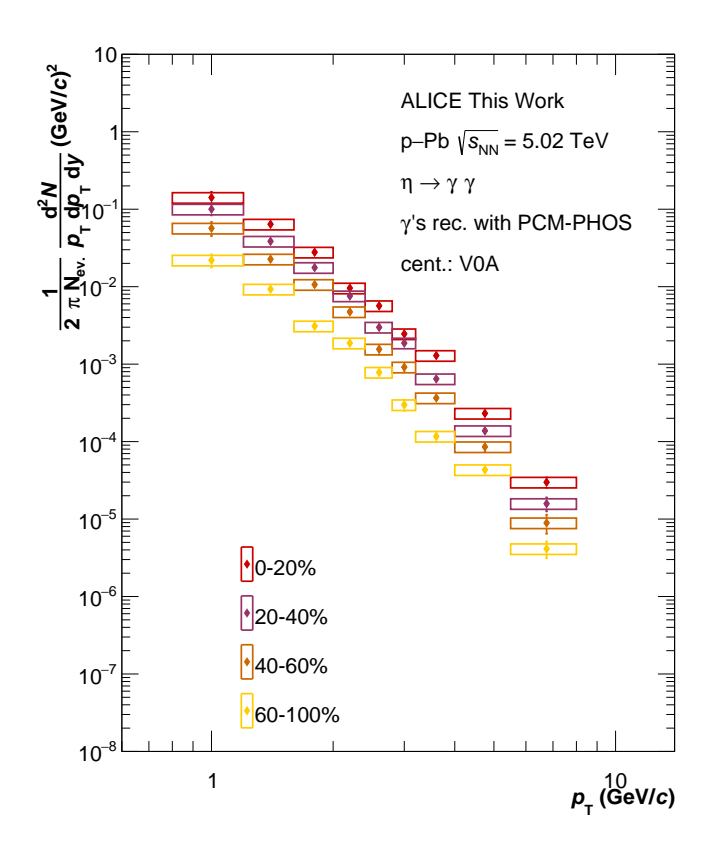


Figure 5.19: Centrality-dependent η $p_{\rm T}$ -spectra, selected with the V0A estimator.

Since the available statistics is limited within individual centrality classes, coarser $p_{\rm T}$ intervals are chosen. To reduce statistical uncertainties further, this analysis uses the centrality-integrated efficiency for the corrections.

Figure 5.16 shows the efficiency for the π^0 and η meson for different centrality classes as a ratio to the centrality-integrated efficiency. Aside from statistical fluctuations, no significant deviations from the centrality-integrated reconstruction efficiency are observed. Hence, the reconstruction efficiency of the centrality-integrated sample can be used for the further analysis.

For the estimation of systematic uncertainties, no significant differences between the minimum bias and centrality-dependent spectra are assumed as the efficiency is the same for all centrality intervals. Therefore, no additional systematic studies have been performed to those already presented.

Figure 5.17 presents the centrality-dependent yield of the neutral pion spectra for ten centrality classes using the V0A amplitude as the centrality estimator. As anticipated, the most central collisions show the highest particle yields, with yields decreasing as collisions become more peripheral. The centrality-dependent yield of the neutral

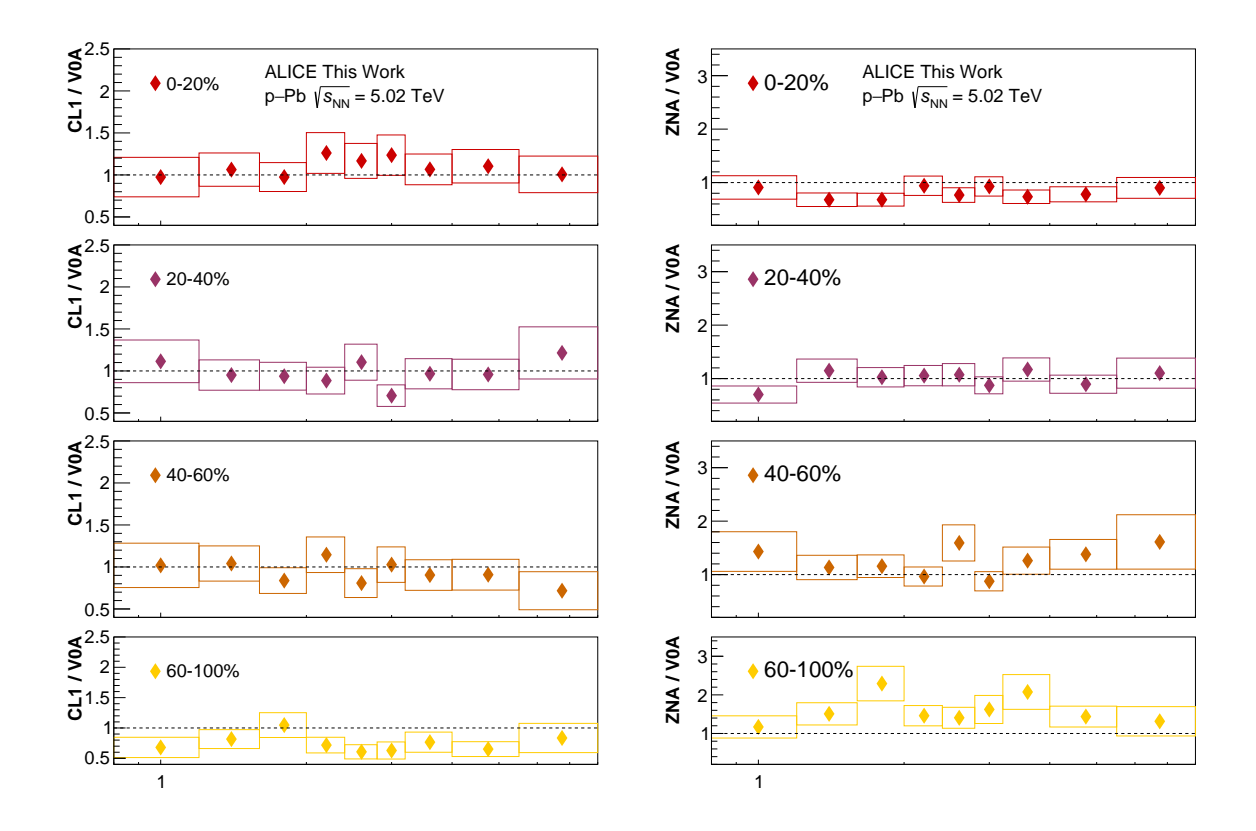


Figure 5.20: Ratio of the η $p_{\rm T}$ -spectra in different centrality classes selected with the CL1 (*Left*) or the ZNA (*Right*) to the corresponding $p_{\rm T}$ -spectra selected with the V0A estimator.

pion spectra is additionally measured using the CL1 and ZNA centrality estimator. The ratio of the neutral pion $p_{\rm T}$ -spectra in different centrality classes is shown in Figure 5.18 for the CL1 estimator in the left panel and for the ZNA estimator in the right panel. For both estimators strong deviations, particularly for peripheral collisions can be observed. The CL1 estimator particle yields are lower in peripheral collisions in comparison to the ones obtained with the V0A estimator. The ZNA estimator also shows a lower yield compared to V0A estimator. Depending on centrality, differences between the estimators range from approximately 40 % to 360 %, a discrepancy that has also been observed in charged particle measurements [35]. Figure 5.19 displays the centrality-dependent η meson yield, which, similar to the π^0 results, decreases as the collision centrality becomes more peripheral. Similar as to the π^0 the ratio of the η meson yield selected with the CL1 to the V0A estimator and the ZNA to the V0A estimator is shown on the right. Figure 5.20 shows again that the CL1 estimator for the centrality-dependent η measurement registers less η mesons. In contrast, the ZNA centrality estimator measures more η mesons for all centrality classes.

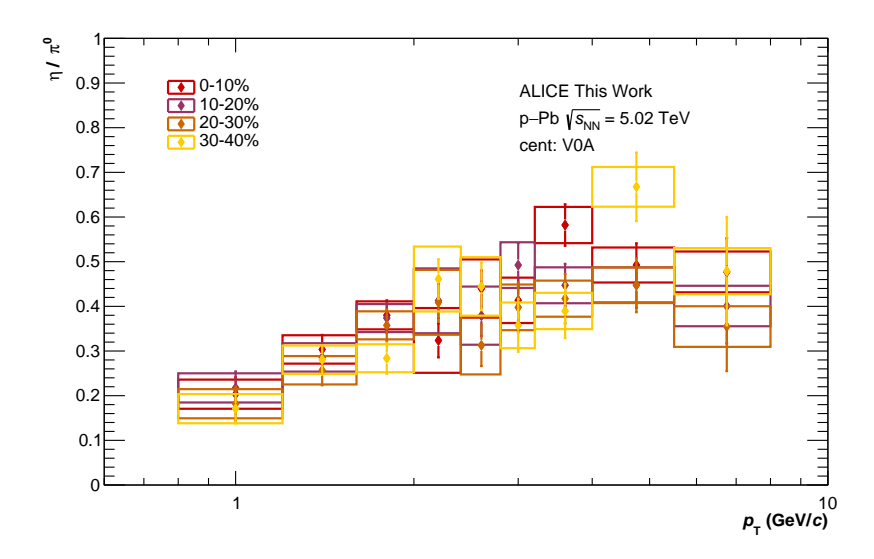


Figure 5.21: Centrality-dependent η/π^0 ratio obtained when using the V0A.

The measurements of both the π^0 and η meson spectra allow for the measurement of the centrality-dependent η/π^0 ratio as a function o $p_{\rm T}$, which is presented in Figure 5.21. Within the statistical and systematic uncertainties, the η/π^0 ratio shows no clear centrality dependence. This indicates that while the amount of produced particles varied across different centralities, the relative abundance of the mesons is unchanged. To estimate differences in particle production in different centrality classes, the centrality-dependent nuclear modification factor – $Q_{\rm pPb}$ – is calculated.

 $Q_{\rm pPb}$ Measurement The centrality-dependent measurement of the π^0 $p_{\rm T}$ spectra allows the investigation of the particle production as function of multiplicity, known as $Q_{\rm pPb}$. Such an analysis potentially provides valuable insight regarding the point at which a formation of a hot and dense medium, typically observed in Pb-Pb collisions, can be found in smaller collision systems. The mathematical expression for $Q_{\rm pPb}$ is identical to $R_{\rm pPb}$, except for the $\langle N_{\rm coll} \rangle$ values, which depend on centrality and the chosen centrality estimators. The $Q_{\rm pPb}$ can thus be expressed as:

$$Q_{\rm pPb} = \frac{\mathrm{d}N^{\rm pPb}/\mathrm{d}p_{\rm T}}{\langle N_{\rm coll,cent}\rangle \mathrm{d}N^{\rm pp}/\mathrm{d}p_{\rm T}}.$$
(5.9)

Since the values of the centrality-dependent $\langle N_{\rm coll,cent} \rangle$ depend on the centrality estimator, the reported differences in the meson yield can be mediated. Thus, the $Q_{\rm pPb}$ measurement can indicate whether the theoretical framework addresses biases across different centrality estimators.

Figure 5.22 shows the $p_{\rm T}$ -dependent $Q_{\rm pPb}$ measurement determined with the V0A, CL1 and ZNA centrality estimator. As the systematic uncertainties are the same among all centrality intervals except the signal extraction, the upper panel only includes the systematic uncertainties from the extraction while all other systematic uncertainties are displayed in the lower panel as relative uncertainties. For the CL1 and V0A estimators, a notable deviation from unity is visible across the full transverse momentum range. For the CL1 and V0A estimators, $Q_{\rm pPb}$ exceeds unity in central collisions and falls below unity in peripheral collisions. This is consistent with reported $Q_{\rm pPb}$ measurements for charged particles, where central collisions are above unity and peripheral collisions are below [35]. A similar trend in energy ordering and shape appears across centralities [35].

Unlike other estimators, the ZNA-selected $Q_{\rm pPb}$ values agree with unity for $p_{\rm T} > 2{\rm GeV}/c$ measurement, with signal suppression at lower transverse momentum increasing with centrality. This contrasts with the charged particle measurement where, especially in peripheral collisions, the ZNA estimator showed substantial deviations from unity [35]. Overall, these results suggest that potential measurement biases are best addressed by using the ZNA centrality estimator – as long no physical explanation for the deviations of the $Q_{\rm pPb}$ is expected.

This study shows that the geometrical correspondence of the experimental centrality selection is still a challenge and demand further investigation. Additional studies in this direction promise valuable input for the distinction of CNM and hot and dense matter effects.

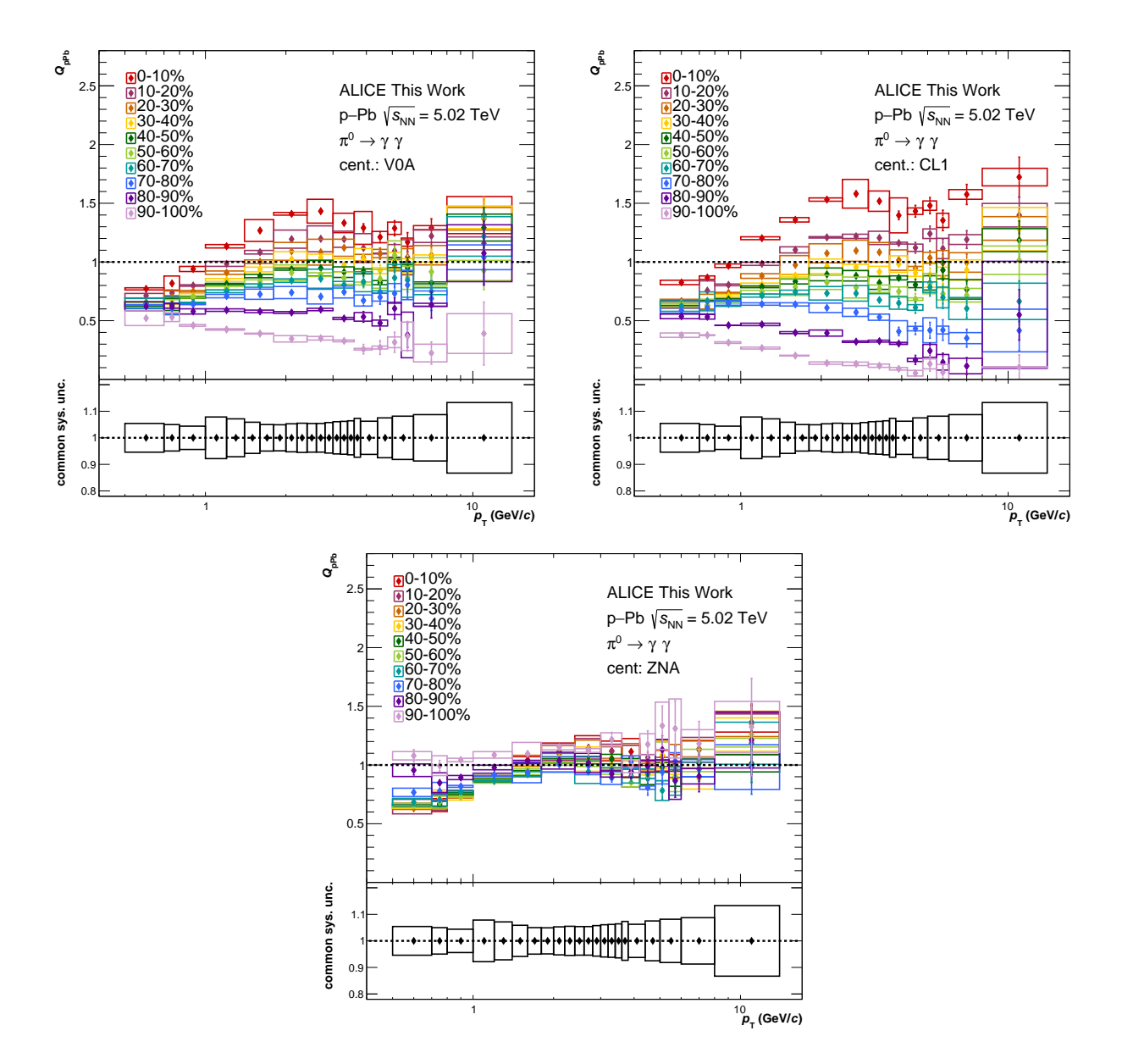


Figure 5.22: $Q_{\rm pPb}$ as a function of $p_{\rm T}$ determined using different centrality estimators: V0A ($Top\ Left$), CL1 ($Top\ Right$) and ZNA (Bottom). The charged pion $p_{\rm T}$ -spectrum is used as a reference [34].

6 Direct-Photon Measurement

The neutral meson measurements presented in the previous chapter serve as crucial input for the photon excess ratio R_{γ} , as detailed in Section 2.5, since they are the biggest contributor of decay photons to the inclusive photon yield. After discussing the inclusive photon analysis, the data-driven simulation of decay photons is presented in this chapter. Both components are then used for the R_{γ} calculation.

6.1 Inclusive Photon Yield

In contrast to the neutral meson measurement the inclusive photon yield is only extracted using the PCM method. Before the inclusive photon yield is used for to obtain the photon excess ratio, several corrections need to be applied. As only the PCM method is used for the photon measurement more corrections are needed as in the neutral meson measurement. The following sections will therefore introduce the necessary corrections and discuss the systematic uncertainties.

6.1.1 Corrections

Out-of-bunch pileup The TPC can reconstruct tracks from collisions that occur in bunch crossings before or after the event that triggered the data taking. These events are so-called out-of-bunch pileup events. If a pair of electron and positron tracks from the out-of-bunch pileup are reconstructed as a photon, this photon will contaminate the raw inclusive photon yield. Most out-of-bunch pileup tracks are only detected by the TPC. To quantify the contamination, photon candidates are grouped into three categories based on their track properties:

- 1. No track with hits in the ITS.
- 2. One track with hits in the ITS.
- 3. Two tracks with hits in the ITS.

In category 1 a significant amount of pileup is expected, while category 3 contains almost no pileup. The drift time of the electron and positron tracks from pileup collisions is biased, resulting in a shift of their z position. Therefore, the DCA_z distribution of the reconstructed photons can be used to identify out-of-bunch pileup.

Figure 6.1 depicts the DCA_z distributions for the three photon categories. While the distribution is widest for category 1 photons, it is narrower for category 2 and

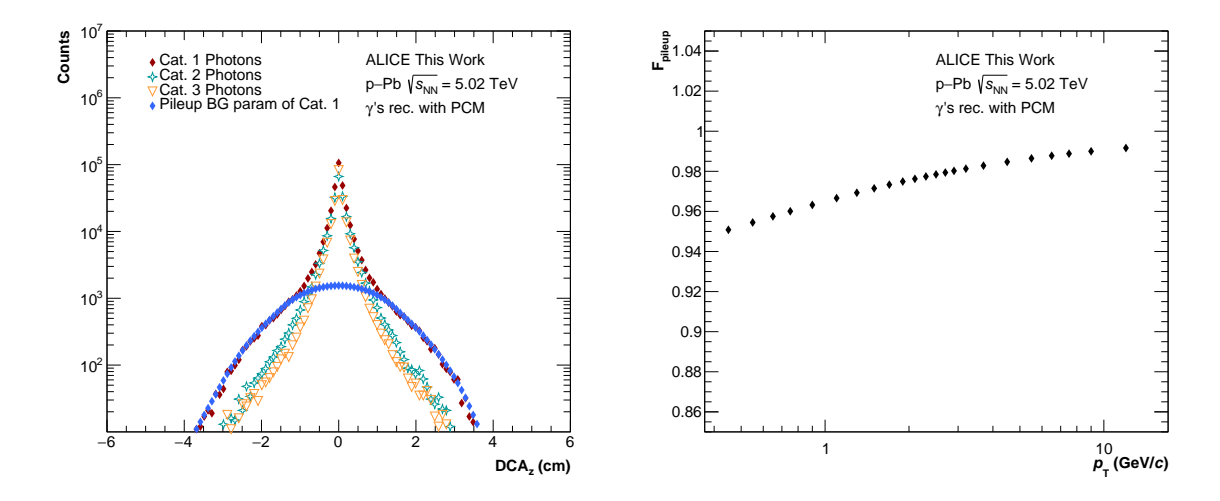


Figure 6.1: Left: DCA_z distribution for the three different photon categories. Right: Pileup correction factor as a function of $p_{\rm T}$.

the sharpest for category 3 due to the decreasing contributions form out-of-bunch pileup. To subtract the pileup contribution in the DCA_z distributions, the data is parameterized with a Gaussian function outside the signal region. The resulting background estimate for category 1 is shown in blue in the left panel of Figure 6.1. The same approach is chosen for the estimation of category 2 photons. The DCA_z distribution for category 2 shows a much narrower distribution than photons in category 1. Category 3 photons are depicted in yellow and show almost no pileup contribution.

To obtain a relative correction factor for the raw photon yield, the ratio of the pileupfree signal to all reconstructed photons is calculated as follows:

$$F_{\text{pileup}}(p_{\text{T}}) = \frac{\gamma_{\text{subtracted}}^{\text{cat1}}(p_{\text{T}}) + \gamma_{\text{subtracted}}^{\text{cat2}}(p_{\text{T}}) + \gamma_{\text{all}}^{\text{cat3}}(p_{\text{T}})}{\gamma_{\text{all}}^{\text{cat1}}(p_{\text{T}}) + \gamma_{\text{all}}^{\text{cat2}}(p_{\text{T}}) + \gamma_{\text{all}}^{\text{cat3}}(p_{\text{T}})}.$$
(6.1)

The resulting correction factor as a function of $p_{\rm T}$ is shown in the right panel of Figure 6.1. The out-of-bunch pileup contamination is largest at low transverse momenta where most photons originate from photons which only left tracking information in the TPC.

Secondary Decay Photons All photons not originating from the primary vertex are considered secondaries ($\gamma_{\rm sec}$) and contaminate the photon sample. Most of these photons stem from weak decays of the K_S^0 ; the second-largest sources are photons from decays of K_L^0 and Λ particles. As the K_L^0 and the Λ particle have a long decay

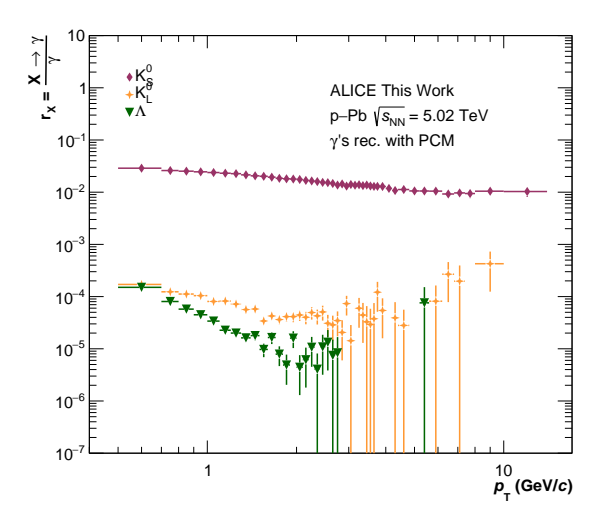


Figure 6.2: $p_{\rm T}$ -dependent fractions of photons stemming from weak decays obtained via the cocktail simulation.

time, their contribution to the background is strongly suppressed.

The secondary correction is performed with a particle cocktail simulation, as will be explained in the following Section 6.2. In this simulation, the K_S^0 , K_L^0 , and Λ are produced with the same probability for all momenta, and their decay is simulated using PYTHIA. The generated spectra are weighted with parameterized input spectra of previously measured K_S^0 and Λ particle spectra. The obtained secondary particle distributions are multiplied by their respective conversion probability and reconstruction efficiency obtained from a MC simulation in order to obtain the raw yield which can be subtracted from the inclusive photon yield.

The resulting fraction r_x of secondary photons with respect to all photons as a function of p_T is shown in Figure 6.2. The K_S^0 decays have the most significant contribution, while the other particles contribute with more than one order of magnitude less to the total photon yield. The raw secondary photon yield $\gamma_{\text{sec}}^{raw}$ can then be subtracted from the raw inclusive photon yield.

Purity The sample of V^0 candidates selected with the criteria discussed in Section 4.2.1 requires a purity correction, which is obtained via full MC simulation. The purity is defined as the fraction of genuine photons ($\gamma_{\rm rec,prim}^{\rm MC,true}$) to all the reconstructed photons ($\gamma_{\rm rec}^{\rm MC,all}$) in the sample. Since the reconstructed photon sample also include photons which stem from secondary particle decays ($\gamma_{\rm rec,sec}^{\rm MC,true}$) they need to be subtracted from the photon sample to obtain the purity. The purity is then calculated as follows:

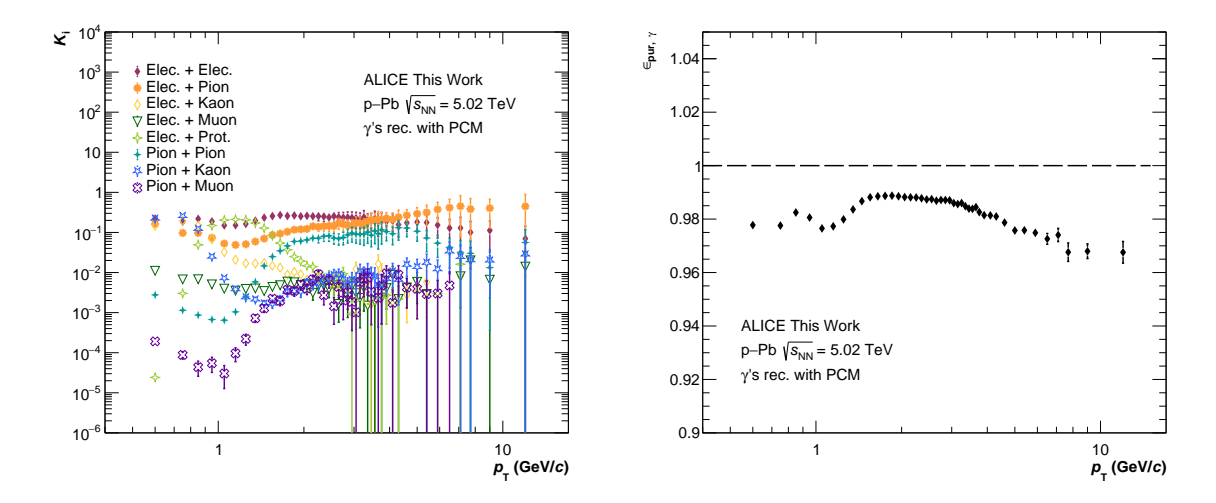


Figure 6.3: Left: MC-based ratio of different photon background sources to primary photons as a function of $p_{\rm T}$. Right: Purity of the photon candidate sample after selection as a function of $p_{\rm T}$.

$$\epsilon_{\text{pur},\gamma}(p_{\text{T}}) = \frac{\gamma_{\text{rec,prim}}^{\text{MC,true}}(p_{\text{T}})}{\gamma_{\text{rec}}^{\text{MC,all}}(p_{\text{T}}) - \gamma_{\text{rec,sec}}^{\text{MC,true}}(p_{\text{T}})}.$$
(6.2)

The magnitude of the falsely reconstructed photons is obtained via MC simulations. The left panel of Figure 6.3 shows the relative contributions K_i of the various possible photon backgrounds. A strong contribution from false e^+e^- pairs can be seen especially at low p_T . At higher p_T electron-pion contributions dominate.

The ratio gives a direct comparison of true primary photons to the reconstructed photons without including the secondaries. The right panel of Figure 6.3 shows the photon purity as a function of $p_{\rm T}$. The purity rises up to $p_{\rm T}=1.2\,{\rm GeV}/c$, but above this value, the purity decreases due to increased contamination from electron-pion pairs. This drop is primarily caused by the reduced effectiveness of the TPC ${\rm d}E/{\rm d}x$ energy loss cut, as electron and pion signals overlap in higher momentum regions. Overall, the high purity values of 97-99% reflect that the V^0 algorithm effectively suppresses contributions from false photon candidates.

Efficiency Correction The efficiency correction addresses the loss of conversion pairs due to the limited detector performance and the reconstruction capabilities for photons. The limited detector resolution as well as Bremsstrahlung lead to a smearing of the measured transverse momentum with respect to the true transverse momentum of the photons. To recover the true photon $p_{\rm T}$ a detector response matrix is used. The detector response matrix for the PCM method is shown in the left panel of Figure 6.4.

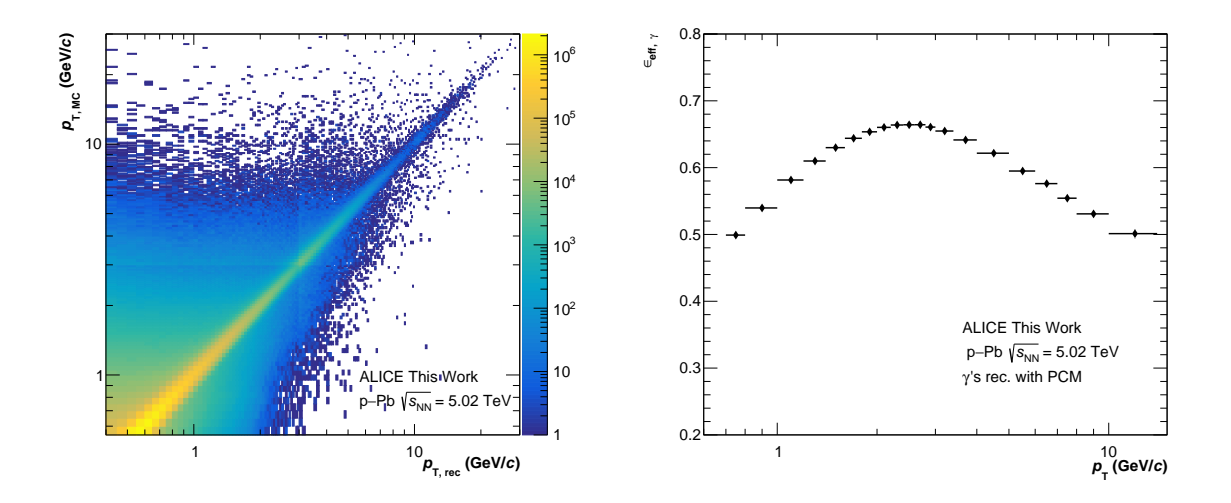


Figure 6.4: Left: Response matrix obtained from MC. Right: Reconstruction efficiency as a function of $p_{\rm T}$.

In this matrix, the generated photon transverse momentum is labeled as $p_{\rm T}^{\rm true}$, and the reconstructed transverse momentum, affected by detector smearing, is denoted as $p_{\rm T}^{\rm rec}$. Figure 6.4 illustrates that photons are often reconstructed with lower transverse momentum.

To retrieve the true transverse momenta, an unfolding method, implemented via the RooUnfold package [36], is employed. This algorithm begins with the initial $p_{\rm T}$ distribution generated by the MC simulation and iteratively refines the distribution in each step to achieve the corrected result.

The photon reconstruction efficiency ($\epsilon_{\rm eff,\gamma}$) can then be obtained by dividing the reconstructed MC validated photons ($\gamma_{\rm rec,prim}^{\rm MC,true}$) by all conversion photons ($\gamma_{\rm all,prim}^{\rm MC,conv}$) obtained in the simulation, as shown in the following equation:

$$\epsilon_{\text{eff},\gamma}(p_{\text{T}}^{\text{true}}) = \frac{\gamma_{\text{rec,prim}}^{\text{MC,true}}(p_{\text{T}}^{\text{true}})}{\gamma_{\text{all,prim}}^{\text{MC,conv}}(p_{\text{T}}^{\text{true}})}.$$
(6.3)

This also ensures that the detector material conversion is included in the efficiency. The right panel of Figure 6.4 shows the reconstruction efficiency ($\epsilon_{\text{eff},\gamma}$) for the PCM method. As in the neutral meson measurement, a drop of the reconstruction efficiency towards low p_{T} can be observed. This decrease can be attributed to the fact that the conversion pair either cannot reach the TPC or that the pair is unable to pass the requirement of a minimum radial distance in the TPC. The decrease of the reconstruction efficiency at higher p_{T} indicates that the conversion product cannot be reconstructed because of dead areas inside the TPC [25].

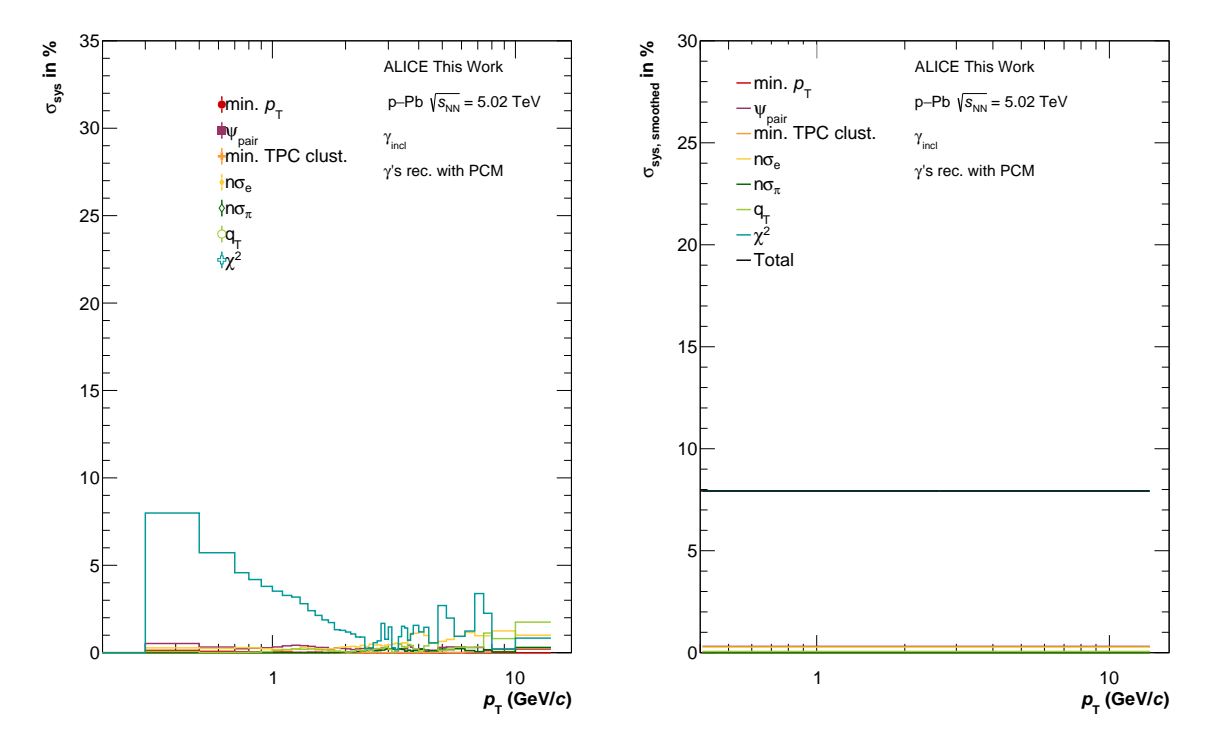


Figure 6.5: Left: Systematic uncertainty as a function of $p_{\rm T}$ for the inclusive photons, based on the applied variations, where the $p_{\rm T}$ dependent fluctuations have not yet been smoothed. Right: Systematic uncertainty for the inclusive photons as function of $p_{\rm T}$ after smoothing.

Systematic Uncertainties The uncertainties are determined in the same manner as the systematic uncertainties of the neutral meson measurement, described in Section 5.3. Again, the uncertainty for each contribution is obtained by studying the variations (varied $p_{\rm T}$ spectra) to the $p_{\rm T}$ spectrum using the standard parameters (standard $p_{\rm T}$ spectrum). The magnitude of the systematic uncertainty is then calculated as the root mean square of the maximum positive deviation Δ^+ and the maximum negative deviation Δ^- between the varied $p_{\rm T}$ spectra and the standard $p_{\rm T}$ spectrum. Since the inclusive photon measurement relies exclusively on the PCM method, not all previously studied contributions affect this measurement. Therefore, only uncertainties relevant to the PCM method are included. To ensure the cancellation of the systematic uncertainties in the excess ratio, the studied variation is the same as for the neutral meson measurement. Figure 6.5 illustrates the systematic uncertainties as a function of $p_{\rm T}$, where the $p_{\rm T}$ -dependent fluctuations have not been smoothed and the uncertainties obtained after smoothing. The plot does not show the material budget uncertainty, which is estimated to be 2.5 % per photon [31].

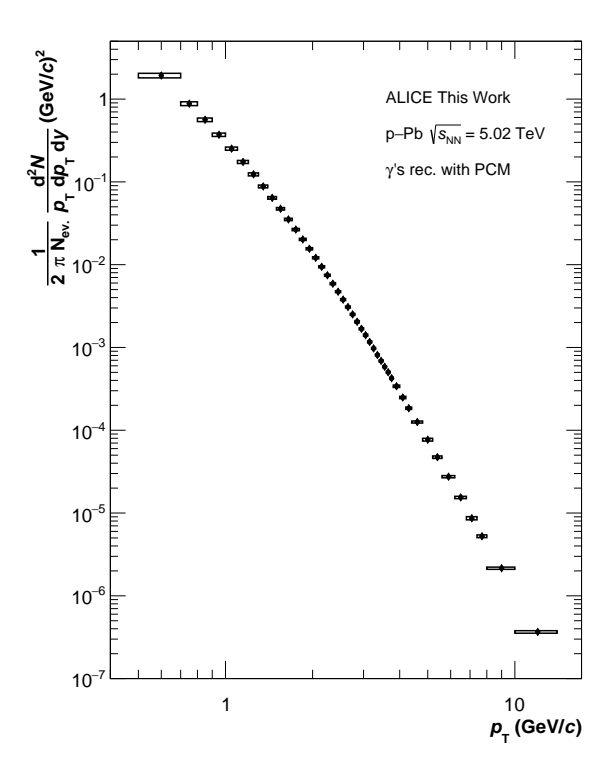


Figure 6.6: Fully corrected $p_{\rm T}$ -dependent inclusive photon yield.

6.1.2 Corrected Inclusive Photon Yield

After applying all the necessary corrections to the raw photon spectrum, one finally obtains the fully corrected primary inclusive photon yield. The pileup correction (F_{pileup}) is first applied to the PCM photon raw yield $(\gamma_{\text{incl}}^{\text{raw}})$ and then the secondary photons $(\gamma_{\text{sec}}^{\text{raw}})$ are subtracted. The corrected yield $(\gamma_{\text{incl}}^{\text{corr}})$ is therefore obtained via the following:

$$\gamma_{\text{incl}}^{\text{corr}}(p_{\text{T}}) = \left(F_{\text{pileup}}(p_{\text{T}}) \times \gamma_{\text{incl}}^{\text{raw}}(p_{\text{T}}) - \sum_{i=\text{K}_{\text{s}}^{0},\text{K}_{\text{L}}^{0},\Lambda,\text{Rest}} \gamma_{\text{sec,i}}^{\text{raw}}(p_{\text{T}})\right) \times \frac{\epsilon_{\text{pur},\gamma}(p_{\text{T}})}{\epsilon_{\text{eff},\gamma}(p_{\text{T}})}. \quad (6.4)$$

The resulting spectrum contains all primary photons that are produced in the pseudorapidity region of $|\eta| < 0.8$ and 2π in azimuth. To obtain the invariant yield, the spectrum is further normalized to the number of events. Figure 6.6 shows the $p_{\rm T}$ -dependent inclusive photon yield obtained using the PCM method along with the statistical and systematic uncertainties. This yield reaches the same $p_{\rm T}$ range of $0.5 < p_{\rm T} < 14\,{\rm GeV}/c$ as the neutral pion measurements.

With the inclusive photons measured for extracting the excess ratio, the next step is to estimate the decay photons.

6.2 Decay Photons

The determination of decay photon yields relies on dedicated simulations. General-purpose MC simulations like DPMJet, HIJING, or EPOS LHC, introduced in Section 4.1, are unsuitable for this task as they do not describe the correct relative particle abundances as seen in Section 5.4. Instead, this analysis employs data-driven decay simulations, also known as particle cocktail simulation, which model the complete decay chain of the particles involved. To accurately determine particle abundances, measured particle spectra parameterizations are used as inputs for these simulations. This section first details the cocktail simulation inputs and then discusses the resulting outputs.

6.2.1 Particle Cocktail Input

As previously discussed, the simulations for the estimation of the decay photons rely on parameterized particle spectra and particle ratios to estimate the decay products. In addition to the neutral meson measurements discussed in this thesis, inputs for the particle cocktail include measurements of the ω meson [37, 38], kaons [30], charged pions [30], lambda baryons [30], ϕ mesons [39], and protons [30] – all obtained from previous measurements by ALICE. Since all measurements cover a limited $p_{\rm T}$ -reach, the data is parameterized using different empirical functions.

For the parameterization of the π^0 meson spectrum, a modified Hagedorn function [40] is used:

$$f(p_{\rm T}) = A \cdot \left(\exp(ap_{\rm T} + bp_{\rm T}^2) + \frac{p_{\rm T}}{p_0} \right)^{-n}.$$
 (6.5)

The same parameterization function has also been chosen for the parameterization of the K_S^0 , K_L^0 and Λ particle, where the free parameters are adjusted for the different particles.

To estimate the decay contribution from the η meson, the η/π^0 ratio is parameterized and afterwards multiplied by the measured neutral pion yield. Since some systematic uncertainties cancel in the ratio, the degrees of freedom for the parameterization are more limited and therefore the uncertainties in general become much lower. To parameterize the ratio, an empirical function is used. The function uses a blast-wave component to describe the soft part of the spectra and a power-law component to describe the hard part of the spectrum. The resulting functional form of the

parameterization is given by [25]:

$$\frac{\eta}{\pi^0} (p_{\mathrm{T}}) = \frac{A \cdot \exp\left(\frac{\beta p_{\mathrm{T}} - m_{\mathrm{T}}^{\eta}}{T\sqrt{1-\beta^2}}\right) + C \cdot R \cdot \left(1 + \left(\frac{p_{\mathrm{T}}}{p^0}\right)^2\right)^{-n}}{\exp\left(\frac{\beta p_{\mathrm{T}} - m_{\mathrm{T}}^{\eta^0}}{T\sqrt{1-\beta^2}}\right) + R \cdot \left(1 + \left(\frac{p_{\mathrm{T}}}{p_0}\right)^2\right)^{-n}}.$$
(6.6)

Here, the factor R is a relative normalization of the soft and hard part of the parameterized spectrum and C is the constant ratio between the two particles which can be observed for higher transverse momenta. The soft component of the spectrum is dependent on a radial flow velocity β and the kinetic freeze-out temperature T.

A recent measurement of the ω meson at this center-of-mass energy has been performed, which now also includes the first ω meson measurement for the particle cocktail [37, 38]. To parameterize the ω spectrum, a similar approach as for the η meson was chosen. The available measurement of the ω meson in p-Pb collision at this center-of-mass energy, however, poses a challenge since its lowest transverse momentum is $p_T = 2 \, \text{GeV}/c$. For the parameterization of the spectrum this was especially problematic as there was no constrain for lower p_T values and the ω meson contribution was overestimated by the cocktail. Therefore, this analysis combines the measurements with a dilepton ω measurement in pp collisions, as the ratio is believed to be independent of the collision system. Figure 6.7 shows both the ω/π^0 ratio measurement that was obtained via the described method together with parameterization of the ω/π^0 .

Instances in which the particle spectra of the respective cocktail ingredients have not been measured yet, the parameterization is obtained by transverse mass $(m_{\rm T})$ scaling. Underlying the scaling relation is the assumption that hadron production is described by a universal scaling law, as described by a statistical-thermodynamical model. Therefore, particle spectra can be described using an exponential function with a slope parameter which has a universal value when they are expressed as a function of $m_{\rm T} = \sqrt{p_{\rm T}^2 + m_0^2}$, where m_0 denotes the particles mass at rest. The mathematical form of the scaling is therefore:

$$P_{\rm m/b}(m_{\rm T}) = C_{\rm T} \cdot P_{\pi^0/p}(m_{\rm T}),$$
 (6.7)

where $P_{\pi^0/p}$ is the neutral pion parameterization or proton parameterization respectively and $C_{\rm T}$ denotes the constant scaling factor. As explained, the proton is not a direct source of particle decay but rather used to create a reference for the $m_{\rm T}$ scaling

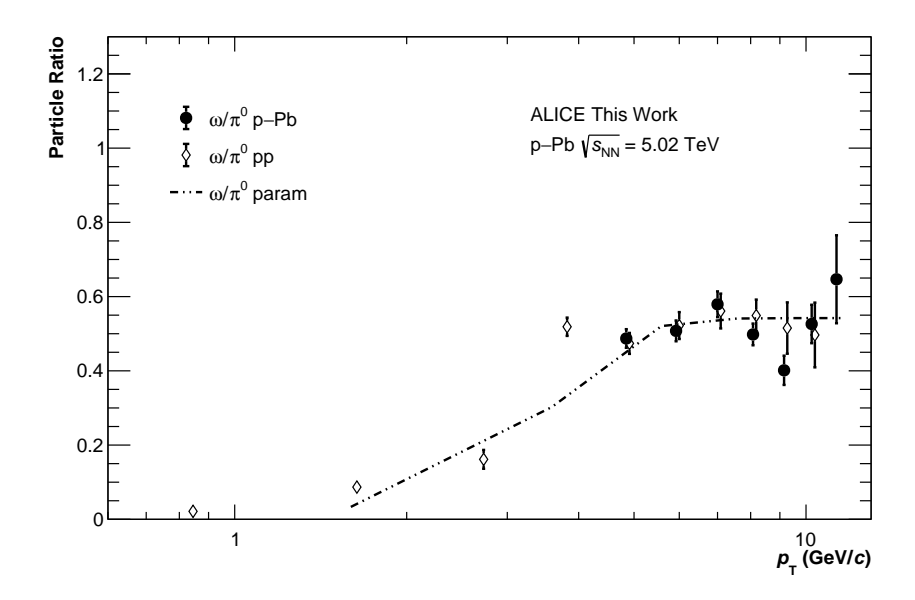


Figure 6.7: Parameterization of the ω/π^0 ratio for p–Pb and pp collision used for this analysis.

of the Δ^0 , Δ^+ and Σ^0 .

The different contributions of the generated mother particles as well as their ratio to the neutral pion or proton spectrum are depicted in Figure 6.2. At low transverse momenta the π^0 , η form the most, followed by ω and η' mesons. At higher transverse momentum, however, the contributions from the ρ mesons gain increasing importance. These parameterizations and ratios can then be used for the cocktail simulations.

6.2.2 Particle Cocktail Simulation and Output

The decay spectra are generated using the PYTHIA 6.4 decayer, which simulates the decay of generated mother particles listed in Table 8.3. The branching ratios in the table are applied to replicate the full decay chain of each particle. For direct-photon measurements only decays from primary particles are considered. The generated particles span a transverse momentum range of $0 < p_T < 50 \,\mathrm{GeV}/c$, a rapidity range of $|\eta| < 1.0$, and full azimuthal coverage $0 < \phi < 2\pi$. Each decay simulation consists of one million events with 1000 particles per species, ensuring minimal contributions to statistical uncertainties of the spectra. Finally, the decay spectra are scaled using the p_T -dependent parameterizations outlined in the previous section and adjusted to the relevant rapidity range to consider the same fiducial zone.

The left panel of Figure 6.8 shows the parameterized mother particles. The decay photon spectra, which are obtained via the simulation are depicted on the right

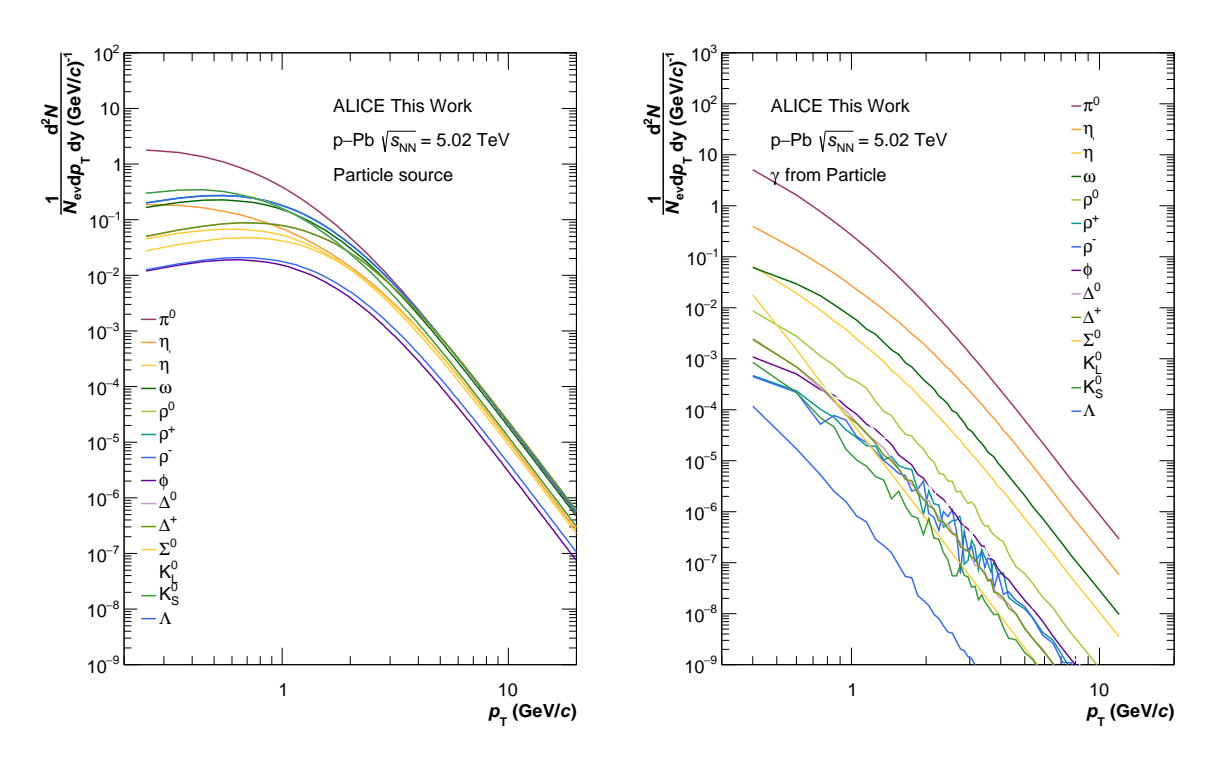


Figure 6.8: Left: Mother particle spectra from the particle cocktail simulation. Right: Decay photon spectra from the particle cocktail simulation.

panel of Figure 6.8. Since the statistics of the decay photon cocktail was limited, statistical fluctuations lead to the kinks in the spectra. As previously stated, the biggest contribution originates from neutral π^0 with $\approx 80\%$ and the η meson with a contribution of about 10%. The light neutral meson contributions are followed by ω and η' mesons which contribute at least one order less of a magnitude to the decay photon cocktail.

As explained in Section 2.5, when calculating the photon excess ratio via the double ratio, decay photons are normalized using the neutral pion spectrum obtained from the cocktail simulation. To validate the simulation, the measured neutral pion spectrum is compared to the generated spectrum from the cocktail. Significant deviations from unity in the ratio would directly lead to an overestimation of the photon yield, distorting the direct-photon measurement. Figure 6.9 illustrates the ratio of measured neutral meson spectra to the generated neutral pion spectrum as a function of $p_{\rm T}$. Across the entire transverse momentum range, no significant deviations are observed, confirming the reliability of the particle cocktail simulation.

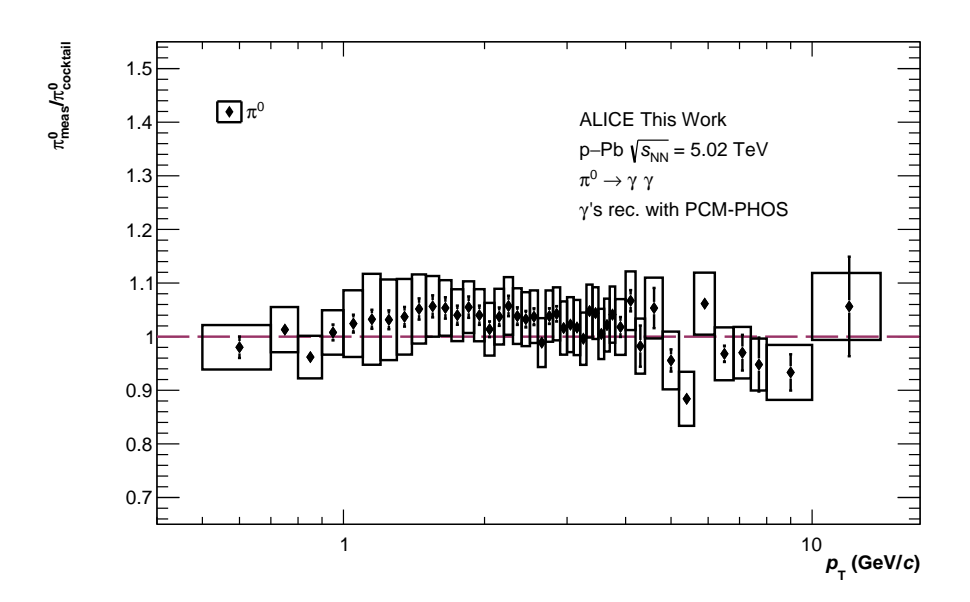


Figure 6.9: Ratio of the neutral pion spectrum to the neutral pion spectrum obtained via the cocktail simulation.

6.3 Results

To measure the photon excess ratio, this analysis uses the double ratio method, as explained in Section 2.5. The double ratio compares the ratio of the measured photon signal to the measured neutral pion spectrum to the same ratio obtained from the cocktail simulation, given as:

$$R_{\gamma} = \frac{(\gamma_{\text{incl}}/\pi^0)_{\text{meas}}}{(\gamma_{\text{dec}}/\pi^0_{\text{param}})_{\text{cocktail}}}.$$
(6.8)

Here, $\gamma_{\rm incl}$ represents the inclusive photon transverse momentum distribution, which includes both direct and decay photons. The decay photon spectrum from the cocktail simulation is denoted by $\gamma_{\rm dec}$ and π^0 corresponds to the neutral pion spectra. An excess ratio above unity would indicate that during the collisions, photons were produced through soft or hard processes, as explained in Section 2.5.

In Figure 6.10 the excess ratio for the calculated ratio of the inclusive photon sample and the measured neutral pion spectrum $(\gamma/\pi^0)_{\text{meas}}$ and the cocktail based $(\gamma/\pi^0)_{\text{cocktail}}$ ratio is depicted. Within the given uncertainties, no excess above unity is observed. The measurement shows that the results are compatible with the NLO pQCD calculations which are drawn in yellow.

In general, the measurement revealed that within the systematic uncertainties no

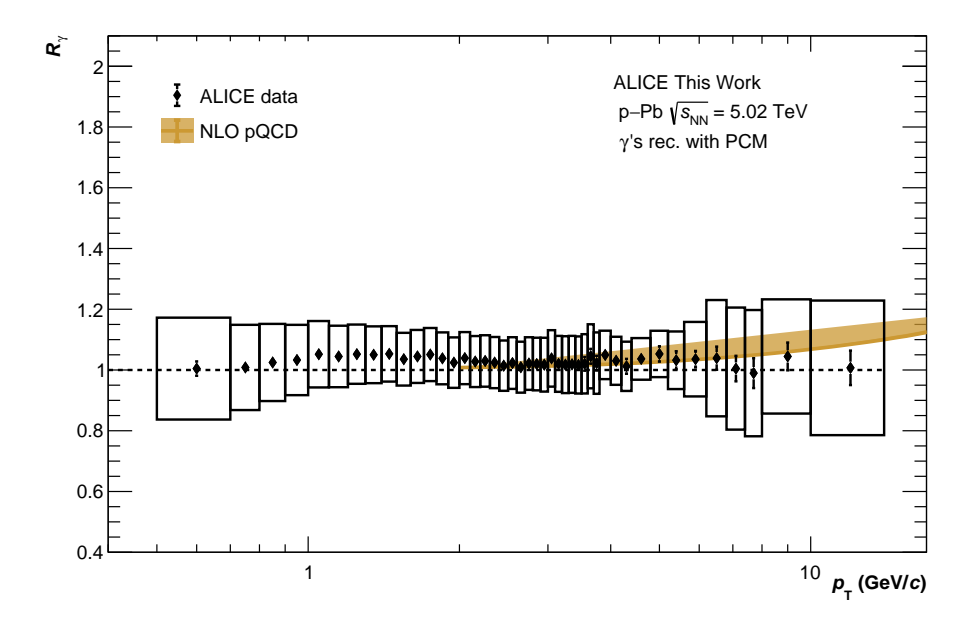


Figure 6.10: R_{γ} for p–Pb collisions at $\sqrt{s_{\mathrm{NN}}} = 5.02\,\mathrm{TeV}$.

excess of thermal or prompt direct photons can be observed. This is in agreement with previous measurements previously discussed in Section 2.5.1.

7 Summary

This thesis presents the transverse momentum spectra of π^0 and η mesons in p–Pb collisions at $\sqrt{s_{\rm NN}}=5.02\,{\rm TeV}$ recorded with the ALICE experiment in LHC Run 2. The neutral mesons are measured via their two-photon decay channel. One photon is measured with the Photon Conversion Method (PCM), which reconstructs photons converted to electron-positron pairs. The second photon is measured with one of the electromagnetic calorimeters in ALICE, the Photon Spectrometer (PHOS). The invariant mass distribution of all possible photon pairs contains background contamination which is estimated using a MC template method. After background subtraction, the raw meson yield is determined for various $p_{\rm T}$ -intervals by integrating around the meson's peak in the invariant mass distribution.

The raw yield is corrected for the contamination with secondary neutral pions using a data-driven cocktail simulation. The corrections for detector acceptance and efficiency are determined via MC simulations. The resulting transverse momentum spectra cover $0.5 < p_{\rm T} < 14\,{\rm GeV}/c$ for the π^0 meson and $0.8 < p_{\rm T} < 12\,{\rm GeV}/c$ for the η meson. Their total systematic uncertainty is in the range of 7-25 % for the π^0 and 16 % for the η meson depending on the transverse momentum. The uncertainties are dominated by the requirement of a minimum cluster energy in the PHOS detector.

The corrected spectra are compared to previous measurements from Run 1. In the mid $p_{\rm T}$ region, the π^0 measurement agrees with the previous results within the uncertainties, while the Run 1 PCM measurement is consistently above the measured data points. This can be understood as an effect of the updated material budget weights used for this analysis. The results for the η meson are qualitatively similar.

In addition, the results of this thesis are compared to predictions from the MC event generators EPOS LHC, HIJING, and DPMJet. While EPOS LHC provides a good description of the measured π^0 $p_{\rm T}$ spectrum, HIJING and DPMJet cannot reproduce its shape. For the η , meson all generators fail to describe the spectrum. Therefore, also the η/π^0 ratio is also not well reproduced by the MC event generators.

The combination of the measured $p_{\rm T}$ spectrum of the π^0 meson and the published charged pion measurement for pp collisions, allows to extract the nuclear modification factor $R_{\rm pPb}$. This observable agrees with unity for $p_{\rm T} > 2\,{\rm GeV}/c$, which is consistent with previous measurements as well as theoretical predictions based on NLO pQCD calculations.

The minimum-bias measurements are complemented by a centrality-dependent ana-

lysis of both neutral mesons. To classify the centrality of the p–Pb collisions, three different centrality estimators are used. For the neutral pion, the data set is divided into ten centrality classes: 0-10 %, 10-20 %, 20-30 %, 30-40 %, 40-50 %, 50-60 %, 60-70 %, 70-80 %, 80-90 %, 90-100 %. Due to the lower statistics, for the η meson the data is divided into five broader centrality classes: 0-20 %, 20-40 %, 40-60 %, 60-100 %. When performing the centrality-dependent analysis, larger $p_{\rm T}$ -intervals are chosen to account for the reduced statistics as compared to the minimim-bias measurement. The systematic uncertainties are estimated analogously to the minimum-bias case. The resulting $p_{\rm T}$ spectra at the same centrality differ greatly depending on the centrality estimator. Consequently, the centrality-dependent equivalent of $R_{\rm pPb}$, the so-called $Q_{\rm pPb}$, depends on the used centrality estimator. This aligns with previous studies that investigated centrality-estimator biases of charged particle measurements in p–Pb collisions. However, the observed trends show quantitative – and, in some cases, qualitative – differences from those discussed in the publication. This suggests that further studies are required to better assess these biases.

The presented neutral meson measurements are a vital input to the direct photon analysis. The neutral mesons are the largest source of decay photons and are used to extract the direct photon excess ratio R_{γ} . The inclusive photon yield is measured using the PCM method, since it provides a high photon purity over the whole analyzed transverse momentum range. When estimating the contributions from decay photons of ω mesons this analysis uses for the first time an experimental measurement for the particle decay cocktail instead of employing $m_{\rm T}$ -scaling. The resulting direct photon excess ratio R_{γ} shows no signal above unity within the uncertainties and thus agrees with the existing literature and NLO pQCD calculations.

The measurements presented in this thesis consolidate and extend the existing canon of theory and experimental data. The results allow for better constrains of nuclear PDFs and can serve as a baseline for more differential analyses.

8 Appendix

8.1 Run List

Data Set	Runs
	265309, 265332, 265334, 265335, 265336, 265338, 265339,
	265342, 265343, 265344, 265377, 265378, 265381, 265383,
LHC16q	286384, 265385, 265387, 265388, 265419, 265420, 265421,
	265422, 265424, 265425, 265426, 265427, 265435, 265499,
	265500, 265501, 265521, 265525
LHC16t	267163, 267164, 267165, 267166

8.2 $p_{\rm T}$ Intervals

$p_{\rm T}$ interval ranges in ${ m GeV}/c$				
0.5, 0.7, 0.8, 0.9, 1.0, 1.1, 1.2, 1.3,				
1.4, 1.5, 1.6, 1.7, 1.8, 1.9, 2.0, 2.1,				
2.2, 2.3, 2.4, 2.5, 2.6, 2.7, 2.8, 2.9,				
3.0, 3.1, 3.2, 3.3, 3.4, 3.5, 3.6, 3.7,				
3.8, 4.0, 4.2, 4.4, 4.8, 5.2, 5.6, 6.2,				
6.8, 7.4, 8.0, 10.0, 14.0				
0.5, 0.7, 0.8, 0.9, 1.0, 1.1, 1.2, 1.3,				
1.4, 1.5, 1.6, 1.7, 1.8, 1.9, 2.0, 2.1,				
2.2, 2.3, 2.4, 2.5, 2.6, 2.7, 2.8, 2.9,				
3.0, 3.1, 3.2, 3.3, 3.4, 3.5, 3.6, 3.7,				
3.8, 4.4, 5.0, 6.0, 8.0, 12.0				
0.8, 1.2, 1.6, 2.0, 2.2, 2.4, 2.6, 3.0,				
3.4, 3.8, 4.2, 4.6, 5.0, 6.0, 8.0, 12.0				
0.8, 1.2, 1.6, 2.0, 2.2, 2.4, 2.6, 3.0,				
3.4, 3.8, 4.2, 4.6, 5.0, 6.0, 8.0				

8.3 Contributions to the Decay Cocktail

Particle	$\frac{\mathrm{Mass}}{(\mathrm{MeV}/c)}$	Reference	Decay Channels	Branching Ratio	Contribution	
π^0	134.98	this thesis	$e^{-}e^{+}\gamma$	9.882E-01 1.174E-02	> 80%	
			$\gamma\gamma$	3.941E-01		
			$\pi^0 \gamma \gamma$	2.560E-04	10-15%	
η	547.85	this thesis	$\pi^+\pi^-\gamma$	4.220E-02		
·			$e^-e^+\gamma$	6.889E-03		
			$\frac{\mu^-\mu^+\gamma}{\pi^0\gamma}$	3.090E-04		
			$\pi^0\gamma$	8.350E-02		
ω	782.65	32.65 [37, 38]	$\eta\gamma$	4.600E-04	$\approx 2.8\%$	
			$\pi^0\pi^0\gamma$	7.000 E-05		
			$\rho^0 \gamma$	2.098E-01		
$\eta^{'}$	957.66	$m_{\rm T}$ scaling from π^0	$\omega\gamma$	2.746E-02	$\approx 1.4\%$	
"/			$\gamma\gamma$	2.198E-02		
			$\frac{\mu^{+}\mu^{-}\gamma}{\pi^{+}\pi^{-}\gamma}$	1.080E-04		
				9.900E-03		
$ ho^0$	775.49	$m_{\rm T}$ scaling from π^0	$\pi^0\gamma$	6.000E-04	<1%	
ρ	110.43	$m_{ m T}$ scanng from π^*	$\eta\gamma$	3.000E-04		
			$\pi^0\pi^0\gamma$	4.500E-05		
$ ho^+$	775.49	$m_{\rm T}$ scaling from π^0	$\pi^+\gamma$	4.500E-04	<1%	
ρ^-	110.43	m scanng nom n	$\pi^-\gamma$	4.500E-04	<u> </u>	
			$\eta\gamma$	1.310E-02		
	1019.46		$\pi^0\gamma$	1.273E-03		
			$\pi^+\pi^-\gamma$	4.100E-05		
ϕ		[39]	$\pi^0\pi^0\gamma$	1.130E-04	< 1%	
				$\pi^0\eta\gamma$	7.300E-05	
			$\eta^{'}\gamma$	6.300E-05		
			$\mu^+\mu^-\gamma$	1.400E-05		
Δ^+	1232	$m_{\rm T}$ scaling from π^0	$n\gamma$	4.500E-04	<1%	
$\frac{\Delta^{-}}{\Xi^{0}}$			$p\gamma$	4.500E-04	<1%	
Σ^0	1192.64	$m_{\rm T}$ scaling of proton	$\Lambda\gamma$	1.000E+0	<1%	
K_S^0	497.61	[30]	$\pi^+\pi^-\gamma$	6.000E-03	<1%	
	101.01	g 457.01 [00]	[00]	$\pi^{0}\pi^{0}$	6.000E-03	
K_L^0	497.61	497.61 [30]	$\pi^{\pm}e^{\mp}\nu\gamma$	3.988E-03		
			$\pi^{\pm}\mu^{\mp}\nu\gamma$	4.920E-04		
			$\pi^+\pi^-\gamma$	4.200E-05	. ~	
			$\gamma\gamma$	5.500E-04	<1%	
			$\pi^{0}\pi^{0}\pi^{0}$	1.946E-01		
			$\pi^{+}\pi^{-}\pi^{0}$	1.250E-01		
			$\pi^0\pi^0$	8.630E-04		
Λ	1115.68	[30]	$n\gamma$	8.400E-04	<1%	
		ı J	$n\pi^0$	3.580E-01		

References

- [1] ALICE, "The ALICE experiment: a journey through QCD", Eur. Phys. J. C 84 no. 8, 813, arXiv:2211.04384 [nucl-ex], 2024.
- [2] O. Philipsen, "Quantenfeldtheorie und das Standardmodell der Teilchenphysik: Eine Einführung", 1. aufl. 2018. ed., 2018.
- [3] H. Büsching, "Kern- und Teilchenphysik 4b: Die Physik des Quark-Gluon-Plasmas", 2021.
- [4] A. Maire, "Phase diagram of QCD matter: Quark-Gluon Plasma", https://cds.cern.ch/record/2025215, 2015. General Photo.
- [5] F. Gross *et al.*, "50 Years of quantum chromodynamics: Introduction and Review", *The European Physical Journal C* 83 no. 12, 2023.
- [6] ALICE, "Transverse momentum spectra and nuclear modification factors of charged particles in pp, p-Pb and Pb-Pb collisions at the LHC", JHEP 11 013, arXiv:1802.09145 [nucl-ex], 2018.
- [7] N. Armesto, "Nuclear shadowing", Journal of Physics G: Nuclear and Particle Physics 32 no. 11, R367, 2006.
- [8] J. Aubert *et al.*, "The ratio of the nucleon structure functions F2N for iron and deuterium", *Physics Letters B* 123 no. 3, 275–278, 1983.
- [9] M. Sas, "Illuminating Light". PhD thesis, Utrecht University, 2021. https://cds.cern.ch/record/2774578.
- [10] ALICE, "Direct photon production in Pb-Pb collisions at $\sqrt{s_{\rm NN}} = 2.76$ TeV", Phys. Lett. B 754 235–248, arXiv:1509.07324 [nucl-ex], 2016.
- [11] E. Boltezar et al., "THE NEW CERN 50-MEV LINAC." in 10th International Linear Accelerator Conference, pp. S2–2. 1980.
- [12] E. Boltezar et al., "THE NEW CERN 50-MEV LINAC." in 10th International Linear Accelerator Conference, pp. S2-2. 1980.
- [13] M. Chanel, "LEIR: The low energy ion ring at CERN", Nucl. Instrum. Meth. A 532 137–143, 2004.

- [14] P. Sortais et al., "ECRIS as ion source and charge breeder", Nucl. Phys. A 701 537–549, 2002.
- [15] J. Schukraft, "Heavy-ion physics with the ALICE experiment at the CERN Large Hadron Collider", Philosophical Transactions of the Royal Society A: Mathematical, Physical and Engineering Sciences 370 no. 1961, 917–932, 2012.
- [16] W. P. C. Mills, "THE PRESENT PERFORMANCE OF THE SPS", *IEEE Trans. Nucl. Sci.* 26 3176, 1979.
- [17] A. Collaboration, "Observation of a new particle in the search for the Standard Model Higgs boson with the ATLAS detector at the LHC", *Physics Letters B* 716 no. 1, 1–29, 2012.
- [18] C. C. Kirti Ranjan, "Observation of a new boson at the LHC with the CMS Experiment", Nuclear Physics B - Proceedings Supplements 251-252 129-134, 2014. International Conference on Light-Cone Physics: Hadronic and Particle Physics.
- [19] R. Quagliani, "The LHCb detector at the LHC" in Study of Double Charm B Decays with the LHCb Experiment at CERN and Track Reconstruction for the LHCb Upgrade, pp. 29–65. Springer, 2018.
- [20] ALICE, "Schematics of the ALICE experiment", https://alice-figure.web.cern.ch/node/11219, 2017.
- [21] P. Cortese *et al.*, "ALICE Forward Detectors: FMD, TO and VO: Technical Design Report" tech. rep., ALICE-TDR-011, 2004.
- [22] J. Alme et al., "The ALICE TPC, a large 3-dimensional tracking device with fast readout for ultra-high multiplicity events", Nucl. Instrum. Methods Phys. Res. A 622 no. 1, 316–367, 2010.
- [23] ALICE, "ALICE technical design report of the photon spectrometer (PHOS)", CERN-LHCC-99-004, 1999.
- [24] R. Brun and F. Rademakers, "ROOT: An object oriented data analysis framework", *Nucl. Instrum. Meth. A* 389 81–86, 1997.

- [25] F. Bock, "Measurement of Direct Photons and Neutral Mesons in Small Collisions Systems with the ALICE Experiment at the LHC". PhD thesis, University Heidelberg, 2017.
- [26] N. Schmidt, "Direct photon and light neutral meson production in hadron collisions at the LHC with ALICE". PhD thesis, Goethe University Frankfurt, 2021.
- [27] ALICE, "Performance of the ALICE Electromagnetic Calorimeter", JINST 18 no. 08, P08007, arXiv:2209.04216 [physics.ins-det], 2023.
- [28] ALICE, "Neutral pion and η meson production in p-Pb collisions at $\sqrt{s_{\rm NN}}=5.02$ TeV", Eur. Phys. J. C 78 no. 8, 624, arXiv:1801.07051 [nucl-ex], 2018.
- [29] Particle Data Group, "Review of Particle Physics", PTEP 083C01, 2022.
- [30] ALICE, "Multiplicity dependence of pion, kaon, proton and lambda production in p-pb collisions at $\sqrt{s_{\rm NN}}=5.02$ tev", *Phys. Lett. B* 728 25–38, arXiv:1307.6796 [nucl-ex], 2014.
- [31] ALICE, "Data-driven precision determination of the material budget in ALICE", JINST 18 no. 11, P11032, arXiv:2303.15317 [physics.ins-det], 2023.
- [32] ALICE, "Neutral pion production at midrapidity in pp and Pb-Pb collisions at $\sqrt{s_{\rm NN}} = 2.76$ TeV", Eur. Phys. J. C 74 no. 10, 3108, arXiv:1405.3794 [nucl-ex], 2014.
- [33] A. A. Bylinkin and A. A. Rostovtsev, "Parametrization of the shape of hadron-production spectra in high-energy particle interactions", *Phys. Atom.* Nucl. 75 999–1005, 2012.
- [34] ALICE, "Measurement of pion, kaon and proton production in proton-proton collisions at $\sqrt{s} = 7$ TeV", Eur. Phys. J. C 75 no. 5, 226, arXiv:1504.00024 [nucl-ex], 2015.
- [35] ALICE, "Centrality dependence of particle production in p-Pb collisions at $\sqrt{s_{\rm NN}}=5.02$ TeV", *Phys. Rev. C* 91 no. 6, 064905, arXiv:1412.6828 [nucl-ex], 2015.

- [36] T. Adye, "Unfolding algorithms and tests using RooUnfold" in *PHYSTAT 2011*, pp. 313–318. CERN, Geneva, 2011. arXiv:1105.1160 [physics.data-an].
- [37] N. Strangmann, "Measurement of ω Meson Production in pp and p-Pb Collisions at $\sqrt{s} = 5.02$ TeV with ALICE", 2023.
- [38] M. Wälde, "Reconstruction of ω Meson decays to e^+e^- in pp collisions at $\sqrt{s} = 5.02$ TeV with ALICE", 2024.
- [39] ALICE, "Production of K* (892)⁰ and ϕ (1020) in p-Pb collisions at $\sqrt{s_{\rm NN}} = 5.02$ TeV", Eur. Phys. J. C 76 no. 5, 245, arXiv:1601.07868 [nucl-ex], 2016.
- [40] PHENIX, "Detailed measurement of the e^{\pm} pair continuum in pp and Au+Au collisions at $\sqrt{s_{\rm NN}}=200\,{\rm GeV}$ ", Phys. Rev. C 81 034911, arXiv:0912.0244 [nucl-ex], 2010.

Acknowledgements

This thesis, in its present form, would not have been possible without the support of many people, who I would like to thank.

I am very grateful to Prof. Henner Büsching. His warm welcome into his research group and the ALICE collaboration was only the beginning of his unwavering support. His constant encouragement to embrace the "Tschaka" spirit, as well as his openness to letting me explore my own interests in the analysis, have been invaluable. Prof. Büsching's dedication to every aspect of the analysis and the finalization of this thesis was extraordinary. Without his guidance in both physics and my aspirations in philosophy, I would not be the person I am today. I would also like to extend my gratitude to Prof. Harald Appelshäuser for kindly agreeing to review this thesis.

This analysis would not have been possible without the tireless support of Joshua König. His patience and passion for the project were evident in his constant explanations, and his enthusiasm was contagious. The additional outreach projects we worked on together, particularly building the Tubulum, greatly enriched my enjoyment of physics.

I am also very thankful to Friederike Bock for her encouragement in pursuing this analysis and her guidance in navigating its many challenges.

My office colleagues, Janis Jäger, Tuba Gündem, and Nicolas Strangmann, deserve special thanks for creating a supportive and understanding work environment. Their tolerance of the surrounding chaos was truly appreciated. In particular, Tuba's calming presence was a great help in the final weeks. I am also grateful to the entire Frankfurt working group for making me feel welcome and providing a nurturing environment throughout this thesis.

Maria Calmon Behling, Emma Ege and Marvin Hemmer have been an unwavering source of emotional support throughout this process. Their cheerful and kindhearted nature kept me grounded during the most stressful moments. Thank you for being such incredible people.

I also owe a special thanks to Eoghan, Mira, Roana, and Elias for their willingness to read this work at the last possible moment and their unconditional support.

Finally, I would like to express my sincere gratitude to Matthias Kleiner and Mario Krüger for their meticulous proofreading. Their attention to detail and relentless reminders that words hold meaning kept me going. Their efforts gave me the clarity and calm I needed to power through the final weeks.